

Distribution Agreement

In presenting this thesis or dissertation as a partial fulfillment of the requirements for an advanced degree from Emory University, I hereby grant to Emory University and its agents the non-exclusive license to archive, make accessible, and display my thesis or dissertation in whole or in part in all forms of media, now or hereafter known, including display on the world wide web. I understand that I may select some access restrictions as part of the online submission of this thesis or dissertation. I retain all ownership rights to the copyright of the thesis or dissertation. I also retain the right to use in future works (such as articles or books) all or part of this thesis or dissertation.

Signature:

Renke Huang

Date

Achieving *quantum practicality* via resource-efficient simulations of strongly
correlated molecules on quantum computers

By

Renke Huang
Doctor of Philosophy

Chemistry

Francesco A. Evangelista, Ph.D.
Advisor

Fang Liu, Ph.D.
Committee Member

Raphael F. Ribeiro, Ph.D.
Committee Member

Accepted:

Kimberly Jacob Arriola, Ph.D, MPH
Dean of the James T. Laney School of Graduate Studies

Date

Achieving *quantum practicality* via resource-efficient simulations of strongly correlated molecules on quantum computers

By

Renke Huang
B.Sc. Chemistry, Southern University of Science and Technology, Shenzhen,
China, 2018

Advisor: Francesco A. Evangelista, Ph.D.

An abstract of
A dissertation submitted to the Faculty of the
James T. Laney School of Graduate Studies of Emory University
in partial fulfillment of the requirements for the degree of
Doctor of Philosophy
in Chemistry
2023

Abstract

Achieving *quantum practicality* via resource-efficient simulations of strongly correlated molecules on quantum computers

By Renke Huang

In this dissertation, we aim to demonstrate practical applications of quantum computers in the quantum simulation of many-body problems. The first contribution is the development of a multireference selected quantum Krylov (MRSQK) algorithm. MRSQK generates a target state by constructing a basis of non-orthogonal Krylov basis states via efficient unitary time evolution using a set of reference states. This approach eliminates the need for numerical optimization of parameters and addresses the linear dependency problem through a basis selection procedure. Benchmarks on various systems demonstrate the feasibility of MRSQK to use compact Krylov bases for predicting both ground state and excited state energies. The second contribution is the proposal of a quantum unitary downfolding formalism based on the driven similarity renormalization group (QDSRG). The QDSRG is a polynomial-scaling downfolding method that retains the accuracy of classical multireference many-body theories while avoiding the evaluation of costly higher-order reduced density matrices. This method effectively reduces the dimensionality of the problem and minimizes the required quantum resources, which enables resource-efficient simulations on small-scale quantum computers using large computational basis sets. We model the bicyclobutane isomerization pathways to *trans*-butadiene on IBM quantum devices, demonstrating the viability of QDSRG to leverage near-term quantum devices for estimating molecular properties with chemical accuracy. We then extend the QDSRG method to a state-averaged formalism (SA-QDSRG) that is capable of treating near-degenerate states which pose great challenges for many quantum chemical methods. The SA-QDSRG allows for simulating a conical intersection on the excited-state energy surfaces of ethylene as well as resolving complex energetics of a non-radiative photodynamical process on small-scale quantum processors. This highlights the versatility and potential of the QDSRG downfolding approach.

Achieving *quantum practicality* via resource-efficient simulations of strongly correlated molecules on quantum computers

By

Renke Huang

B.Sc. Chemistry, Southern University of Science and Technology, Shenzhen,
China, 2018

Advisor: Francesco A. Evangelista, Ph.D.

A dissertation submitted to the Faculty of the
James T. Laney School of Graduate Studies of Emory University
in partial fulfillment of the requirements for the degree of
Doctor of Philosophy
in Chemistry
2023

Acknowledgments

I would like to take this opportunity to express my heartfelt gratitude to the following individuals who have played a significant role in my journey towards completing this PhD dissertation:

First and foremost, I am immensely grateful to my advisor, Prof. Francesco Evangelista. His invaluable guidance, profound insights, and inspiring moments have not only shaped me as an independent researcher but also added a touch of flavor to my academic pursuits. Thank you for fostering my growth.

I extend my sincere appreciation to Prof. Chenyang Li for helping me unravel all those mystical problems while running Forte, and your papers and notes that build the DSRG realm are always valuable resources for me. A special thanks go to Dr. Nan He for innumerable afternoon polymathic encyclopedical chats. From politics to finance, from machine learning to physics, your diverse perspectives have always been a source of inspiration and have broadened my horizons. I am indebted to Dr. Jonathon Misiewicz and Dr. Meng Huang for their unwavering intellectual support. Your contributions have been invaluable and have greatly enriched my work. To Dr. Ilias Magoulas, thanks for the laughter and insightful suggestions provided throughout my projects. Talking with you is always an enjoyable experience. Your positive energy and guidance have been a constant source of motivation.

I would also like to acknowledge my previous committee members, Prof. Joel M. Bowman and Prof. James T. Kindt, who congratulated me on my second-year qualifying exam, but also witnessed the most struggling moments of my doctoral journey during the third and fourth years. Your presence and

guidance were truly invaluable. A special mention goes to my current committee member, Prof. Raphael F. Ribeiro, for the tremendous support provided during my job search and for crafting excellent recommendation letters on my behalf. Your assistance has been instrumental, and I am grateful for your unwavering support. I am also grateful to Prof. Fang Liu and Prof. Yao Wang for offering me future job possibilities. Your belief in my potential is deeply appreciated.

Last but certainly not least, I would like to express my heartfelt gratitude to all my gym buddies. You have been instrumental in making me physically and emotionally stronger, helping me survive the last six months of graduate school. Chris, the strongest powerlifter I have ever seen in real life, your constant cheerfulness has never failed to uplift my spirits, even when I messed up my forms. To Robert and Jae, although our time together at Emory was brief, your inspiration and assistance in my training have been nothing short of epic. You have empowered me with the courage to confront and overcome my fears, and have motivated me to tackle those challenges that I had been procrastinating on for quite some time. And to all those familiar faces I kept bumping into at the gym, even though we never exchanged names, I just wanted to say a big thanks for all those shared moments. I truly appreciate them.

To all of you mentioned here, thank you from the bottom of my heart for your invaluable contributions, support, and friendship. This dissertation would not have been possible without each and every one of you.

Contents

1	Introduction	1
1.1	<i>Quantum practicality</i>	1
1.2	Models of quantum simulation	3
1.3	Problems in quantum chemistry	6
1.3.1	The electronic structure problem	6
1.3.2	Quantum dynamics	11
1.3.3	Computational complexity	13
1.4	Quantum computing basics	13
1.4.1	Quantum building blocks	13
1.4.2	Encoding fermionic problems on quantum computers . .	15
1.5	Quantum algorithms for quantum chemistry	16
1.5.1	Quantum phase estimation	16
1.5.2	Variational quantum eigensolver	17
1.5.3	Quantum imaginary time evolution	19
1.6	Outline of the dissertation	21
2	A multireference quantum Krylov algorithm for strongly-correlated electrons	23

2.1	Methods	28
2.1.1	Basis in MRSQK	28
2.1.2	State Preparation	33
2.1.3	Quantum Circuits for Measuring Matrix Elements	34
2.1.4	Cost Estimation	37
2.2	Computational Details	40
2.3	Results and Discussion	41
2.4	Summary	48
2.5	Appendix	49
2.5.1	Trotterization errors and term ordering	49
2.5.2	Comments	56
2.6	Computing electronic excited states via multireference quantum Krylov method	57
2.6.1	State-specific approach	57
2.6.2	State-averaged approach with dynamic weights	59
3	Leveraging small scale quantum computers with unitarily downfolded Hamiltonians	64
3.1	Methods	69
3.1.1	Unitary Hamiltonian downfolding via the DSRG	69
3.1.2	Hybrid quantum-classical DSRG downfolding	73
3.2	Calibration	80
3.2.1	Noiseless simulations	80
3.2.2	Sensitivity to noise	83
3.3	Results and Discussion	86

3.3.1	Dissociation curve of the nitrogen molecule	87
3.3.2	Singlet-triplet gaps of <i>para</i> -benzyne	90
3.3.3	Hardware implementation	93
3.4	Summary	101
3.5	Appendix	104
3.5.1	Symmetry-preserving ansatz for two-configuration wave functions	104
3.5.2	Comparing QDSRG with double unitary coupled cluster approach	108
4	Simulating conical intersections on quantum computers with uni- tarily downfolded Hamiltonians	110
4.1	Methods	113
4.1.1	State-averaged Hamiltonian downfolding via QDSRG . .	113
4.1.2	Quantum subspace expansion for excited states	115
4.1.3	Spin-restricted ansatz	115
4.2	Computational Details	117
4.3	Results and Discussion	117
4.4	Summary and future work	119
5	Conclusions and perspectives	122
	Bibliography	125

List of Figures

- 1.1 A circuit diagram for quantum phase estimation using three ancillary qubits. The circuit block labelled with QFT^{-1} executes the inverse quantum Fourier transformation. When the ancillary qubits are in state $|x\rangle$, a controlled rotation $e^{-2\pi i H x}$ is applied to the main register $|\Psi\rangle$. The ancillary qubits output an eigenvalue of H in binary when being measured in the computational basis; meanwhile the main register $|\Psi\rangle$ collapses to the corresponding eigenstate. The circuit diagram is adapted with permission from *Rev. Mod. Phys.*, 92(1):015003, 2020, DOI:10.1103/revmodphys.92.015003. Copyright 2020 American Physical Society. 18
- 1.2 Scheme of the variational quantum eigensolver (VQE) using three qubits. The scheme is reprinted with permission from *Rev. Mod. Phys.*, 92(1):015003, March 2020, DOI:10.1103/revmodphys.92.015003. Copyright 2020 American Physical Society. 19
- 1.3 Schematic of the quantum imaginary time evolution (QITE) algorithm 20

2.1	Schematic illustration of the multireference selected quantum Krylov (MRSQK) algorithm. (A) An approximate real-time dynamics using a single Slater determinant reference (Φ_0) is used to generate a trial state ($\tilde{\Psi}$). (B) Measurements of the determinants that comprise the trial state are used to determine the probability of hopping (P_μ) to other determinants. This information is employed to build two new reference states, Φ_1 and Φ_2 . (C) Finally, three real-time evolutions starting from the references (Φ_0, Φ_1, Φ_2) generate a set of 12 Krylov states ψ_α , which are used to diagonalize the Hamiltonian and obtain the energy of the state Ψ .	29
2.2	Hadamard test circuit to estimate expectation values of unitary operators with a general form of $\langle \bar{0} \hat{U}_\gamma^\dagger \hat{U}_\chi \bar{0} \rangle$. Measuring the X, Y operators on the ancillary qubit $ 0\rangle$, one can obtain the mean value of $X + iY = 2 0\rangle\langle 1 $, which equals to $\langle X + iY \rangle = \langle \bar{0} \hat{U}_\gamma^\dagger \hat{U}_\chi \bar{0} \rangle$	35
2.3	Circuit for applying one controlled- $e^{-it_l \otimes_k \sigma_k}$ operator.	36
2.4	The circuit to compute $\langle \Phi_1 e^{-i\Delta t \hat{H}_q} \Phi_1 \rangle$ (top) and $\langle \Phi_0 e^{i\Delta t \hat{H}_q} \Phi_1 \rangle$ (bottom) implemented using Qiskit[168]. q[0] , q[1] encode basis states for the Hamiltonian, while q[2] is the ancillary qubit, with c3 the classical bit to store the output from measuring q[2] . $U2(\pi/2, -\pi/2)$ gate before the measurement is the H_k gate rotating the state of ancillary qubit into the σ^Y basis.	37

2.5	Potential energy curve (top) and error (bottom) for symmetric dissociation of linear H_6 in a STO-6G basis. MRSQK computations use $\Delta t = 0.5$ a.u., three time steps ($s = 3$), and five references ($d = 5$) corresponding to 20 Krylov basis states. The number of Trotter steps (m) is indicated in parentheses, while those from exact time evolution are labeled ($m = \infty$).	45
2.6	Potential energy curve (top) and error (bottom) for symmetric dissociation of linear BeH_2 in a STO-6G basis. MRSQK computations use $\Delta t = 2$ a.u., four time steps ($s = 4$), and six references ($d = 6$) corresponding to 30 Krylov basis states. The number of Trotter steps (m) is indicated in parentheses, while those from exact time evolution are labeled ($m = \infty$).	47
2.7	Energy error ΔE (in E_h) as a function of the number of Krylov basis states N of linear H_6 at a bond distance of 1.5 \AA	53
2.8	Potential energy curve (top) and energy error (bottom) for symmetric dissociation of linear H_6 in STO-6G basis. References in MRSQK were selected using initial QK calculations with $s_0 = 4$ evolutions of the Hartree–Fock determinant and a time step of $\Delta t_0 = 0.25$ a.u. Then the following MRSQK calculations use $\Delta t = 0.5$ a.u., three time steps ($s = 3$), and five references ($d = 5$) corresponding to 20 Krylov basis states. Two orderings of Pauli terms are employed for comparison, with notations consistent with that in Table 2.4. The number of Trotter steps (m) is indicated in parentheses, while those from exact time evolution are labeled ($m = \infty$).	54

2.9	Potential energy curve (top) and energy error (bottom) for symmetric dissociation of linear BeH₂ in STO-6G basis. References in MRSQK were selected using initial QK calculations with $s_0 = 3$ evolutions of the Hartree–Fock determinant and a time step of $\Delta t_0 = 0.25$ a.u. Then the following MRSQK calculations use $\Delta t = 2.0$ a.u., three time steps ($s = 4$), and five references ($d = 6$) corresponding to 30 Krylov basis states. Two orderings of Pauli terms are employed for comparison, with notations consistent with that in Table 2.4. The number of Trotter steps (m) is indicated in parentheses.	55
2.10	Potential energy curves (in E_h) of the ground state (1^1A_g) and the first singlet excited state (2^1A_g) for the symmetric dissociation of H ₆ computed with the MRSQK method using two reference spaces. All calculations use a STO-6G basis. MRSQK computations use one Trotter step ($m = 1$), $\Delta t = 0.5$ a.u., three time steps ($s = 3$), and five references ($d = 4$) corresponding to 16 Krylov basis states.	61
2.11	Deviations of vertical excitation energies (in eV) from FCI results of the first singlet excited state (2^1A_g) along the symmetric dissociation of H ₆ computed with the MRSQK method using two reference spaces. All calculations use a STO-6G basis. MRSQK computations use one Trotter step ($m = 1$), $\Delta t = 0.5$ a.u., three time steps ($s = 3$), and five references ($d = 4$) corresponding to 16 Krylov basis states.	62

3.1	The QDSRG scheme for performing hybrid classical-quantum computations on strongly correlated molecules. The computation begins with a classical or hybrid orbital optimization (1), followed by the preparation of a correlated reference state defined in the subset of active molecular orbitals (2). This step yields the reduced density cumulants ($\tilde{\lambda}_k$), which are passed to a classical DSRG algorithm (3) to produce the effective Hamiltonian ($\bar{H}_{1,2}$) and its expectation value with respect to the approximate cumulants ($\langle \bar{H}_{1,2} \rangle_{\tilde{\lambda}_k}$). (4) In the last step, an eigenvalue of the DSRG effective Hamiltonian is found via a quantum algorithm.	73
3.2	The energy error for the H ₂ molecule (in mE_h) computed with the QLDSRG(2) with various amounts of stochastic noise (σ) added to the RDMs. For a given value of σ , the semiopaque circles aligned vertically show the distribution of errors from 50 computations, while the horizontal bars represent the average error. All computations use a cc-pVTZ basis [274] and the flow parameter value $s = 0.5 E_h^{-2}$. The energy errors are computed with respect to noiseless values. The data are obtained imposing $\gamma_3 = 0$ in the reconstruction of the approximate three-body cumulant.	84

3.3 The dissociation curve for the ground-state N_2 computed with the LDSRG(2) and QLDSRG(2). (a) The total energy and (b) the energy error with respect to FCI in units of E_h . Nonparallelism errors (in mE_h) for each method are reported in square brackets. All computations use an active space containing six $2p$ N atomic orbitals, a cc-pVDZ basis [274], and the flow parameter value $s = 0.5 E_h^{-2}$. The 1-QLDSRG(2)-CCSD data employ natural orbitals and γ_1 from CCSD as the input to the QDSRG computation. All other results employ CASSCF(6,6) orbitals. 87

3.4 The dissociation curve (a) and the energy error (b) for the H_2 molecule computed with the 2-QLDSRG(2) using one qubit on the `ibm_lagos` device. The energy errors are with respect to FCI energies. For each geometry, the semiopaque blue circles aligned vertically show the distribution of energies (energy errors) from 9 experiments, with each experiment consisting of 32000 measurements, while the horizontal bars in blue denote average energies or average energy errors. All computations use the cc-pV5Z basis [274] (110 basis functions), CASSCF(2,2) orbitals, and the flow parameter value $s = 0.5 E_h^{-2}$. The gray-shaded area indicates unsigned energy errors below $1 mE_h$. The unsigned energy errors and the standard deviations are reported in Table 3.4. 96

3.5	Conrotatory and disrotatory pathways describing the isomerization of bicyclo[1.1.0]butane (bicyclobutane) to <i>trans</i> -buta-1,3-diene (<i>trans</i> -butadiene). The enthalpies in kcal mol ⁻¹ are relative to the reactant for relevant stationary points computed with the 2-QLDSRG(2) method using one qubit on the device <code>ibmq_manila</code> . The black horizontal bars represent the 2-QLDSRG(2) results obtained with noiseless simulations. The device results are shown in parentheses. The semiopaque blue circles aligned vertically show the distribution of the relative enthalpies from eight experiments (20000 measurements per experiment), while the yellow horizontal bars denote the average relative enthalpies. We use a cc-pVTZ basis [274] (204 basis functions) and CASSCF(2,2) natural orbitals, and the flow parameter value $s = 1.0 E_h^{-2}$ for all six stationary points.	97
4.1	Definition of geometrical coordinates, torsion angle τ and pyramidalization angle β utilized in this study. The figure is adapted with permission from <i>J. Chem. Phys.</i> , 121(23):11614–11624, 2004, DOI:10.1063/1.1807378. Copyright 2023 American Institute of Physics.	113
4.2	Two π -like molecular orbitals in the active space for the twisted-pyramid conical intersection geometry. The orbitals are optimized at the CASSCF(2,2)/aug-cc-pVTZ level of theory.	116
4.3	Circuit for singlet-restricted ansatz for a CAS(2,2) system	116

4.4 Potential energy curves of the three lowest singlet states along the pyramidalization motion of one CH₂ group computed with (a) SA-DSRG-PT2 [solid lines] and 2-SA-QDSRG-PT2 [asterisks], (b) SA-LDSRG(2) [solid lines], 2-SA-QLDSRG(2) [asterisks], (c) diagonalizing the bare Hamiltonian. Energies are shifted with respect to the ground-state energy of the planar geometry calculated using the same method. The vertical dash lines and angle values denote the twisted-pyramid conical intersection geometry at the corresponding computational level.

..... 121

List of Tables

2.1	Resource estimates for MRSQK calculations with $m = 1$ Trotter step approximation on several hydrogen systems in STO-6G basis at the bond length $R=1.5 \text{ \AA}$. Jordan-Wigner transformation is used to encode the Hamiltonian for all cases in the table. . . .	38
2.2	Ground-state energies (in E_h) of H_6 and H_8 at a site-site distance of 1.5 \AA using exact time-evolution. Energy and overlap condition number $k(S)$ results are given for a single determinant (QK) using N Krylov basis states and $\Delta t = 0.5$. MRSQK results are given for $N = d(s + 1)$ Krylov basis states using three steps ($s = 3$) and $\Delta t = 0.5$ a.u. With N greater than 12 states, the condition number for QK does not grow larger than 10^{18} . This is likely a result of limitations of double precision arithmetic.	41

- 2.3 The energy error (in mE_h) of the ground-state (in E_h) of H_6 at a bond distance of 1.5 Å. MRSQK results are given for $N = d(s + 1)$ Krylov basis states using three steps ($s = 3$) and $\Delta t = 0.5$ a.u. The quantity m indicates the Trotter number. For each value of N , selected configuration interaction (sCI) results were obtained using N determinants with the largest absolute coefficient in the FCI wave function. ADAPT-VQE results show the energy with N cluster amplitudes selected from the pool of spin-adapted generalized singles/doubles. All energy errors are computed with respect to the FCI energy ($-3.020198 E_h$). . . . 44
- 2.4 Ground-state energies (in E_h) of H_6 at a bond distance of 1.5 Å computed with MRSQK using different term orderings. MRSQK calculations use $N = d(s + 1)$ Krylov basis states with three steps ($s = 3$) and $\Delta t = 0.5$ a.u. m indicates the Trotter number. Subscripts denote different ordering type of Pauli terms in the qubit Hamiltonian after the Trotterization. **OF**: OpenFermion’s default QubitOperator ordering; **JW**: terms are sorted in the descending order based on the magnitude of coefficients after *Jordan-Wigner* transform (Pauli term with largest magnitude goes first); **sq**: terms are sorted in the descending order based on the magnitudes of amplitudes of fermion operators in the *second quantized* form of the Hamiltonian (the group of terms from the fermion operator with the largest amplitude go first). **rand**: Pauli terms are shuffled *randomly* after *Jordan-Wigner* transform. 51

2.5 Two reference spaces used in MRSQK method for computing the first singlet excited state (2^1A_g) of linear H_6 . The orbitals are ordered by the irreducible representation of the D_{2h} point group as $1a_g, 2a_g, 3a_g, 1b_{1u}, 2b_{1u}, 3b_{1u}$. The ordering of orbital energies (in ascending order) from the restricted Hartree–Fock calculation is given by $1a_g < 1b_{1u} < 2a_g < 2b_{1u} < 3a_g < 3b_{1u}$, so the Hartree–Fock determinant is $|220200\rangle$ 59

2.6 Vertical excitation energies ΔE (in eV) for the first singlet excited state (2^1A_g) of linear H_6 at two bond distance 1.5 Å and 0.9 Å computed with MRSQK method in a STO-6G basis. MRSQK calculations use $N = d(s + 1)$ Krylov basis states using $\Delta t = 0.5$ a.u. and three steps ($s = 3$). The vertical excitation energy is calculated with respect to the corresponding ground-state energy obtained using the same values for N and m (as reported in Table 2.3). Note that we take the Trotter approximation with $m = 100$ as a good approximation to the infinite m limit. The data in parentheses show deviations from the FCI result ($\epsilon = \Delta E_{\text{MRSQK}} - \Delta E_{\text{FCI}}$, unit in eV). The best estimate of each reference space is indicated in bold type. 60

2.7	Statistical evaluation for deviations of vertical excitation energies (in eV) along the dissociation of H ₆ as shown in Figure 2.11. The mean absolute error (MAE, in eV) is estimated as an arithmetic average of the absolute errors over 28 geometries. The nonparallelism error (NPE, in eV) is defined as the difference between the largest and smallest excitation energy deviation from the FCI vertical excitation energy along the symmetric dissociation curve.	61
3.1	The energy error for the H ₂ molecule (in mE _h) computed with the LDSRG(2) and QLDSRG(2) methods. All computations use a cc-pVTZ basis [274] and the flow parameter value $s = 0.5 E_h^{-2}$. The energy errors are computed with respect to full configuration interaction (FCI) energies (in E _h) reported in the last row of the table. For the LDSRG(2), the expectation value of the energy is designated with “ $\langle \bar{H}_{1,2} \rangle$,” while the lowest eigenvalue is indicated with “eig. $\bar{H}_{1,2}$.” For the QDSRG methods, we report two sets of data. Those labeled “ $\gamma_3 = 0$ ” use an approximate three-body cumulant reconstructed from $\tilde{\lambda}_1$ and $\tilde{\lambda}_2$. The results for line M employ CCSD natural orbitals and the one-body relaxed CCSD reduced density matrix as input to the QDSRG procedure.	79

3.2 Spectroscopic constants for the ground state ($X^1\Sigma_g^+$) of N_2 from the dissociation curves in Figure 3.3. The data in parentheses show deviations from FCI results. All LDSRG(2) and QLDSRG(2) computations as well as literature results listed here use the cc-pVDZ basis.	88
3.3 Adiabatic singlet-triplet splittings ($\Delta E_{ST} = E_T - E_S$) in kcal mol ⁻¹ of <i>para</i> -benzyne computed with the LDSRG(2) and QLDSRG(2) in the cc-pVTZ basis [274] with the flow parameter value $s = 1.0 E_h^{-2}$. The data in parentheses show the difference with respect to the experimental value of ΔE_{ST} (in kcal mol ⁻¹). All LDSRG(2) and QLDSRG(2) results include a zero-point vibrational energy (ZPVE) correction equal to +0.30 kcal mol ⁻¹ (see Ref. [290]). The geometries are taken from Ref. [291]. We use CASSCF(2,2) optimized orbitals for all computations of the singlet state and ROHF orbitals for the triplet state. For the LDSRG(2), the expectation value of the energy is designated with “ $\langle \bar{H}_{1,2} \rangle$ ”, while the lowest eigenvalue is indicated with “eig. $\bar{H}_{1,2}$ ”. For the QDSRG methods, we report two sets of data. Those labeled “ $\gamma_3 = 0$ ” use an approximate three-body cumulant reconstructed from approximate $\tilde{\lambda}_1$ and $\tilde{\lambda}_2$. All literature results listed here for comparison use the same cc-pVTZ basis.	91

3.4	The errors of 2-QLDSRG(2) energies in mE_h (with respect to FCI energies) along the H_2 dissociation curve (Figure 3.4). For results from the <code>ibm_lagos</code> device, we show the unsigned average energy errors and standard deviations (in mE_h). Unsigned energy errors below $1 mE_h$ are highlighted in bold type.	95
3.5	LDSRG(2) and QLDSRG(2) (exact and device) computations of the relative enthalpies (in kcal mol^{-1}) with respect to the bicyclobutane reactant of the conrotatory transition state and the disrotatory transition state, the <i>gauche</i> -butadiene intermediate, the transition state connecting <i>gauche</i> -butadiene and <i>trans</i> -butadiene, and the <i>trans</i> -butadiene product. We use the cc-pVTZ basis [274] (204 basis functions) and CASSCF(2,2) natural orbitals, and the flow parameter value $s = 1.0 E_h^{-2}$. All results include zero-point vibrational energy (ZPVE) corrections taken from Ref. [304]. The OMR3-DMC and CC(t;3) results also use the cc-pVTZ basis. The differences of values (in kcal mol^{-1}) with respect to the experimental data for the conrotatory transition state and <i>trans</i> -butadiene are shown in parentheses; values within 1 kcal mol^{-1} deviation are indicated in bold type.	98
3.6	Summary of the number of qubits required for the full-space and QDSRG computations that use large basis sets in this study.	104

- 3.7 The relations between the elements of the fermionic 1-RDM ($\gamma_q^p = \langle a_p^\dagger a_q \rangle$) and 2-RDM ($\gamma_{rs}^{pq} = \langle a_p^\dagger a_q^\dagger a_s a_r \rangle$) and the measured quantities for the one-qubit ansatz. Only nonzero elements are shown; others are zero due to symmetries. $|C_1|^2 = \langle \Psi|0\rangle \langle 0|\Psi\rangle$ and $|C_2|^2 = \langle \Psi|1\rangle \langle 1|\Psi\rangle$ are obtained from projective measurements [51, 321] of the optimized state in the computational basis; $\langle X \rangle$ is the expectation value of the Pauli X operator. . . 107
- 3.8 A comparison of the energy errors (in mE_h) of the QDSRG and the DUCC for the H_2 molecule at four bond lengths in the cc-pVTZ basis using DSRG flow parameter $s = 0.5 E_h^{-2}$. The size of the active space is denoted in parentheses. The energy errors are with respect to the full-space (30-orbital) FCI computations [absolute energies (in E_h) are shown in the first row]. The DUCC data are taken from Ref. [238]. 108
- 3.9 A comparison of the energy errors (in mE_h) of the QDSRG and the DUCC for the Be atom with different basis sets and active spaces. The DSRG flow parameter $s = 2.0 E_h^{-2}$. All computations use RHF orbitals. The energy errors are with respect to the full-space FCI computations [absolute energies (in E_h) are shown in the last column], which use 14, 30 and 55 orbitals for the cc-pVDZ, cc-pVTZ, and cc-pVQZ basis sets, respectively. The DUCC data are taken from Ref. [238]. 109

4.1	Excitation energies (in eV) of the three lowest singlet states of the twisted-pyramid conical intersection geometry. The excitation energies are computed with respect to the ground-state energy of the planar geometry (Franck-Condon point) calculated at the corresponding computational level.	119
-----	---	-----

Chapter 1

Introduction

1.1 *Quantum practicality*

The original concept of quantum computing traces its roots back to the 1980s when the legendary physicist, Richard P. Feynman [1, 2] and the Russian mathematician Yuri Manin [3] independently envisioned the idea of harnessing quantum mechanical systems for computational purposes. This revolutionary notion was spurred by the realization that solving the many-body Schrödinger equation for systems exhibiting strong correlation effects posed significant challenges [4] for classical computers. These problems arise from the exponential growth of the Hilbert space dimension of a quantum mechanical system with respect to the number of particles in this system; this requires exponential resources (space or time) for exact simulations as the size of the system increases. Consequently, classical computers face great difficulty in simulating general quantum systems, such as computing the ground state—also known as the eigenstate corresponding to the lowest en-

ergy/eigenvalue—which is a notoriously NP-complete problem [5]. However, not all quantum mechanical systems are equally demanding to simulate. This fact lays the physical foundation for the development of quantum computers. Quantum mechanical systems that are easily controllable and possess computable exact solutions or approximate solutions with arbitrary tight error bound, can be leveraged to perform the computation or the simulation of complex quantum systems that are otherwise intractable [6, 7].

With decades of groundbreaking advancements throughout the full quantum hardware/software stack, the applications of quantum computing have extended well beyond its initial purpose as a quantum simulator for other quantum systems. The vast potential of quantum computers is unlocked through the construction of full-stack quantum computer systems and the exploration of meaningful applications [8]. A wide range of complex problems of academic and/or commercial interest have been suggested to potentially benefit from *quantum speedup* (the time scaling for a quantum algorithm grows more slowly with the size of the problem than its classical counterpart), including cryptanalysis, chemistry, materials science, optimization, big data processing, machine learning, database search, drug design, protein folding, fluid dynamics, weather prediction, etc. However, not all applications can achieve a practical quantum advantage (***quantum practicality***) in practice even on a futuristic fault-tolerant quantum device.

In a recent commentary, researchers at Microsoft have suggested multiple guidelines for achieving ***quantum practicality*** and identified problems with realistic quantum speedup from many proposed applications [9]. The first consideration, the *I/O bottleneck* of quantum computers when accessing large

amounts of classical data, ruled out problems that relied on broad bandwidths of data input and output. Typical problems include database search and unstructured linear algebra systems [10]. The second criterion, *crossover time*, must be short enough to have the runtime advantage of quantum computers. The analysis shows that quantum algorithms that only promise quadratic quantum speedups (those based on Grover's search algorithm [11, 12]) are unlikely to show a practical advantage, which requires at least cubic or quartic speedups [13]. This guideline further eliminates several applications, including the utilization of quantum random walks for accelerating Monte Carlo simulations, employing Grover's algorithm-based optimization and machine learning algorithms to enhance protein structure prediction and drug discovery [14].

One particularly promising domain for achieving *quantum practicality* is the quantum simulation of quantum problems in chemistry and materials science. These are small-data problems that exhibit exponential quantum speedup. History goes back to the original proposal of quantum advantage. By simulating quantum chemical problems on quantum computers, significant advancements can be made in areas such as the design of new catalysts which enable more efficient nitrogen fixation or CO₂ reduction [15]. These breakthroughs have the potential to revolutionize the field and pave the way for new strategies and technologies with far-reaching implications.

1.2 Models of quantum simulation

There are two distinct models for quantum simulations [16]. Feynman's initial proposal of a quantum mechanical computer aligns more with **analog quantum simulation**, where the dynamics of a controllable quantum simulator emulates the dynamics of a model quantum system that we are interested in. For instance, ultracold atoms can be manipulated to simulate electron dynamics by adjusting the interactions between these atoms via adjusting laser light, switching external electric and magnetic fields [17]. Analog simulators are typically regarded as more resilient to noise, making them easier to construct [6, 18].

Various physical implementations of analog quantum simulations have been successfully demonstrated for practical chemical applications. For example, simulators based on ultracold atoms and semiconductor quantum dots are utilized to simulate simple chemical reactions [19, 20]. Photonic analog simulators are applied to investigate molecular vibronic spectroscopy [21, 22, 23, 24] and to examine the time dynamics of vibrational excitations [25]. Trapped ion devices are employed to emulate both molecular vibronic spectra [26] and the many-body electron-electron Coulomb interaction of an electron gas [27]. Spin-lattice simulators are used to solve quantum chemical nuclear dynamics [28]. Superconducting simulators show the capability to generate molecular spectra for both equilibrium and non-equilibrium states of diatomic molecules [29]. These sophisticated analog quantum simulations achieved in condensed matter physics [30, 31, 32] and molecular quantum chemistry [17, 33] may already exceed the capabilities of

classical simulations.

However, analog quantum simulators always suffer from imperfect control, as the actual quantum system in the laboratory only provides a rough approximation of the specific quantum system of interest, no matter how precise the manipulations are. There is no systematic way to mitigate or correct such errors in large analog simulations. In another aspect, analog simulation is highly domain-specific, requiring distinct programs for various systems of interest. In this model, computations are articulated through technical protocols of experimental operations conducted at the hardware level, as opposed to an abstract algorithmic procedure commonly employed in classical computations.

In contrast, the more flexible **digital quantum simulation** is based on general-purpose (universal) circuit-based quantum computers that are capable of simulating any desired real system through appropriate programming, while also serving various other purposes. Digital quantum simulation maps the target problem onto a set of gates that can be executed on a quantum computer. Though digital quantum simulations are more sensitive to noise and device imperfections than analog simulations, systematic protocols have been established for error correction [34, 35] and error mitigation [36, 37, 38].

Under the framework of universal quantum computers, computations in quantum chemical simulation utilize the same language as those for solving algebraic problems [39]. Layers of abstraction similar to classical digital computers make the evaluation of quantum algorithms more straightforward.

In the subsequent sections of this dissertation, we will focus exclusively on the digital quantum simulation of chemistry problems.

1.3 Problems in quantum chemistry

1.3.1 The electronic structure problem

The fundamental problem in molecular quantum chemistry is to solve the time-independent, non-relativistic electronic Schrödinger equation under the Born-Oppenheimer approximation

$$\hat{H}_{\text{elec}}(\mathbf{R}, \mathbf{r})\psi(\mathbf{R}, \mathbf{r}) = E_{\text{elec}}(\mathbf{R})\psi(\mathbf{R}, \mathbf{r}) \quad (1.1)$$

where we define the collective electronic $\mathbf{r} = \{\vec{r}_i\}$ and nuclear $\mathbf{R} = \{\vec{R}_A\}$ degrees of freedom, and the electronic Hamiltonian (in atomic units) is given by

$$\hat{H}_{\text{elec}} = -\frac{1}{2} \sum_i^{N_e} \nabla_i^2 - \sum_i^{N_e} \sum_A^{N_{\text{nuc}}} \frac{Z_A}{|\vec{r}_i - \vec{R}_A|} + \frac{1}{2} \sum_{i \neq j}^{N_e} \frac{1}{|\vec{r}_i - \vec{r}_j|} \quad (1.2)$$

where N_e and N_{nuc} are the number of electrons and nuclei in the system, \vec{r}_i and \vec{R}_A are the position of electron i , atomic nucleus A , and Z_A represents the charge of nucleus A .

Solving the electronic Schrödinger equation provides the electronic wavefunction and the corresponding energy levels, which yield valuable information about the electronic structure and the molecular properties. From a mathematical standpoint, the problem is to solve a coupled set of partial differential equations. To tackle this, the main numerical tool is to introduce a basis set, which encompasses a set of independent functions. These functions are utilized to expand the abstract wavefunction vectors either in position space when Gaussian functions are employed or in momentum space when plane

wave functions are used [40]. In this way, the electronic Hamiltonian is expressed as a Hermitian matrix. Resolving the eigenvalue problem associated with this matrix yields the electronic energy spectrum of the molecule.

For the scope of this dissertation, we work with the electronic Hamiltonian in the second-quantized formalism

$$\hat{H} = \sum_{pq} h_{pq} \hat{a}_p^\dagger \hat{a}_q + \frac{1}{4} \sum_{pqrs} \langle pq||rs \rangle \hat{a}_p^\dagger \hat{a}_q^\dagger \hat{a}_s \hat{a}_r \quad (1.3)$$

where h_{pq} are the one-electron integrals and $\langle pq||rs \rangle$ two-electron integrals, \hat{a}^\dagger and \hat{a} are creation and annihilation operators, respectively. The first term represents the kinetic and potential energy of the electrons in the presence of the molecular field, and the second term accounts for the electron-electron repulsion.

Slater determinants To solve the electronic Schrödinger equation for many-electron systems, the Slater determinant basis is a commonly used mathematical construct. It is particularly well-suited for describing the electronic wavefunction, because it enforces the correct fermionic symmetry by ensuring that the wavefunction remains antisymmetric under electron exchange.

The electronic wavefunction of a system with N electrons can be written as a product of one-electron wavefunctions, also known as molecular orbitals (MOs) or spin orbitals (SOs) when spin part is included. The Slater determinant is constructed by antisymmetrizing the product of spin orbitals, ensuring that the resulting wavefunction is antisymmetric with respect to the exchange of any two electrons. This antisymmetry is a direct consequence of the Pauli

exclusion principle and accurately reflects the indistinguishability nature of electrons. Given a basis that contains M orthonormal spin orbitals $\{\psi_i(\mathbf{x})\}$, where the collective coordinates \mathbf{x} represent the spatial coordinates \mathbf{r} and the spin coordinate σ of the electron. A normalized Slater determinant for N electrons is then given by:

$$\Psi(\mathbf{x}_1, \mathbf{x}_2, \dots, \mathbf{x}_N) = \frac{1}{\sqrt{N!}} \begin{vmatrix} \phi_1(\mathbf{x}_1) & \phi_2(\mathbf{x}_1) & \dots & \phi_N(\mathbf{x}_1) \\ \phi_1(\mathbf{x}_2) & \phi_2(\mathbf{x}_2) & \dots & \phi_N(\mathbf{x}_2) \\ \vdots & \vdots & & \vdots \\ \phi_1(\mathbf{x}_N) & \phi_2(\mathbf{x}_N) & \dots & \phi_N(\mathbf{x}_N) \end{vmatrix} \quad (1.4)$$

In the second-quantized formalism (in the Fock space), each Slater determinant is represented by an occupation number vector $|\mathbf{f}\rangle$ given by

$$|\mathbf{f}\rangle = |f_1, f_2, \dots, f_i, \dots, f_M\rangle, \quad f_i = \begin{cases} 1 & \phi_i \text{ occupied} \\ 0 & \phi_i \text{ unoccupied} \end{cases} \quad (1.5)$$

Therefore, the occupation number $f_i = 1$ if ϕ_i is present in the determinant and $f_i = 0$ if it is absent.

Hartree-Fock method There is a full hierarchy of approximative numerical methods for solving the electronic Schrödinger equation with increasing accuracy and cost. The simplest approach, Hartree-Fock (HF) method, provides a way to obtain the most accurate single Slater determinant approximation for the system [41]. It is also known as the mean-field approach, since in Hartree-Fock theory the electrons are treated as if they were moving independently in an effective field created by the other electrons and the atomic nuclei.

We start by assuming a set of molecular orbitals (MOs), which are typically expanded as a linear combination of atomic orbitals (AOs) from the constituent atoms

$$\psi_i = \sum_{\mu}^{\text{AO}} \chi_{\mu} C_{\mu i} \quad (1.6)$$

where ψ_i is the i -th molecular orbital, χ_{μ} is the μ -th atomic orbital and $C_{\mu i} = \langle \chi_{\mu} | \psi_i \rangle$ represents the expansion coefficients. The molecular orbitals are enforced to be orthonormal and satisfy the condition $\langle \psi_i | \psi_j \rangle = \delta_{ij}$. The goal of Hartree-Fock theory is to determine the best set of expansion coefficients $C_{\mu i}$ that minimize the energy. This is done by solving a set of self-consistent field equations, which are derived by minimizing the electronic energy under the orthonormality constraint of the molecular orbitals based on the variational principle [42]. The Hartree-Fock equations can be written as:

$$\hat{F}\psi_i = \epsilon_i \psi_i \quad (1.7)$$

where the Fock operator is given by

$$\hat{F} = \hat{H}^{\text{core}} + \hat{J} - \hat{K} \quad (1.8)$$

Here, \hat{H}^{core} is the one-electron term that describes the motion of electrons in the field of the atomic nuclei, \hat{J} is the Coulomb operator that represents the classical electron-electron repulsion, and \hat{K} is the exchange operator that accounts for exchange interactions.

The Hartree-Fock equations in a finite computational basis (AO basis) $\{\chi_{\mu}\}$

are called Roothan equations [43] and are given by

$$\mathbf{FC} = \mathbf{SCE} \quad (1.9)$$

where \mathbf{F} is the Fock matrix, \mathbf{S} is the overlap matrix of atomic orbitals, \mathbf{E} is a diagonal matrix containing the molecular orbital energies. Due to the presence of \mathbf{S} , this generalized eigenvalue problem is solved iteratively until the electronic energy and the density converge.

The set of molecular orbitals obtained from Hartree-Fock equations is usually a good starting point for more advanced post-Hartree-Fock electronic structure methods.

Electron correlation The Hartree-Fock energy is only exact for one-electron systems. For most multi-electron systems, correlation effects that cannot be adequately captured by the Hartree-Fock (single-determinant) approximation are by convention classified into two types:

- Dynamic correlation refers to the rapid, non-local fluctuations of electron positions due to their mutual repulsion. These fluctuations occur on a very short timescale and involve the exchange of electrons between different regions of space. Dynamic correlation effects are particularly important to achieve high accuracy in characterizing transition metal complexes or molecules with highly delocalized electrons [44].
- Static correlation arises from the possibility of multiple Slater determinants (electronic configurations) with similar energies. In molecules with near-degenerate electronic states, the wavefunction cannot be accurately described by a single determinant. This is often the case in

molecules undergoing bond breaking or in photochemical processes that involve electronic excited states [45]. Static correlation effects require a proper treatment of the wavefunction to capture the mixing of multiple determinants.

The Full Configuration Interaction (FCI) method gives the exact solution to the electronic Schrödinger equation within a given finite orbital basis. FCI includes all possible determinants, allowing for a complete treatment of electron correlation

$$\Psi_{\text{FCI}} = \sum_I C_I \Psi_I \quad (1.10)$$

However, the number of determinants in the FCI space grows exponentially with the number of electrons N_e and the number of correlated spin orbitals M , making FCI computationally intractable for larger systems.

As a result, approximations and truncations are often employed to balance accuracy and computational cost. Various truncated CI methods and truncated coupled-cluster methods are commonly used approaches that include a subset of determinants based on excitation level. In practice, these methods usually truncated at double excitation level from the Hartree-Fock determinant [41, 42].

1.3.2 Quantum dynamics

The electronic energy spectra and wave functions obtained from Eqn. 1.1 describe stationary states of the system. Many complex processes in nature happen at finite temperature or other conditions that have non-trivial time dynamics of the system. Dynamical properties are encoded in the

time-dependent Schrödinger equation

$$i\frac{\partial}{\partial t}\Psi(\mathbf{r},t) = \hat{H}\Psi(\mathbf{r},t). \quad (1.11)$$

When the Hamiltonian is time-independent, which is usually the case for a large class of dynamical processes that chemists are interested in, the time-evolved state can be written as

$$\Psi(\mathbf{r},t) = e^{-i\hat{H}t}\Psi(\mathbf{r},0). \quad (1.12)$$

Expanding $\Psi(\mathbf{r},0)$ in the eigenstate basis $\{\varphi_J(\mathbf{r})\}$ of the time-independent Hamiltonian yields

$$\Psi(\mathbf{r},t) = \sum_J C_J e^{-iE_J t} \varphi_J(\mathbf{r}) \quad (1.13)$$

where $C_J = \langle \varphi_J(\mathbf{r}) | \Psi(\mathbf{r},0) \rangle$ is the expansion coefficient, and E_J is the energy of eigenstate $\varphi_J(\mathbf{r})$.

Eqn. 1.13 reveals that dynamic problems are considerably more complex than static problems. This complexity arises from the requirement of knowing the complete spectrum of the Hamiltonian, as well as the expansion coefficient of each eigenvector in the initial state, to execute the exact time evolution of the system. Such an exact solution is only possible for systems with very few electrons. Consequently, quantum dynamics for medium- to large-sized molecules becomes a class of problems that cannot be effectively solved using classical computers.

1.3.3 Computational complexity

Quantum computers have a considerable advantage for simulating the dynamics of how a highly-entangled quantum state evolves with time because it is intrinsically capable of maintaining the entangled state, which circumvents the exponential memory overhead of classical algorithms to store all the coefficients in the FCI expansion. In the language of computational complexity class, simulating unitary time evolution is a **BQP** problem [46], while BQP refers to the set of problems that can be efficiently solved using a quantum computer with polynomial resources and a bounded probability of error. Other typical **BQP** problems in quantum chemistry include quantum phase estimation (QPE)[47] and approximating the time-dependent effective Kohn-Sham potential in density functional theory [48].

1.4 Quantum computing basics

1.4.1 Quantum building blocks

The **qubit** [49], also known as quantum bit, serves as the fundamental building block of quantum information in quantum computing. It is the quantum analog of the binary bit that is used to represent information in classical computers. In mathematics, a single qubit is a two-level quantum-mechanical system described by a unit state vector in a two-dimensional complex vector space \mathcal{V} , also known as Hilbert space

$$|q\rangle = \cos \frac{\theta}{2} |0\rangle + \sin \frac{\theta}{2} e^{i\phi} |1\rangle \quad (1.14)$$

Any stable two-state devices could be a potential candidate for the physical realization of a qubit. Typical two-state quantum systems include the spin-up and spin-down state of electron spin or atomic spin in optical lattices, the vertical and horizontal polarization of a single photon, the clockwise and counterclockwise current of a superconducting Josephson junction, etc [50, 51, 52]. Therefore, the development of quantum hardware has branched to different physical architectures.

A single qubit has the potential to hold significantly more information than a classical bit, although it requires multiple preparations and measurements to extract that information. However, the true power of quantum computing lies in the exponential growth of the computational space when entangling an increasing number of qubits. An arbitrary state of an n -qubit system is represented by a unit vector in the tensor product space of singlet-qubit Hilbert space.

$$|Q\rangle = a_0 |0 \dots 00\rangle + a_1 |0 \dots 01\rangle + \dots + a_{2^n-1} |1 \dots 11\rangle \quad (1.15)$$

where n qubits encode 2^n probability amplitudes and computational basis states that can be exploited to store the information.

A **quantum circuit** consists of a number of single and two qubit gates that act on the qubits. These qubit gates are all unitary transformation acting on the state vector of qubits. The most commonly used are the Pauli gates

$$X = \begin{bmatrix} 0 & 1 \\ 1 & 0 \end{bmatrix}, \quad Y = \begin{bmatrix} 0 & -i \\ i & 0 \end{bmatrix}, \quad Z = \begin{bmatrix} 1 & 0 \\ 0 & -1 \end{bmatrix}, \quad (1.16)$$

the Hadamard gate

$$H = \frac{1}{\sqrt{2}} \begin{bmatrix} 1 & 1 \\ 1 & -1 \end{bmatrix} \quad (1.17)$$

which is useful to create a superposition state, for example, $H|0\rangle = (|0\rangle + |1\rangle)/\sqrt{2}$. There are also single qubit rotation gates that contain parameters,

$$R_Y(\beta) = \begin{bmatrix} \cos \frac{\beta}{2} & -\sin \frac{\beta}{2} \\ \sin \frac{\beta}{2} & \cos \frac{\beta}{2} \end{bmatrix}, \quad R_Z(\beta) = \begin{bmatrix} e^{-i\beta/2} & 0 \\ 0 & e^{i\beta/2} \end{bmatrix}, \quad (1.18)$$

which can be used to construct a parametrized variational ansatz. To entangle qubits, the two qubit controlled-NOT (CNOT) gate is required, which is mathematically written as

$$\text{CNOT}_{t,c} = I_t \otimes |0\rangle\langle 0|_c + X_t \otimes |1\rangle\langle 1|_c \quad (1.19)$$

where t denotes the target qubit, c denotes the control qubit.

1.4.2 Encoding fermionic problems on quantum computers

We are interested in simulating chemical systems in the second-quantised representation (Eqn. 1.3). To preserve the antisymmetry condition of fermionic wave functions, the second-quantised creation and annihilation operators must follow the anticommutation relations

$$\{\hat{a}_p, \hat{a}_q^\dagger\} = \delta_{pq}, \quad \{\hat{a}_p, \hat{a}_q\} = \{\hat{a}_p^\dagger, \hat{a}_q^\dagger\} = 0 \quad (1.20)$$

To encode these fermionic operators acting on indistinguishable fermions

into qubit operators acting on distinguishable qubits, the most common mapping is the Jordan-Wigner transformation [53, 54] given by

$$\begin{aligned}\hat{a}_p &= \frac{\hat{X}_p + i\hat{Y}_p}{2} \otimes \hat{Z}_{p-1} \otimes \dots \hat{Z}_0 \\ \hat{a}_p^\dagger &= \frac{\hat{X}_p - i\hat{Y}_p}{2} \otimes \hat{Z}_{p-1} \otimes \dots \hat{Z}_0\end{aligned}\tag{1.21}$$

The occupation number of a spin orbital is stored in the $|0\rangle$ or $|1\rangle$ state of a qubit

$$\begin{aligned}|f_M, \dots, f_i, \dots, f_1\rangle &\rightarrow |q_M, \dots, q_i, \dots, q_1\rangle \\ q_i &= f_i \in \{0, 1\}\end{aligned}\tag{1.22}$$

In this way, every Slater determinant in the FCI wavefunction can be written as one of the computational basis states, so M qubits can efficiently store the FCI wavefunction in M spin orbitals, surpassing the exponential memory scaling with respect to the system size. This quantum advantage also holds for any other second-quantised mappings [55, 54].

1.5 Quantum algorithms for quantum chemistry

In this section, we give an overview of several prototype quantum algorithms for quantum chemical applications.

1.5.1 Quantum phase estimation

Suppose we have a unitary operator U and one of its eigenvectors $|u\rangle$ with eigenvalue $e^{2\pi i\varphi}$ where φ is unknown. The value of φ can be obtained through the quantum phase estimation subroutine. A general circuit form of QPE can

be found in Nielsen and Chuang’s canon [50].

In the case of quantum chemistry, phase estimation can be formulated to compute the lowest energy eigenstate $|E_0\rangle$ of a Hamiltonian [56]. Figure 1.1 shows a pedagogical example of how to construct a circuit for phase estimation using three ancillary qubits. When the ancillary qubits are in the state $|x\rangle$, a controlled rotation $e^{-2\pi i H x}$ is applied to the qubit registers that encode $|\Psi\rangle$. After layers of controlled gates, an inverse quantum Fourier transform is performed over all ancillary qubits before measuring these qubits in the standard computational basis. The measurement outputs a bit-string $\text{bin}(E_0)$ from the register of ancillary qubits which gives the binary representation of the eigenvalue/energy of interest. Meanwhile, the $|\psi\rangle$ register is projected into the corresponding eigenstate $|E_0\rangle$.

The application of phase estimation on the near-term quantum devices, with less than 100 qubits and shallow circuits, are limited in the foreseeable future, because it requires a large overhead of ancillary qubits to achieve a acceptable precision, gate with high-fidelity as well as long coherence time to get a asymptotic approximation of the exact dynamics.

1.5.2 Variational quantum eigensolver

The variational quantum eigensolver (VQE) [57, 58, 59] is a hybrid approach that combines classical and quantum computation to solve problems in quantum chemistry. It aims to find the lowest energy state (ground state) of a molecular system. In the VQE scheme, as shown in Fig. 1.2, a variational ansatz is employed to prepare a quantum state that approximates the ground

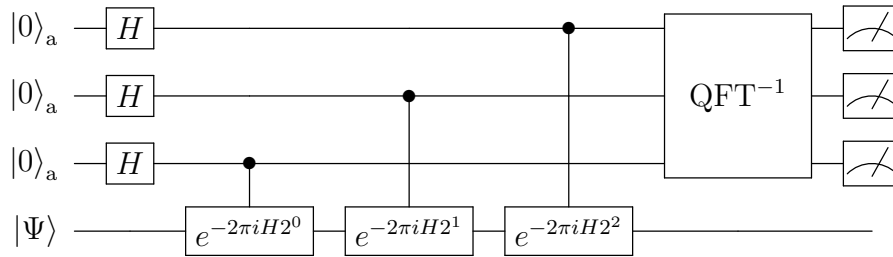


Figure 1.1: A circuit diagram for quantum phase estimation using three ancillary qubits. The circuit block labelled with QFT^{-1} executes the inverse quantum Fourier transformation. When the ancillary qubits are in state $|x\rangle$, a controlled rotation $e^{-2\pi i H x}$ is applied to the main register $|\Psi\rangle$. The ancillary qubits output an eigenvalue of H in binary when being measured in the computational basis; meanwhile the main register $|\Psi\rangle$ collapses to the corresponding eigenstate. The circuit diagram is adapted with permission from *Rev. Mod. Phys.*, 92(1):015003, 2020, DOI:[10.1103/revmodphys.92.015003](https://doi.org/10.1103/revmodphys.92.015003). Copyright 2020 American Physical Society.

state of the system. This ansatz is represented by a parameterized quantum circuit, where the parameters are adjusted iteratively to minimize the energy expectation value given by

$$E(\vec{\theta}) = \langle \psi_{\text{ref}} | U^\dagger(\vec{\theta}) \hat{H} U(\vec{\theta}) | \psi_{\text{ref}} \rangle. \quad (1.23)$$

where $\vec{\theta} = (\theta_1, \dots, \theta_n)^T$ denotes a vector of independent parameters in the circuit, and $\psi_{\text{ref}} = U_{\text{ref}} |\bar{0}\rangle$ is usually taken to be a mean-field or multi-reference state [60, 61, 62, 63, 64, 65] generated by non-parametrised gates on the initial all-zero state. The Rayleigh-Ritz variational principle guarantees that $E(\vec{\theta}) \geq E_0$ where E_0 is the exact ground-state energy. VQE harnesses the power of classical optimization algorithms to fine-tune the quantum circuit's parameters $\vec{\theta}$, while the energy expectation value is repeatedly measured on a quantum computer. Classical optimization algorithms, such as gradient-based

methods [66], are employed to update the parameters and search for the optimal configuration that minimizes the energy expectation value.

VQE provides an efficient way to approximate the ground state energy without the need for complete diagonalization of the Hamiltonian, which is often computationally expensive for large systems. The main advantage of VQE is that it can utilize shallow circuits, which leads to less demanding coherence time, with the cost of a polynomial overhead of measurements and classical optimization.

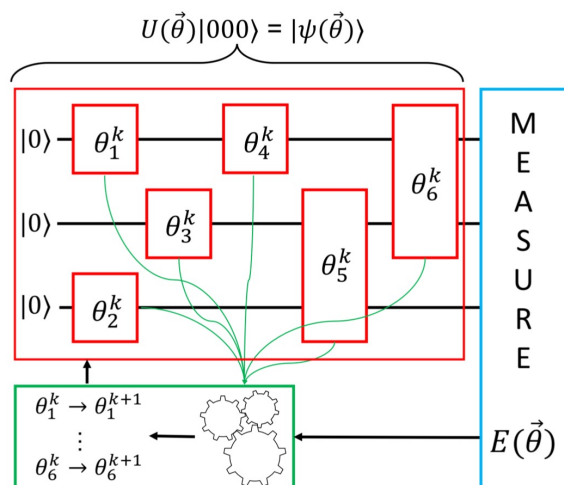


Figure 1.2: Scheme of the variational quantum eigensolver (VQE) using three qubits. The scheme is reprinted with permission from *Rev. Mod. Phys.*, 92(1):015003, March 2020, DOI:[10.1103/revmodphys.92.015003](https://doi.org/10.1103/revmodphys.92.015003). Copyright 2020 American Physical Society.

1.5.3 Quantum imaginary time evolution

As an alternative scheme to VQE, the quantum imaginary time evolution (QITE), an ansatz-independent optimization-free method, has been proposed to determine the eigenstates of a Hamiltonian on quantum computers [67].

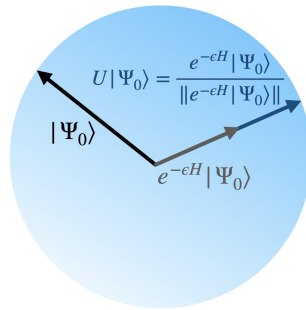


Figure 1.3: Schematic of the quantum imaginary time evolution (QITE) algorithm

QITE inherits the advantage of the classical imaginary time evolution method [68, 69] that allows correlations to build faster than the real-time evolution, which is limited by Lieb-Robinson bounds on the growth of correlation functions [70]. Propagating an initial state that has a non-zero overlap with the ground state in imaginary time, it is possible to converge to the exact ground state $|\Psi\rangle = \lim_{\beta \rightarrow \infty} \frac{|\Phi(\beta)\rangle}{\|\Phi(\beta)\|}$ (for $\langle \Phi(0) | \Psi \rangle \neq 0$). However, the imaginary-time propagator is nonunitary. As the basic operations allowed on quantum computers have to be unitary, the textbook implementation of a non-unitary operator is to use extra ancillary qubits with an increased number of measurements [50].

The key idea of QITE, as originally formalized by Motta and coworkers, is to map the action of the imaginary time evolution on a state to a unitary operator obtained by least-square fitting [67]. The fitting procedure involves solving linear equations in which matrix elements can be computed from projective measurements on the initial state without additional ancillary qubits.

The quantum imaginary time evolution algorithm is not limited to ground-state computations. Since its first proposal, it has been applied to estimate

finite temperature properties [71], simulate open quantum systems [72], prepare thermal states [73], and even extended to perform prime factorization [74] and simulate quantum field theories [75].

The depth of the QITE circuit grows exponentially with the correlation length of the system and linearly with the number of imaginary time steps. As for the measurement cost, the number of Pauli terms (same as the dimension of the linear system to be solved in the fitting) scales exponentially with the correlation length. Thus, with increasing system size, this rapidly becomes the bottleneck of the algorithm. For practical implementations, many techniques have been proposed to reduce the circuit complexity and measurement overhead. Sun *et al.* introduced circuit optimization by recompiling it using tensor networks [71]. Several works reported different strategies to combine unitary operators in the state preparation circuit effectively [76, 77, 78]. Some techniques have been developed to reduce the number of Pauli terms to be measured, such as exploiting Hamiltonian symmetries [71], randomized compiling [79], or utilizing a compact list of Pauli terms that arises in unitary-coupled-cluster-type exponential ansatz [76]. Another variant of QITE uses an adaptive scheme combining the variational ansatz simulation of imaginary time [80, 81] with the "action fitting" technique in QITE, which yields compact variational ansatz and a polynomial scaling of circuit depth with system size [82].

1.6 Outline of the dissertation

In Chapter 2, we propose a novel quantum algorithm for practical chemical simulations, termed multireference selected quantum Krylov (MRSQK) algorithm, which use the efficient unitary time evolution on quantum computers to generate compact quantum Krylov subspaces. In Chapter 3, we introduce a hybrid quantum-classical unitary downfolding scheme based on the driven similarity renormalization group theory (QDSRG). This method effectively reduces the dimensionality of the problem and minimizes the required quantum resources, which enables resource-efficient simulations on small-scale quantum computers using large basis sets. In Chapter 4, we extend the QDSRG scheme to compute excited states via a state-averaged formalism (SA-QDSRG), specifically targeting the challenging cases of near-degenerate states (i.e. conical intersections) that play a crucial role in describing photodynamic processes.

Chapter 2

A multireference quantum Krylov algorithm for strongly-correlated electrons

Part of this chapter is reprinted or adapted with permission from Nicholas H. Stair, Renke Huang, and Francesco A. Evangelista. *J. Chem. Theory Comput.*, 16(4):2236–2245, 2020, DOI:[10.1021/acs.jctc.9b01125](https://doi.org/10.1021/acs.jctc.9b01125). Copyright 2020 American Chemical Society.

Sec. [2.2](#), [2.3](#), [2.4](#) are mostly reprinted from the above publication; Table [2.3](#) is updated to show a comparison of energy errors directly. The introduction is rewritten while the topics covered remain unchanged. Sec. [2.1](#) is largely rewritten in a detailed and pedagogical way (hopefully), which is complementary to the *Theory* section of the above published paper. Sec. [2.5](#) and Sec. [2.6](#) summarize several preliminary results of follow-up works on the method.

Simulating fermions whose interactions display strong correlation effects on classical computers is plagued by the computational difficulties from the

exponential growth of many-body Hilbert space dimension.[4] This problem motivated the original idea of quantum computing.[1, 3] The past decade has witnessed the milestone achieved in the hardware development of the quantum computer,[83] so it has become crucial to realize useful applications to demonstrate the potential it promises. Current noisy intermediate-scale quantum (NISQ) devices,[52] characterized by 50 to several hundred qubits and low gate fidelity, limit the depth and width of quantum circuits that can be executed with sufficient confidence, which puts many constraints on the design of algorithms for quantum simulation.

Quantum computers have a prominent advantage for simulating quantum dynamics, the unitary time evolution of a highly-entangled state.[46] In the language of complexity class, this is known to be a **BQP** problem,[84, 46] which in theory can be efficiently solved by a quantum computer. The quantum algorithm combining unitary evolution and phase estimation, termed QPE, was the first to manifest the exponential speedup in solving the eigenvalue problem of a local hamiltonian,[85, 86] and adapted for fermionic simulations.[87, 88] QPE was then demonstrated on small molecules for calculating the ground-state energy,[56] and later extended to compute the complete spectrum on photonic hardware.[65, 89] However, for medium to large systems of chemical interest, such as FeMoco, the transition metal center in a nitrogenase enzyme, an estimate of circuit depth and coherence time needed for QPE is far beyond the reach of NISQ devices.[15] Promising alternatives tailored for the existing or near-term noisy hardware are hybrid quantum-classical algorithms. Two major schemes of this type are the variational quantum eigensolver (VQE)[57, 58, 59] and the quantum approximate optimiza-

tion algorithm (QAOA),[90] both of which are variational. It has been shown that variational methods are more error/noise resilient than QPE.[91, 84]

The VQE algorithm leverages the quantum computer only for the classically intractable task, namely, preparing an entangled quantum state by a parametrized circuit termed the ansatz, and obtaining the energy expectation from statistics of repetitive measurements of the state.[59] Then, a classical optimizer minimizes the energy and updates parameters iteratively. In this way, the VQE trades a polynomial overhead of measurements and classical optimization for a much shorter coherence time and a reduction of the circuit depth.[92] The most important wavefunction ansatz in the VQE scheme is the unitary coupled cluster truncated at single and double excitations (UCCSD),[59, 93, 94, 95] which is inspired by efforts in improving classical coupled cluster theory.[96, 97, 98, 99, 100, 101, 102] Several variants of UCCSD ansatz have been explored, including k -UpCCGSD approach which utilizes generalized singles and doubles,[103] qubit UCC constructed directly from entangler gates[104, 105] with qubit mean-field reference,[106] Bogoliubov UCC using fermionic Gaussian state reference,[61] an adaptive compact UCC with gradient-selected unitaries[107] and its hardware efficient variant.[108] Other alternatives, primarily, hardware-efficient ansatzes that only use the set of gates easily implementable on NISQ devices[109, 110, 111] also gain attention because of much shallower circuits. The VQE scheme has also been extended to compute excited-state properties,[91, 112, 113, 114, 115, 116, 117, 118] or combined with QPE to reduce the measurement cost.[119, 120] While VQE experiments have been realized on most existing hardware architectures,[57, 58, 93, 121, 113, 120, 122, 110] multiple

challenges nonetheless remain in practice – the difficulty of high-dimensional classical optimization of the energy,[123] a large number of measurements required for converging the expectation value to high precision[124] and intrinsic accuracy limit from the inexact ansatz.[125] Therefore, it is crucial to improve the VQE further or to develop other hybrid algorithms.

The idea of representing the Hamiltonian in a non-orthogonal subspace,[41] which has various practices in classical computational chemistry,[126, 127, 128, 129, 130, 131, 132, 133] has also been adopted in a class of quantum-classical algorithms referred to as Quantum Subspace Diagonalization (QSD).[91, 113, 67, 134, 135, 136, 137] The initial proposal of QSD, named quantum subspace expansion (QSE), aimed at extending the VQE scheme to compute excited states and mitigate errors.[91] In this work, the Hamiltonian is expanded in the configuration interactions singles (CIS) subspace $\hat{a}_i^\dagger \hat{a}_j ||\Psi\rangle$, and overlap matrix elements are three- and four-electron reduced density matrices measured in VQE experiments by operator averaging.[137] Then solving the generalized eigenvalue problem yields both the ground and excited states. Nevertheless, the CIS basis only expands a relatively small, restricted Hilbert space. Diagonalization of the possible noisy Hamiltonian matrices in this space might lead to systematic biases.[138] Huggins *et al.* developed another VQE-based QSD method, termed the non-orthogonal VQE (NOVQE) approach,[135] which uses separate VQE experiments to generate and optimize a set of non-orthogonal k -UpCCGSD type states[103] and diagonalizes the Hamiltonian in this basis. One motivation of this work is to ameliorate the difficulty of optimization in the context of VQE.

While many efforts in the QSD is to extend or augment the VQE scheme, the general QSD framework is likely to go beyond, specifically in terms of the great flexibility in the way to form the subspace. Motta *et al.* proposed the Quantum Lanczos (QLanczos) algorithm[67] which fills a Krylov subspace with basis vectors in powers of $e^{-2\Delta\tau H}$ such that $\mathcal{K} : \{|\Phi\rangle, e^{-2\Delta\tau H} |\Phi\rangle, e^{-4\Delta\tau H} |\Phi\rangle, \dots\}$. These basis vectors are obtained using the QITE algorithm,[67] which maps the Trotterized[139] imaginary-time propagator to a unitary operator scaled by the norm of the evolved state vector after a single Trotter time step. The matrix elements in the QLanczos are computed based on the expectations values of those mapped unitaries, which are available after direct measurements. Note that the QLanczos algorithm requires no classical optimization, and its convergence is guaranteed by properties of the imaginary-time evolution, free of fixed ansatz errors in its variational variant.[80] These advantages show that the QSD scheme provides viable solutions to circumvent problems that hinder the VQE methods.

Inspired by the QLanczos algorithm, we proposed a multireference selected quantum Krylov (MRSQK) method[140] based on real-time dynamics, and also provided the circuit to evaluate matrix elements efficiently by indirect measurements (the Hadamard test),[141] which is distinct from the expectation value measuring in the situation of both the QSE[91] and the QLanczos.[67] QSD methods that generate the non-orthogonal basis from a single state are likely to suffer from numerical instabilities due to the linear dependency of basis states.[67, 135] Thus, we initialized the QSD procedure with a set of orthogonal references. When completing this work, we noticed

a recent preprint paper by Parrish and McMahon[134] which shares part of the ideas employed in our work. They theorized a quantum filter diagonalization approach (QFD) in which the variational basis is generated by propagating several reference states approximately in real-time, which is motivated by classical filter diagonalization[142, 143, 144, 145] and time-grid-propagation based quantum algorithms.[146, 147, 148, 149] The QFD method is applied to simulate the spectrum of an 8-qubit *ab initio* exciton Hamiltonian, where they started with the zero configuration $|00\dots\rangle$ and all singly-excited configurations $\{|10\dots\rangle, |010\dots\rangle, \dots\}$, and propagated these references to form a time-grid subspace.[134]. While we utilized the same strategy to produce basis states from a single reference, our method has the novelty that real-time dynamics on the mean-field reference and measurements are also used to automatically select important configurations with large amplitudes out and add them to the set of references. The selection procedure preserves symmetries, such as the particle number, the total spin, the spatial symmetry, making it fit for the fermionic Hamiltonian, which is generally more complicated than the exciton model.

2.1 Methods

2.1.1 Basis in MRSQK

The multireference selected quantum Krylov method combined with real-time dynamics generates a $d(s + 1)$ -dimensional non-orthogonal Krylov space \mathcal{K} in

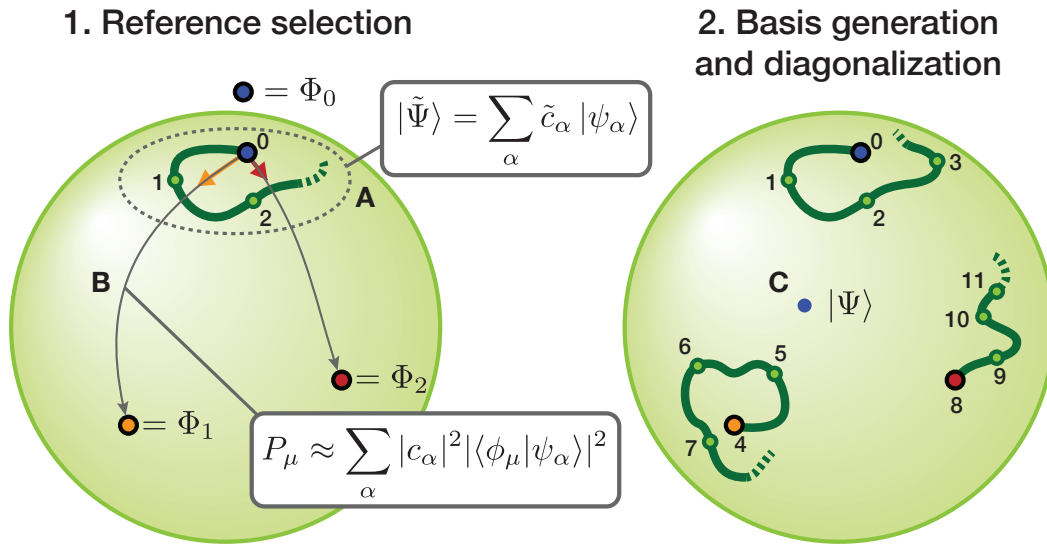


Figure 2.1: Schematic illustration of the multireference selected quantum Krylov (MRSQK) algorithm. (A) An approximate real-time dynamics using a single Slater determinant reference (Φ_0) is used to generate a trial state ($\tilde{\Psi}$). (B) Measurements of the determinants that comprise the trial state are used to determine the probability of hopping (P_μ) to other determinants. This information is employed to build two new reference states, Φ_1 and Φ_2 . (C) Finally, three real-time evolutions starting from the references (Φ_0, Φ_1, Φ_2) generate a set of 12 Krylov states ψ_α , which are used to diagonalize the Hamiltonian and obtain the energy of the state Ψ .

the form:

$$\begin{aligned}
 \mathcal{K} : & \{ |\Phi_0\rangle, e^{-i\Delta t\hat{H}} |\Phi_0\rangle, e^{-i2\Delta t\hat{H}} |\Phi_0\rangle, \dots, e^{-is\Delta t\hat{H}} |\Phi_0\rangle, \\
 & |\Phi_1\rangle, e^{-i\Delta t\hat{H}} |\Phi_1\rangle, e^{-i2\Delta t\hat{H}} |\Phi_1\rangle, \dots, e^{-is\Delta t\hat{H}} |\Phi_1\rangle, \\
 & \dots \\
 & |\Phi_{d-1}\rangle, e^{-i\Delta t\hat{H}} |\Phi_{d-1}\rangle, e^{-i2\Delta t\hat{H}} |\Phi_{d-1}\rangle, \dots, e^{-is\Delta t\hat{H}} |\Phi_{d-1}\rangle \}
 \end{aligned} \tag{2.1}$$

This is done in two procedures: *reference selection* and the *basis generation and diagonalization* (see Fig. 2.1).

The *reference selection* utilizes the real-time evolution of a single Slater de-

terminant $|\Phi_0\rangle$ (usually the Hartree–Fock reference) to determine other $(d-1)$ references. It starts with propagating $|\Phi_0\rangle$ at fixed intervals in real-time, which forms a trial time-grid basis $\{|\Phi_0\rangle, e^{-i\Delta t\hat{H}}|\Phi_0\rangle, e^{-i2\Delta t\hat{H}}|\Phi_0\rangle \dots\}$ with $(s'+1)$ dimension. The ground state of the Hamiltonian in this trial basis is written as

$$|\tilde{\Psi}_0\rangle = \sum_{k=0}^{s'} C_{0k} e^{-ik\Delta t\hat{H}} |\Phi_0\rangle = \sum_{k=0}^{s'} C_{0k} |k\rangle \quad (2.2)$$

We use Jordan-Wigner transform[53] to map the fermionic Fock space to the Hilbert space of qubits.[150] In this mapping, a Slater determinant in the Fock space is represented by a qubit computational basis state that has the same binary representation. Note that the algorithm is agnostic to the encoding method, but in order to give a chemically-intuitive picture, that determinants (fermionic basis states) and computational basis states are the same in the Jordan-Wigner encoding, we can conveniently view these two bases equivalently in the following explanation. Each time-grid basis vector $|k\rangle$ can be written as a linear combination of n -qubit computational basis states (Slater determinants) $|k\rangle = \sum_{\mu} C_{k\mu} |\mu\rangle$. Then, the trial ground state vector can be decomposed in the computational basis

$$|\tilde{\Psi}_0\rangle = \sum_{k=0}^{s'} \sum_{\mu=0}^{2^n-1} C_{0k} C_{k\mu} |\mu\rangle \quad (2.3)$$

Based on Eq. 2.3, the probability of measuring the determinant $|\mu\rangle$ in the trial ground state $|\tilde{\Psi}_0\rangle$ is given by $P_{\mu} = |\sum_{k=0}^{s'} C_{0k} C_{k\mu}|^2$. $|\tilde{\Psi}_0\rangle$ can also be written in a compact way as the Hadamard product[151] (element-wise multiplication) of three vectors $|\tilde{\Psi}_0\rangle = \sum_k \mathbf{C}_0 \circ \mathbf{C}_k \circ \vec{\mu}$, where $\vec{\mu}$ comprises all the n -qubit

computational basis states $\vec{\mu} = (|0\rangle, |1\rangle, \dots, |2^n - 1\rangle)$.

The coefficient vector $\mathbf{C}_0 = (C_{00}, C_{01}, \dots, C_{0s'})$ is obtained by solving the generalized eigenvalue problem,

$$\mathbf{HC} = \mathbf{SCE} \quad (2.4)$$

with matrix elements given by

$$S_{\alpha\beta} = \langle \Phi_0 | e^{i\alpha\Delta t \hat{H}} e^{-i\beta\Delta t \hat{H}} | \Phi_0 \rangle, \quad H_{\alpha\beta} = \langle \Phi_0 | e^{i\alpha\Delta t \hat{H}} \hat{H} e^{-i\beta\Delta t \hat{H}} | \Phi_0 \rangle, \quad (2.5)$$

where $\alpha, \beta \in [0, 1, \dots, s']$. \mathbf{C}_0 is the eigenvector corresponding to the lowest eigenvalue.

\mathbf{C}_k is the state vector of the quantum state $|k\rangle = e^{-ik\Delta t \hat{H}} |\Phi_0\rangle = \sum_{\mu} C_{k\mu} |\mu\rangle$, which can be simulated classically (e.g. statevector simulator in the Qiskit-Aer package). However, in real experiments, the state vector cannot be directly read out from the quantum computer. Available quantities from projective measurements on a quantum state are $\mathbf{bin}(\mu)$, the binary representation of the determinant $|\mu\rangle$ to which the state collapses after measuring $|k\rangle$ in the computational basis, and $|C_{k\mu}|^2$, the probability of getting $|\mu\rangle$. [51] While the exact value of any $C_{k\mu}$, which is complex in general, can not be determined, we can nonetheless use $|C_{k\mu}|^2$ to upper bound the probability of sampling the determinant $|\mu\rangle$ in the trial ground state $|\tilde{\Psi}_0\rangle$:

$$P_{\mu} = \left| \sum_{k=0}^{s'} C_{0k} C_{k\mu} \right|^2 \leq \sum_k |C_{0k}|^2 |C_{k\mu}|^2 \quad (2.6)$$

which follows from the Cauchy-Schwarz inequality. The upper bound expres-

sion is adopted in practice for the probability estimation. To make it more explicitly, we prepare time-grid basis states $\{|k\rangle\}$ separately on multiple quantum computers. Each quantum computer outputs a probability distribution $\{|C_\mu|^2\}_\mu$ of determinants. The overall probability of a single $|\mu\rangle$ is computed as the weighted sum over the probability of $|\mu\rangle$ in each time-grid basis state. Note that we only use the value of P_μ to select important states, so a qualitatively correct measurement statistics of the time-evolved state is sufficient for our need, which means not many measurement repetitions are required.

Through finite measurements, we form a coarse aggregate of important determinants and sort them in descending order according to the overall probability. Next, the set is refined, such that only determinants with the same particle number as $|\Phi_0\rangle$ are kept. Then, we enforce the total spin symmetry by leaving the closed-shell configurations alone as one state, grouping open-shell configurations with the same spin occupation pattern to zero out the total spin, summing their weights, and normalizing the obtained multi-configurational states. Lastly, we select $d - 1$ largest-weighted states, together with $|\Phi_0\rangle$, to form our reference set $\{|\Phi_I\rangle\}_{I=0}^{d-1}$.

We then generate the full basis with the states sampled at fixed intervals when evolving each reference. Diagonalizing the Hamiltonian in the entire $d(s+1)$ -dimensional space \mathcal{K} requires solving Eq. 2.4 again, with more general matrix representations of the overlap \mathbf{S} and the Hamiltonian \mathbf{H} given by

$$S_{I(s+1)+\alpha, J(s+1)+\beta} = \langle \Phi_I | e^{i\alpha\Delta t\hat{H}} e^{-i\beta\Delta t\hat{H}} | \Phi_J \rangle, \quad (2.7)$$

$$H_{I(s+1)+\alpha, J(s+1)+\beta} = \langle \Phi_I | e^{i\alpha\Delta t\hat{H}} \hat{H} e^{-i\beta\Delta t\hat{H}} | \Phi_J \rangle \quad (2.8)$$

where $\alpha, \beta \in [0, 1, \dots, s]$, $I, J \in [0, 1, \dots, d - 1]$, indices are consistent with the basis ordering in Eq. 2.1.

2.1.2 State Preparation

Given a qubit Hamiltonian after the Jordan-Wigner[53] or the Bravyi-Kitaev encoding, [55, 54] in general, not all Pauli terms (tensor products of Pauli operators) in the Hamiltonian commute.

$$\hat{H} = E_0 + \sum_l^N h_l \bigotimes_{k=1}^n \sigma_k^{\{I,X,Y,Z\}} \quad (2.9)$$

One may realize the time evolution operator $e^{-it\hat{H}}$ on a quantum computer following the widely-used first order Lie-Trotter-Suzuki product approximation[139, 152, 153] or higher-order product formulae[154, 155]. Other more sophisticated methods include truncated Taylor series expansions,[156, 157] linear combinations of unitaries (LCU),[158] Chebyshev polynomial approximations,[159] or the recently proposed qubitization[160, 161] in conjunction with quantum signal processing[162] methods. In our case, the first-order Lie-Trotter-Suzuki product with m Trotter steps (numbers) is employed

$$e^{-it\hat{H}} = \left(\prod_l^N e^{-i\frac{th_l}{m} \otimes_k \sigma_k} \right)^m + O\left(\frac{(th_l)^2}{m}\right) \quad (2.10)$$

The error in approximating $e^{-it\hat{H}}$ using product formula is determined by both the number of Trotter steps and the Trotter order. In the first-order Trotter-Suzuki formula, the number of Trotter steps required for a simulation error of

ϵ scales as $m = O((th_l)^2/\epsilon)$, so m should be large to suppress approximation errors.

It has been observed that in practice, the first order Trotter-Suzuki product gives errors in the ground state energy scaling as $1/m^2$, [163] same as that of second-order Trotter-Suzuki approximation. Therefore, considering both the error scaling and the state preparation cost, the first-order formula that has much shorter circuits is favorable.

We argue that the MRSQK method is likely to achieve better error scaling than the Trotter error, because it has the variational optimization of the state when solving the generalized eigenvalue problem in a subspace, while variational methods are shown to be resilient to errors to some extent. [59, 93]

2.1.3 Quantum Circuits for Measuring Matrix Elements

In order to compute matrix elements on quantum devices, we use a modified Hadamard test [164, 50] (shown in Fig. 2.2) to measure observables indirectly with the help of one ancilla qubit. To explain it more detailedly, we reformulate Eq. 2.7 and Eq. 2.8, denoting collective indices $\gamma = (I, \alpha)$, $\chi = (J, \beta)$, and the l -th tensor product in the qubit Hamiltonian $\hat{P}_l = \bigotimes_{k=1}^n \sigma_k^{\{I,X,Y,Z\}}$

$$\begin{aligned} S_{\gamma\chi} &= \langle \bar{0} | \hat{U}_I^\dagger \left(\prod_l e^{i\frac{\alpha\Delta th_l}{m} \hat{P}_l} \right)^m \left(\prod_l e^{-i\frac{\beta\Delta th_l}{m} \hat{P}_l} \right)^m \hat{U}_J | \bar{0} \rangle \\ &= \langle \bar{0} | \hat{U}_I^\dagger \hat{U}_\alpha^\dagger \hat{U}_\beta \hat{U}_J | \bar{0} \rangle = \langle \bar{0} | \hat{U}_\gamma^\dagger \hat{U}_\chi | \bar{0} \rangle \end{aligned} \quad (2.11)$$

$$\begin{aligned}
H_{\gamma\chi} &= \langle \bar{0} | \hat{U}_I^\dagger \left(\prod_l e^{i\frac{\alpha\Delta t h_l}{m} \hat{P}_l} \right)^m \hat{H} \left(\prod_l e^{-i\frac{\beta\Delta t h_l}{m} \hat{P}_l} \right)^m \hat{U}_J | \bar{0} \rangle \\
&= E_0 \langle \bar{0} | \hat{U}_\gamma^\dagger \hat{U}_\chi | \bar{0} \rangle + \sum_l^N h_l \langle \bar{0} | \hat{U}_\gamma^\dagger \hat{P}_l \hat{U}_\chi | \bar{0} \rangle
\end{aligned} \tag{2.12}$$

\hat{U}_I, \hat{U}_J are unitary oracles that output reference states. For a single determinant (one computational basis state), $\hat{U}_{\{I,J\}}$ comprises one layer of X gates. Protocols for constructing multi-determinant states are proposed [63, 62, 165] with linear scaling in the number of qubits. In the most general case when matrix elements are between basis states that evolve from different references $|\Phi_I\rangle, |\Phi_J\rangle$, we need to implement the controlled reference oracles $c\text{-}\hat{U}_{\{I,J\}}$, which have two-qubit gates at the same scaling as single-qubit gates in $\hat{U}_{\{I,J\}}$. While for matrix elements between states from the same reference $|\Phi_I\rangle$, we simplify Eq. 2.11, 2.12 as $S_{\gamma\chi} = \langle \Phi_I | \hat{U}_\alpha^\dagger \hat{U}_\beta | \Phi_I \rangle$, $H_{\gamma\chi} = E_0 \langle \Phi_I | \hat{U}_\alpha^\dagger \hat{U}_\beta | \Phi_I \rangle + \sum_l h_l \langle \Phi_I | \hat{U}_\alpha^\dagger \hat{U}_\beta | \Phi_I \rangle$, where only the series of exponentials of \hat{P}_l are included in the controlled unitaries, with $\hat{U}_{\{I=J\}}$ gulped in the main register state preparation.

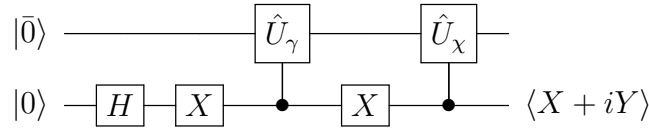


Figure 2.2: Hadamard test circuit to estimate expectation values of unitary operators with a general form of $\langle \bar{0} | \hat{U}_\gamma^\dagger \hat{U}_\chi | \bar{0} \rangle$. Measuring the X, Y operators on the ancillary qubit $|0\rangle$, one can obtain the mean value of $X + iY = 2 |0\rangle \langle 1|$, which equals to $\langle X + iY \rangle = \langle \bar{0} | \hat{U}_\gamma^\dagger \hat{U}_\chi | \bar{0} \rangle$

The method to exponentiate tensor products of Pauli gates is described in

Ref. [54, 163]. The exponential of one $\hat{P}_l = \bigotimes_k \sigma_k$ is given by

$$e^{-it_l \bigotimes_k \sigma_k} = \left(\bigotimes_{k=1}^n H_k^\dagger \right) \left(\prod_{i=1}^{n-1} \text{CNOT}_{i,i+1} \right) e^{-it_l \sigma_n^Z} \left(\prod_{i=n-1}^1 \text{CNOT}_{i,i+1} \right) \left(\bigotimes_{k=1}^n H_k \right)$$

where H_k gates perform transformations between the eigenbasis of σ^X or σ^Y and σ^Z , i.e. $H_k^\dagger \sigma^{\{X,Y\}} H_k = \sigma^Z$, $t_l = \alpha \Delta t h_l / m$ and $e^{-it_l \sigma_n^Z} = R_z(2t_l)$ represents the Z rotation gate on the qubit with the largest index.

For applying $e^{-it_l \bigotimes_k \sigma_k}$ on the main register controlled by the ancillary qubit, we only need to replace the $R_z(2t_l)$ with a controlled $R_z(2t_l)$ on the last qubit, as illustrated in Fig. 2.3. In this way, l terms in a single Trotter step are executed sequentially. For larger Trotter number m , we just run m replicas of l -terms in series.

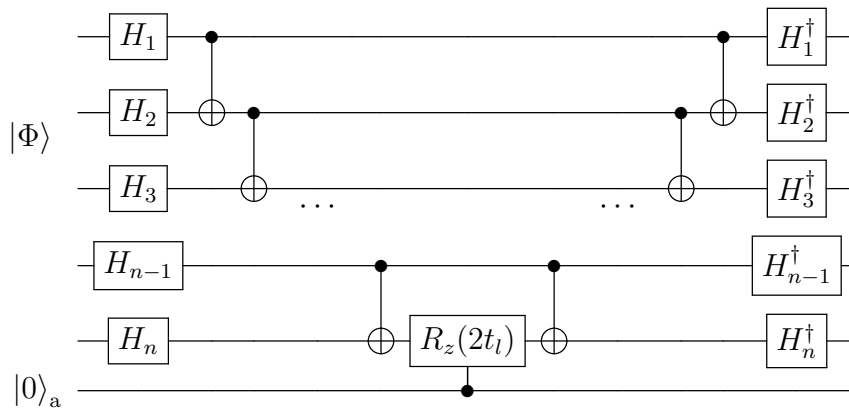


Figure 2.3: Circuit for applying one controlled $-e^{-it_l \bigotimes_k \sigma_k}$ operator.

To give readers an idea of how to construct such circuits in practice, we demonstrate an example circuit to compute several matrix elements for a two-qubit molecular H_2 Hamiltonian[93] using the spin symmetry-enforced Bravyi-Kitaev transformation,[166, 167] at the bond length of 0.75 Å. Coefficients h_l are computed in STO-3G basis given in Table I of the supplementary

information of Ref. [113].

$$\hat{H}_q = -0.349833 - 0.388748\sigma_0^Z + 0.181771\sigma_0^X\sigma_1^X - 0.388748\sigma_1^Z + 0.011177\sigma_0^Z\sigma_1^Z$$

Four determinants are mapped to computational basis states explicitly as $|00\rangle = a_{0\alpha}^\dagger a_{0\beta}^\dagger |\text{vac}\rangle$, $|01\rangle = a_{0\alpha}^\dagger a_{1\beta}^\dagger |\text{vac}\rangle$, $|10\rangle = a_{1\alpha}^\dagger a_{0\beta}^\dagger |\text{vac}\rangle$, $|11\rangle = a_{1\alpha}^\dagger a_{1\beta}^\dagger |\text{vac}\rangle$. The Hartree–Fock state for this Hamiltonian is $|\Phi_0\rangle = |00\rangle$. A normalized spin adapted Krylov basis reference state is given by $|\Phi_1\rangle = (|01\rangle + |10\rangle)/\sqrt{2}$. The MRSQK parameters used in evaluating one matrix element are set, with the time grid $\Delta t = 0.1$, the number of Trotter step(s) $m = 1$. We take two off-diagonal matrix elements as examples, which are overlaps between Krylov basis state $|\Phi_1\rangle$ and $e^{-i\Delta t\hat{H}_q}|\Phi_1\rangle$, $e^{-i\Delta t\hat{H}_q}|\Phi_0\rangle$ and $|\Phi_1\rangle$. Hadamard test circuits with one-step Trotter-Suzuki approximation to compute $\langle\Phi_1|e^{-i\Delta t\hat{H}_q}|\Phi_1\rangle$ and $\langle\Phi_0|e^{i\Delta t\hat{H}_q}|\Phi_1\rangle$ by estimating $\langle X + iY \rangle_{\text{anc}}$ are shown in Fig. 2.4, where the ancilla qubit is measured to obtain $\langle Y \rangle$. Substituting the final $U2(\pi/2, -\pi/2)$ gates with Hadamard gates in two circuits will give $\langle X \rangle$.

2.1.4 Cost Estimation

The quantum computational cost of the MRSQK method is dominated by the number of two-qubit gates in the controlled Hamiltonian exponentials, especially the CNOT gates. Here we present a rough estimate of the gate counts in measuring matrix elements at the minimal Trotter step ($m = 1$), summarized in Table 2.1.

The concept of circuit depth can be interpreted as layers in a circuit.[51] The layer counting follows the rule that the set of gates that can be executed

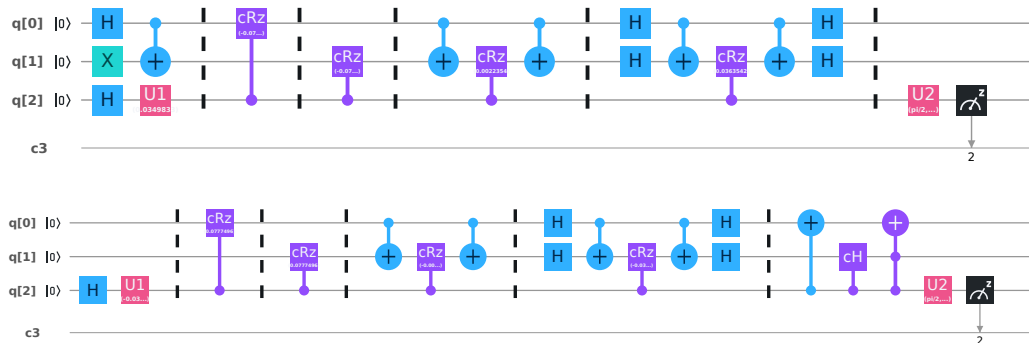


Figure 2.4: The circuit to compute $\langle \Phi_1 | e^{-i\Delta t \hat{H}_q} | \Phi_1 \rangle$ (top) and $\langle \Phi_0 | e^{i\Delta t \hat{H}_q} | \Phi_1 \rangle$ (bottom) implemented using Qiskit[168]. **q[0]**, **q[1]** encode basis states for the Hamiltonian, while **q[2]** is the ancillary qubit, with **c3** the classical bit to store the output from measuring **q[2]**. $U2(\pi/2, -\pi/2)$ gate before the measurement is the H_k gate rotating the state of ancillary qubit into the σ^Y basis.

Table 2.1: Resource estimates for MRSQK calculations with $m = 1$ Trotter step approximation on several hydrogen systems in STO-6G basis at the bond length $R=1.5$ Å. Jordan-Wigner transformation is used to encode the Hamiltonian for all cases in the table.

	H ₂	H ₄ (linear)	H ₄ (ring)	H ₆ (linear)	H ₆ (ring)	H ₈ (linear)
Num. of qubits	4	8	8	12	12	16
Num. of Pauli terms	14	184	92	918	702	2912
Num. of H/R_{zy} (H_k) gates	16	480	224	2832	2240	9664
Num. of one-qubit gate layers	8	296	112	1680	1248	5552
Num. of CNOT gates	36	1328	520	9972	7476	41600
Num. of c - R_z gates	14	184	92	918	702	2912
Num. of total layers	58	1808	724	12570	9426	50064

concurrently in parallel contributes one layer of the circuit. It is clear that in the c - e^{-iHt} circuit we are interested in, the number of layers of single-qubit basis change gates H_k are roughly half of the total one-qubit gate counts, while each two-qubit gate adds one layer to the circuit, because they need to run sequentially in the time order. Denoting the number of terms (each term

denotes one tensor product of single-qubit Pauli gates) in the Hamiltonian N , the weight of each term w_l (the number of non-identity (σ^I) Pauli gates in one term), the Trotter number m , a boolean quantity δ_l^Z that sets to 1 if at least one Pauli gate in the tensor product is σ^X or σ^Y , else sets to 0, we give estimates of gate counts by

$$\begin{aligned}\bar{N}_{1-q} &= m \sum_l^N 2w_l \\ \bar{N}_{\text{CNOT}} &= m \sum_l^N 2(w_l - 1) \\ \bar{N}_{R_z} &= Nm \\ \bar{N}_{\text{layer}} &= m \sum_l^N (2w_l + 2\delta_l^Z - 1).\end{aligned}\tag{2.13}$$

Note that all the numbers in the table serve as upper bounds for the implementation in practice, because we analyze the case when the number of qubits is equal to the number of spin orbitals with the active space spanning the whole molecular orbital space. Also, a direct application of the Jordan-Wigner transformation retains some redundant degrees of freedom in the qubit Hamiltonian. Some advanced encoding techniques enable the quantum simulation with fewer qubits. For example, Temme *et al.* [167] described a transform to remove qubits in the presence of \mathbb{Z}_2 symmetries. On the other hand, these circuits can be further compressed and compiled. By carefully choosing the term order, it is likely to cancel some basis change gates H_k and CNOT gates between two adjacent term exponentials, because all quantum gates are unitary and reversible. In this way, the number of gates will be much fewer than

the ones reported in the table.

In short, the depth of these circuits scales at worst $\mathcal{O}(mK^4)$ where m is the trotter number and K is the number of molecular orbitals. At the minimal Trotter number level ($m = 1$), the maximum circuit depth for MRSQK is comparable to that of UCC with generalized singles and doubles (employing the same Trotter number), and far shallower than QPE. More importantly, the circuit depth of MRSQK is independent of size of the Krylov basis one wishes to generate, allowing for a flexible trade off-between quantum and classical cost (for a desired level of accuracy). For example, in the NISQ device era, one may avoid larger circuit depths with MRSQK by employing a modest Trotter number, but still achieve a high degree of accuracy by building a larger Krylov space that will be diagonalized classically. In this way MRSQK has both the advantage of selected CI to exploit wave function sparsity and the classical compression afforded by its quantum computational subroutines. This flexibility is a feature that distinguishes MRSQK from other QSD methods.

2.2 Computational Details

The MRSQK method was implemented using both an exact second quantization formalism and a quantum computer simulator using the open-source package QForte.[169] All calculations used restricted Hartree–Fock (RHF) orbitals generated with Psi4[170] using a minimal (STO-6G)[171] basis. Molecular Hamiltonians for the hydrogen and BeH₂ systems were translated to a qubit representation via the Jordan–Wigner transformation as implemented in OpenFermion[172] with default term ordering. For all calculations, ref-

ferences in MRSQK were selected using initial QK calculations with $s_0 = 2$ evolutions of the Hartree–Fock determinant and a time step of $\Delta t = 0.25$ a.u. Parameters such as the time step (Δt), and number of evolutions per reference (s) used in MRSQK were chosen based on energy accuracy and numerical stability. We also note that we take the Trotter approximation with $m = 100$ as a good approximation to the infinite m limit for the potential energy curves we plot. The generalized eigenvalue problem has been solved using a canonical orthogonalization where only eigenvalues of \mathbf{S} above 1.0×10^{-7} were considered.

2.3 Results and Discussion

We benchmark the performance and comparative numerical stability of the MRSQK algorithm with linear chains of six and eight hydrogen atoms, two well-known models for one-dimensional materials with correlation strength modulated by bond length.[173, 174, 175, 176] We utilize point-group symmetry, which results in a determinant space comprised of 200 and 2468 determinants for H_6 and H_8 , respectively. We first consider H_6 at a site-site distance of 1.50 \AA , which exhibits strong electron correlation, as indicated by the large correlation energy ($E_{\text{corr}} = -0.24681 E_h$) and the small weight of the Hartree–Fock determinant in the FCI expansion ($|C_{\text{HF}}|^2 = 0.634$).

In Table 2.2 we show a comparison of the energy and overlap matrix condition number for the single reference version of quantum Krylov (QK), taking only the HF determinant as a reference, and MRSQK as a function of the total number of basis states. For H_6 we observe that in both the single and multiref-

Table 2.2: Ground-state energies (in E_h) of H_6 and H_8 at a site-site distance of 1.5 Å using exact time-evolution. Energy and overlap condition number $k(\mathbf{S})$ results are given for a single determinant (QK) using N Krylov basis states and $\Delta t = 0.5$. MRSQK results are given for $N = d(s + 1)$ Krylov basis states using three steps ($s = 3$) and $\Delta t = 0.5$ a.u. With N greater than 12 states, the condition number for QK does not grow larger than 10^{18} . This is likely a result of limitations of double precision arithmetic.

N	E_{QK}	$k(\mathbf{S}_{\text{QK}})$	E_{MRSQK}	$k(\mathbf{S}_{\text{MRSQK}})$
H_6 ($r_{\text{HH}} = 1.5 \text{ \AA}$)				
4	-3.015510	3.29×10^5	-3.015510	3.29×10^5
8	-3.019768	3.60×10^{11}	-3.019301	4.86×10^5
12	-3.020172	1.61×10^{17}	-3.019696	9.39×10^5
16	-3.020192	3.19×10^{17}	-3.019835	5.68×10^6
20	-3.020198	3.86×10^{17}	-3.019929	6.23×10^6
FCI	-3.020198			
H_8 ($r_{\text{HH}} = 1.5 \text{ \AA}$)				
4	-4.017108	1.19×10^5	-4.017108	1.19×10^5
8	-4.026563	1.39×10^{10}	-4.024268	1.50×10^5
12	-4.028000	5.11×10^{14}	-4.025894	2.00×10^5
16	-4.028096	1.33×10^{17}	-4.026042	2.51×10^5
20	-	-	-4.026387	4.27×10^5
24	-	-	-4.026457	4.44×10^5
FCI	-4.028152			

erence cases, convergence to chemical accuracy (error less than $1 \text{ kcal mol}^{-1} = 1.594 \text{ m}E_h$) is achieved with only 8 parameters, an order of magnitude smaller than the size of FCI space. For the case $N = 12$, MRSQK identifies the

following three references

$$\begin{aligned}
 |\Phi_0\rangle &= |220200\rangle \\
 |\Phi_1\rangle &= |200220\rangle \\
 |\Phi_2\rangle &= -0.302 |2 \uparrow\uparrow\downarrow\downarrow 0\rangle - 0.302 |2 \downarrow\downarrow\uparrow\uparrow 0\rangle \\
 &\quad + 0.275 |2 \uparrow\downarrow\uparrow\downarrow 0\rangle + 0.577 |2 \uparrow\downarrow\downarrow\uparrow 0\rangle \\
 &\quad + 0.577 |2 \downarrow\uparrow\uparrow\downarrow 0\rangle + 0.275 |2 \downarrow\uparrow\downarrow\uparrow 0\rangle
 \end{aligned} \tag{2.14}$$

where the orbitals are ordered according to $(1a_g, 2a_g, 3a_g, 1b_{1u}, 2b_{1u}, 3b_{1u})$ in the D_{2h} point group. These references are comprised of two closed-shell and six open-shell determinants. If we perform a computation with a set of references consisting of eight individual (uncontracted) determinants, the resulting Krylov space has dimension 32 and the corresponding energy is $-3.019797 E_h$, which is only $0.1 mE_h$ lower than the contracted result (-3.019696). Turning to H_8 , we find that the single-reference QK energy converges to chemical accuracy with only 12 parameters, two orders of magnitude fewer than FCI. For the same example, the MRSQK energy error is $1.06 \text{ kcal mol}^{-1}$ with 24 parameters, only slightly higher than chemical accuracy.

The linear dependency of the basis for H_6 and H_8 —as measured by the condition number of the overlap matrix $[k(\mathbf{S})]$ —is significantly more pronounced in the single reference QK than the MRSQK version. In the case of H_6 , even with a small Krylov basis (8 elements), QK is potentially ill-conditioned $[k(\mathbf{S}) = 3.60 \times 10^{11}]$. In the case of 12 (or more) states, the QK eigenvalue problem is strongly ill-conditioned $[k(\mathbf{S}) = 1.16 \times 10^{17}]$, while MRSQK dis-

plays only a modest condition number, $[k(\mathbf{S}) = 9.39 \times 10^5]$. Importantly, QK becomes ill-conditioned before reaching chemical accuracy, whereas MRSQK does not, highlighting the importance of multireference approach for practical applications.

Table 2.3: The energy error (in mE_h) of the ground-state (in E_h) of H_6 at a bond distance of 1.5 Å. MRSQK results are given for $N = d(s+1)$ Krylov basis states using three steps ($s = 3$) and $\Delta t = 0.5$ a.u. The quantity m indicates the Trotter number. For each value of N , selected configuration interaction (sCI) results were obtained using N determinants with the largest absolute coefficient in the FCI wave function. ADAPT-VQE results show the energy with N cluster amplitudes selected from the pool of spin-adapted generalized singles/doubles. All energy errors are computed with respect to the FCI energy ($-3.020198 E_h$).

Method	N				
	4	8	12	16	20
MRSQK ($m = \infty$)	4.804	0.903	0.51	0.456	0.276
MRSQK ($m = 8$)	7.762	1.827	1.195	1.047	0.763
MRSQK ($m = 4$)	12.93	4.031	2.666	2.471	1.645
MRSQK ($m = 2$)	24.074	9.444	5.963	5.727	3.503
MRSQK ($m = 1$)	37.329	16.171	9.776	9.297	5.337
sCI	175.196	110.794	93.861	65.611	58.426
ADAPT-VQE	113.474	37.156	24.507	17.853	11.351

Next, we assess the errors introduced by approximating the real-time dynamics with a Trotter approximation. Table 2.3 shows the performance of MRSQK using various levels of Trotter approximation for H_6 at a bond distance of 1.5 Å. We compute the energy errors (in mE_h) with respect to the FCI energy. While using exact time evolution affords the fastest energy convergence with respect to the number of Krylov basis states, we find that chemical accuracy can still be achieved using Trotter approximation. For example, using a finite Trotter number $m = 8$, MRSQK gives an error of $1.2 mE_h \approx$

0.03 eV using only 12 Krylov states. In Table 2.3 we also show a comparison of MRSQK with selected configuration interaction (sCI) and the adaptive derivative-assembled pseudo-Trotter ansatz variational quantum eigensolver (ADAPT-VQE).[107] For any Trotter numbers, MRSQK converges significantly faster than sCI and the ADAPT-VQE method. For example, even with the smallest Trotter number ($m = 1$) MRSQK with 20 Krylov states gives an error of $5.4 mE_h$, while a sCI wave function with 20 determinants yields an error of $58.4 mE_h$ (see Table 2.3 for details of the determinant selection). In comparison, an ADAPT-VQE wave function with 20 parameters yields an error of $11.4 mE_h$. These results demonstrate the ability of MRSQK to parameterize strongly correlated states efficiently using a small fraction of the variational degrees of freedom.

To illustrate the ability of MRSQK to determine accurate ground-state potential energy surfaces (PES) in the presence of strong correlation, we examine the dissociation of the H_6 chain and linear BeH_2 . Figure 2.5 show the energy and error with respect to FCI for H_6 , for restricted Hartree–Fock (RHF), second-order Møller–Plesset perturbation theory (MP2), coupled cluster with singles and doubles (CCSD),[177] and MRSQK with a Krylov basis of 20 states ($s = 3, d = 5$). With the onset of strong electron correlation, single-reference methods (RHF, MP2, CCSD) fail to capture the the correct qualitative features of the PEC. For example, CCSD produces very accurate results near the equilibrium geometry; however, it dips significantly below the FCI energy for bond distances greater than 1.5 \AA . In contrast, MRSQK far outperforms CCSD even with the lowest Trotter number ($m = 1$) and chemically accurate MRSQK results are obtained with $m = 8$.

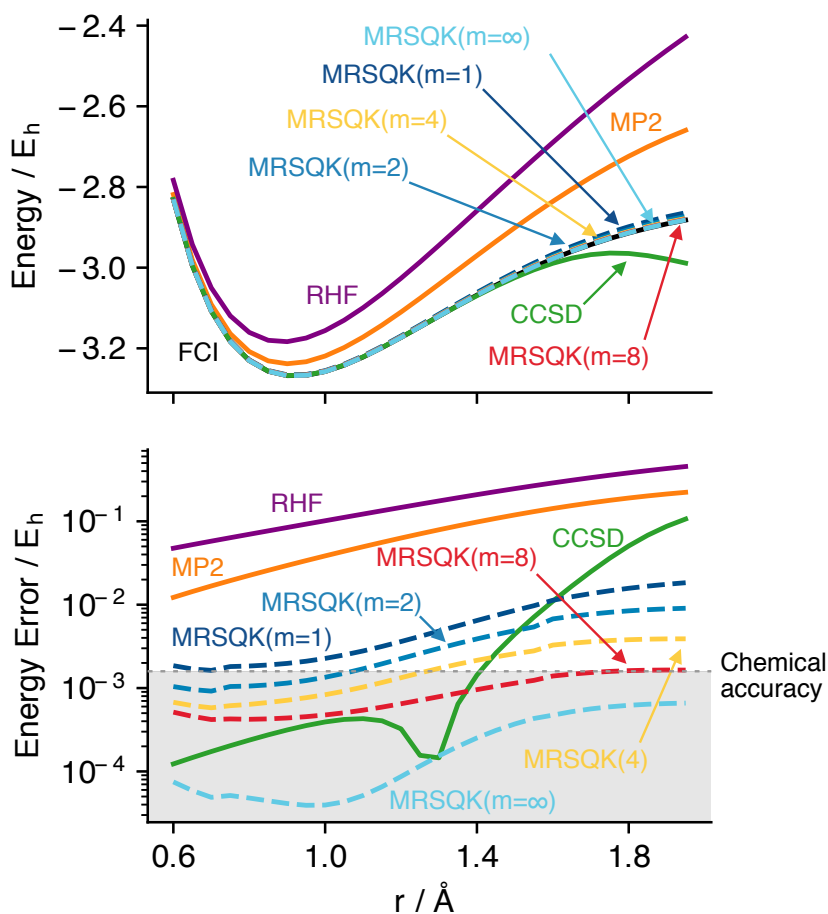


Figure 2.5: Potential energy curve (top) and error (bottom) for symmetric dissociation of linear H₆ in a STO-6G basis. MRSQK computations use $\Delta t = 0.5$ a.u., three time steps ($s = 3$), and five references ($d = 5$) corresponding to 20 Krylov basis states. The number of Trotter steps (m) is indicated in parentheses, while those from exact time evolution are labeled ($m = \infty$).

In Figure 2.6 we report the potential energy curve for the symmetric dissociation of linear BeH₂. For this problem, the size of the determinant space is 169. Like H₆, BeH₂ is a challenging problem for single-reference methods,

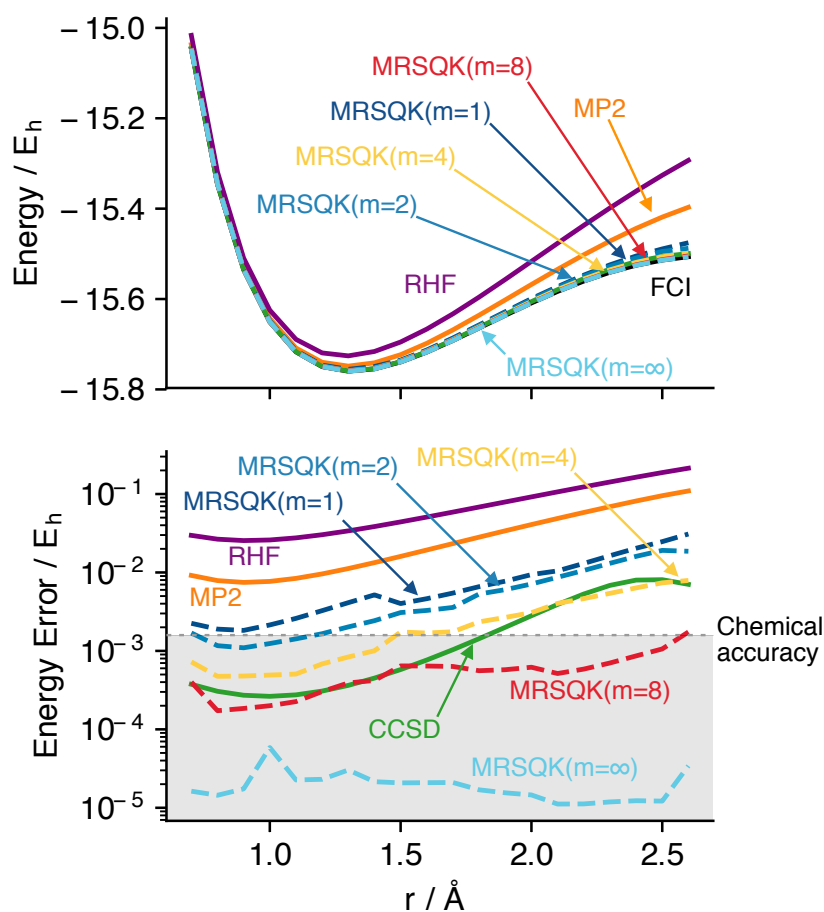


Figure 2.6: Potential energy curve (top) and error (bottom) for symmetric dissociation of linear BeH_2 in a STO-6G basis. MRSQK computations use $\Delta t = 2$ a.u., four time steps ($s = 4$), and six references ($d = 6$) corresponding to 30 Krylov basis states. The number of Trotter steps (m) is indicated in parentheses, while those from exact time evolution are labeled ($m = \infty$).

although CCSD shows smaller errors (less than $10 mE_h$) throughout the entire curve. MRSQK computations on BeH_2 employed 30 Krylov states generated by a space of six references and four time steps ($s = 4$). For this problem,

we found that using a larger time step provides more accurate results and therefore, we report results using $\Delta t = 2$ a.u. In the case of no Trotter approximation ($m = \infty$), the MRSQK error is less than $0.1 mE_h$ across the entire potential energy curve. The approximate MRSQK scheme based on four Trotter steps is already comparable in accuracy to CCSD, while using $m = 8$ the error falls within chemical accuracy. By analyzing the error plot in the bottom half of Fig. 2.6, we see that there are small discontinuities in the curve due to the selection of a different set of reference states. This problem, however, is common to all selected CI methodologies, [178, 179, 180, 181, 182] as well as ADAPT-VQE. These discontinuities may be removed by employing references built from a fixed set of determinants.

2.4 Summary

In summary, the multireference selected quantum Krylov is a new quantum subspace diagonalization algorithm for solving the electronic Schrödinger equation on NISQ devices. MRSQK diagonalizes the Hamiltonian in a basis of many-body states generated by real-time evolution of a set of orthogonal reference states. This approach has two major advantages: (i) it requires no variational optimization of classical parameters, (ii) it avoids the linear dependency problem that may plague other QSD methods. Benchmark computations on H_6 , H_8 , and BeH_2 show that MRSQK with exact time-propagation converges rapidly to the exact energy using a number of Krylov states that is a small fraction of the full determinant space. When the real-time propagator is approximated via a Trotter decomposition, modest Trotter numbers $m = 4, 8$

are sufficient to ensure that truncation errors yield chemically accurate potential energy curves. We also report a comparison of the convergence of the energy of H_6 for MRSQK, selected configuration interaction (sCI), and the state-of-the-art ADAPT-VQE algorithm. In comparing sCI and MRSQK, the significantly faster convergence of the latter method indicates that the Krylov basis efficiently captures the important multideterminantal features of the wave function. The comparison with ADAPT-VQE shows that MRSQK can achieve a compact representation of the wave function competitive even with an adaptive strategy that aims to minimize the number of unitary rotations.

Together, these advantages make MRSQK a promising tool for treating strongly correlated electronic systems with quantum computation. However, there are several aspects of the MRSQK that deserve more consideration. The current reference selection strategy may produce different sets of references as the molecular geometry is changed, which in turn causes small discontinuities in potential energy curves. Selection procedures that, e.g., identify references from a small fixed set of orbitals could be used to address this issues. In this work, we have selected fixed values for the time steps t_n . Schemes in which the time steps are treated as variational parameters may be able to represent states with a fewer number of Krylov states and are worth exploring. Another important aspect is improving the approximation to the real-time dynamics. Our results indicate that low Trotter number approximations ($m = 1, 2$) commonly used in other context introduce errors that are too large. It would be desirable to explore the implementation of real-time dynamics via alternative methods, e.g. truncated Taylor series.[156] An interesting alternative is to follow the strategy of Ref. [183], which employs an unphysical dynamics

generated by a simple function of the Hamiltonian. This dynamics still spans the classical Krylov space and may be implemented with the same number of gates as a single Trotter number approximation.

2.5 Appendix

2.5.1 Trotterization errors and term ordering

The accuracy of MRSQK computations is primarily affected by errors resulting from the Trotter-Suzuki approximation of real-time dynamics. In this context, two key factors influencing the approximation error are the number of Trotter steps, denoted as m , and the ordering of Pauli term exponentials in the circuit. It is intriguing to investigate the extent to which the ordering of terms effectively ameliorates the Trotter error, particularly when a small number of Trotter steps is utilized. By selecting a potentially optimal term ordering, it becomes possible to achieve comparable accuracy with a smaller value of m .

Table 2.4: Ground-state energies (in E_h) of H_6 at a bond distance of 1.5 Å computed with MRSQK using different term orderings. MRSQK calculations use $N = d(s+1)$ Krylov basis states with three steps ($s = 3$) and $\Delta t = 0.5$ a.u. m indicates the Trotter number. Subscripts denote different ordering type of Pauli terms in the qubit Hamiltonian after the Trotterization. **OF**: OpenFermion’s default QubitOperator ordering; **JW**: terms are sorted in the descending order based on the magnitude of coefficients after *Jordan-Wigner* transform (Pauli term with largest magnitude goes first); **sq**: terms are sorted in the descending order based on the magnitudes of amplitudes of fermion operators in the *second quantized* form of the Hamiltonian (the group of terms from the fermion operator with the largest amplitude go first). **rand**: Pauli terms are shuffled *randomly* after Jordan-Wigner transform.

N	$E_{\text{OF}}^{(m=1)}$	$E_{\text{JW}}^{(m=1)}$	$E_{\text{sq}}^{(m=1)}$	$E_{\text{rand}}^{(m=1)}$	$E_{\text{OF}}^{(m=2)}$	$E_{\text{JW}}^{(m=2)}$	$E_{\text{sq}}^{(m=2)}$	$E_{\text{rand}}^{(m=2)}$
4	-2.982186	-2.988497	-2.988691	-2.982186	-2.998858	-3.001573	-3.002303	-2.998858
8	-3.001195	-3.010441	-3.010010	-3.001195	-3.010035	-3.014902	-3.015058	-3.010035
12	-3.008661	-3.010831	-3.010532	-3.008661	-3.013425	-3.015151	-3.015306	-3.013425
16	-3.010543	-3.011343	-3.011179	-3.010543	-3.014253	-3.015388	-3.015527	-3.014253
20	-3.011663	-3.016956	-3.017073	-3.011663	-3.015311	-3.018432	-3.018505	-3.015311
N	$E_{\text{OF}}^{(m=4)}$	$E_{\text{JW}}^{(m=4)}$	$E_{\text{sq}}^{(m=4)}$	$E_{\text{rand}}^{(m=4)}$	$E_{\text{OF}}^{(m=8)}$	$E_{\text{JW}}^{(m=8)}$	$E_{\text{sq}}^{(m=8)}$	$E_{\text{rand}}^{(m=8)}$
4	-3.009948	-3.009826	-3.010353	-3.009948	-3.014138	-3.013367	-3.013629	-3.014138
8	-3.015872	-3.017784	-3.017966	-3.015872	-3.018341	-3.018880	-3.018970	-3.018341
12	-3.016940	-3.017891	-3.018062	-3.016940	-3.018808	-3.018956	-3.019039	-3.018808
16	-3.017173	-3.017980	-3.018152	-3.017173	-3.018888	-3.019012	-3.019105	-3.018888
20	-3.017614	-3.019231	-3.019280	-3.017614	-3.019054	-3.019669	-3.019710	-3.019054
FCI	-3.020198							

Table 2.4 shows the ground-state energies from MRSQK computations with the Trotter number m of 1, 2, 4, 8, and four ordering strategies for linear H_6 at a bond length of 1.5 Å. We observe that chemical accuracy (error less than 1 kcal mol⁻¹ = 1.594 m E_h) can be reached fastest if **sq** ordering is used. For example, when $m = 4$, MRSQK using **sq** ordering gives an error of 0.917 m E_h with 20 Krylov basis states, while **JW** ordering gives 0.967 m E_h , and both the **OF** and **rand** ordering have a much larger error of 2.584 m E_h . To see the effect of ordering clearly, we compare the energy errors with respect to FCI for different orderings in several Trotter number m as a function of the number of Krylov basis states N , displayed in Fig. 2.7. It is clear to find two patterns of asymptotic convergences. For this specific H_6 geometry, **sq** and **JW** ordering always converge faster than **OF** and **rand** ordering. While there is a small difference between **sq** energies and **JW** energies, numbers of **OF** and **rand** are exactly the same to at least 6 decimals. Other random orderings are also tested (not shown), but all of them give the same results as **OF** and **rand** energies reported in Table 2.4.

Next, we examine how the effect of ordering might be change with different bond distances. Figure 2.8 and Figure 2.9 show the potential energy curves (PEC) of H_6 and BeH_2 , for RHF, MP2, CCSD, and the MRSQK utilizing 20 Krylov basis states ($s = 3$, $d = 5$). For MRSQK results, only **sq** and **rand** energies are plotted because they already well represent two asymptotic patterns. We can see that MRSQK with the lowest Trotter number m already outperforms RHF and MP2, ranging from the equilibrium geometry towards geometries displaying strong correlation. MRSQK with $m = 4$ and **sq** ordering achieves the same level of accuracy as CCSD at short bond distance range

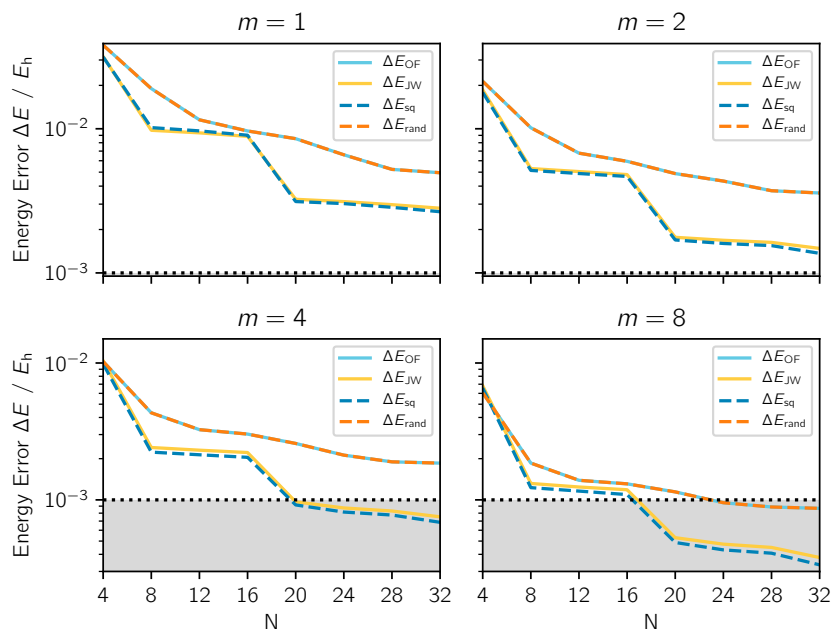


Figure 2.7: Energy error ΔE (in E_h) as a function of the number of Krylov basis states N of **linear** \mathbf{H}_6 at a bond distance of 1.5 \AA .

(0.6 \AA to 1.1 \AA), and when using $m = 8$ and **sq** ordering, MRSQK performs better than CCSD throughout the PEC (except the kink range of CCSD), especially when the geometry is far from the equilibrium with a bond length greater than 1.5 \AA . Note that MRSQK always gives a variational estimate of the energy, and produces accurate results for both strong and weak correlation range of the bond distance.

For the effect of term ordering on the energy error, we find that for \mathbf{H}_6 chain, the optimality of **sq** is consistent throughout the entire PEC (bond length from 0.6 \AA to 2.0 \AA), which can be seen that the **sq** curves are always below the **rand** curves for these small Trotter number $m = 1, 2, 4, 8$. By scrutinizing the error plot, we observe some small discontinuities in the **sq** curves but none in the **rand** curves, which results from the fact that the

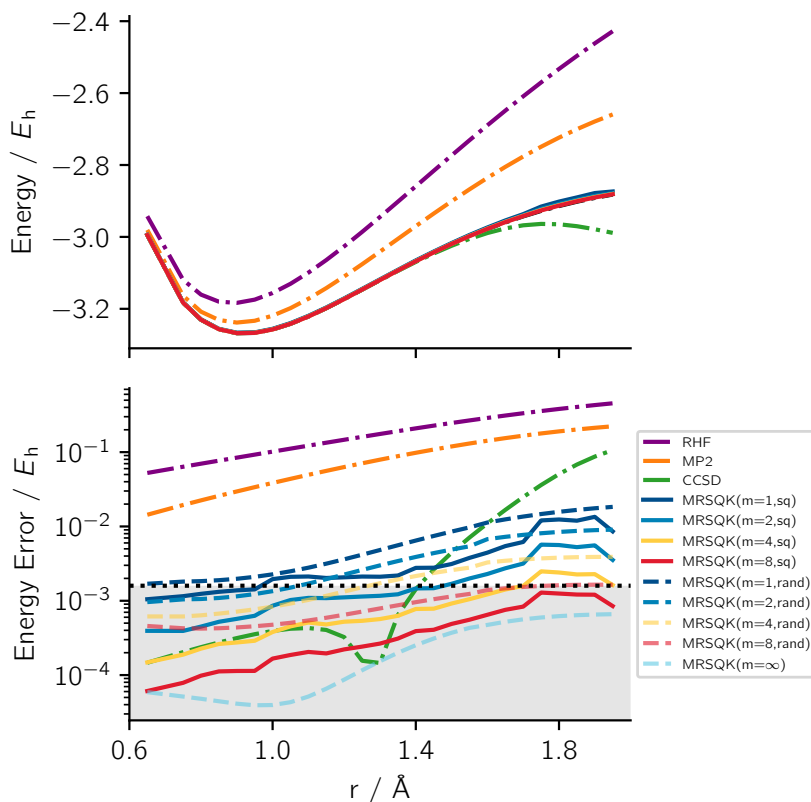


Figure 2.8: Potential energy curve (top) and energy error (bottom) for symmetric dissociation of **linear** \mathbf{H}_6 in STO-6G basis. References in MRSQK were selected using initial QK calculations with $s_0 = 4$ evolutions of the Hartree–Fock determinant and a time step of $\Delta t_0 = 0.25$ a.u. Then the following MRSQK calculations use $\Delta t = 0.5$ a.u., three time steps ($s = 3$), and five references ($d = 5$) corresponding to 20 Krylov basis states. Two orderings of Pauli terms are employed for comparison, with notations consistent with that in Table 2.4. The number of Trotter steps (m) is indicated in parentheses, while those from exact time evolution are labeled ($m = \infty$).

optimal Trotter ordering varies with the bond length.[184]

The ordering effect in the PEC of BeH_2 is much involved. In this case, the optimal ordering is not consistent when varying bond distances. Most of the case **rand** ordering performs better, in both the energy error and the discontinuity problem. The **sq** ordering also suffer from the problem of slow

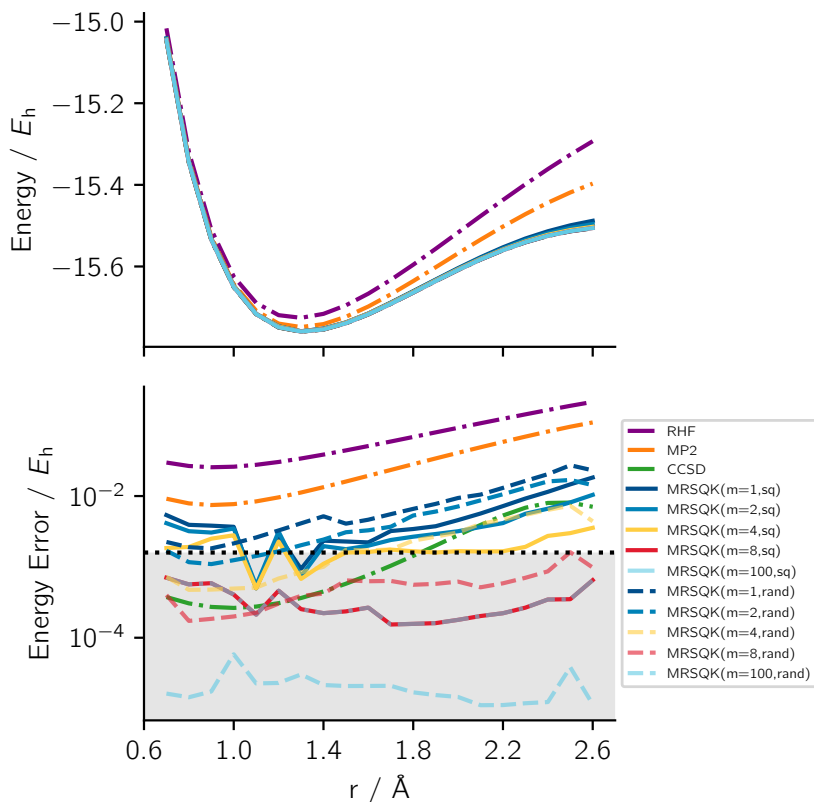


Figure 2.9: Potential energy curve (top) and energy error (bottom) for symmetric dissociation of **linear BeH_2** in STO-6G basis. References in MRSQK were selected using initial QK calculations with $s_0 = 3$ evolutions of the Hartree–Fock determinant and a time step of $\Delta t_0 = 0.25$ a.u. Then the following MRSQK calculations use $\Delta t = 2.0$ a.u., three time steps ($s = 4$), and five references ($d = 6$) corresponding to 30 Krylov basis states. Two orderings of Pauli terms are employed for comparison, with notations consistent with that in Table 2.4. The number of Trotter steps (m) is indicated in parentheses.

convergence of energy with respect to the Trotter number m . We run the PEC calculations using a very large m of 100, and surprisingly find that for **sq** ordering, the $m = 100$ plot overlaps with $m = 8$ plot entirely. This numerical observation is not well understood, thus requires a systematic study in the future.

2.5.2 Comments

Several questions remain for further interrogations.

I. **Term ordering strategy.** For H_6 case, **sq** ordering performs the best among the reported four strategies as well as many other random orderings. Nevertheless, we have no theoretical demonstration that it gives the fastest energy convergence among all possible $N!$ orderings that can be generated from N Pauli terms in the Hamiltonian. A possible route is to construct error operators for these orderings, as shown in Ref. [184].

II. **Measurement optimization.** In the reference selection part, we employ statistics of indirect measurements on the time-evolved states. While we only want a qualitatively correct probability distribution, running MRSQK calculations on realistic hardware with a high noise level might nonetheless necessitate a larger number of measurements than expected. It is worthwhile to try many recently proposed strategies to mitigate the measurement cost.[185, 186, 187, 188, 189, 190]

III. **Gate count reduction.** As discussed in section 2.1.4, some orderings of term exponentials in circuits will reduce the number of CNOT gates and H_k gates by the cancellation. We need to implement this term contraction in practice. Note that there might be a counterbalance between the number of gates that can be saved and errors from the term ordering for a specific level of Trotter steps and a Krylov subspace with a fixed size. But no available evidence wipes out the possibility that an optimal ordering exists that gives accurate energies as well as a significant reduction of gate counts.

2.6 Computing electronic excited states via multireference quantum Krylov method

This section summarizes some preliminary results for excited-state MRSQK calculations.

Computing excited states in the MRSQK framework is straightforward, since diagonalizing the Hamiltonian in the subspace also gives estimates of excited states with no additional cost. However, unlike in the ground state case, it is necessary to carefully choose the MRSQK reference space \mathcal{R} . This consideration comes from the fact that the multi-electron excited states with considerable multireference character usually have dominant contributions from double or higher excitations with respect to the Hartree–Fock determinant. Therefore, the quantum Krylov space generated via the Hamiltonian evolution of a trial ground-state wave function (e.g. the Hartree–Fock determinant) is biased toward the ground state and may not provide a good reference basis for describing excited states. An open problem is how to generalize the reference selection procedure to target excited states in a root-agnostic, black-box manner as the ground-state calculations.

Here, we test several approaches to generate reference spaces that aim to describe multiple electronic states.

2.6.1 State-specific approach

We first explore the use of a state-specific reference space informed by a small classical selected CI (sCI) calculation \mathcal{R}_{sCI} for targeting the low-lying excited

states [191, 192]. We also examine the use of the reference space generated by the ground state calculation \mathcal{R}_{GS} , to provide quantitative evidence for our intuitive argument stated above. Table 2.5 summarizes the two reference spaces employed in this study to calculate the first singlet excited state of linear H_6 . Note that the Hartree–Fock determinant is not included in the sCI reference space, since a small selected CI calculation of the first excited state suggests a negligible contribution of the Hartree–Fock determinant in the target excited-state manifold ($|C_{\text{HF}}^{(1)}|^2 = 0.025$), compared to the small but considerable weight in the ground-state FCI wave function ($|C_{\text{HF}}^{(0)}|^2 = 0.634$).

Table 2.6 reports the vertical excitation energies (in eV) for the first singlet excited state of linear H_6 at $r_{\text{HH}} = 1.5 \text{ \AA}$, and 0.9 \AA (near equilibrium geometry) computed with MRSQK method. We examine how energy estimations are impacted by the reference space type (\mathcal{R}_{GS} or \mathcal{R}_{sCI}), level of Trotter approximations (m), as well as the size of the Krylov subspace (N). Since the number of time steps ($s = 3$) and the time grid ($\Delta t = 0.5 \text{ a.u.}$) are fixed, the total number of Krylov basis states $N = 4, 8, 12, 16, 20$ corresponds to the size of reference space $\dim(\mathcal{R}) = 1, 2, 3, 4, 5$. The vertical excitation energy is calculated with respect to the corresponding ground-state energy obtained using the same values for N and the Trotter number m (same as those reported in Table 2.3).

For both geometries, best estimates of excitation energies using sCI reference space \mathcal{R}_{sCI} (with an absolute error of 0.035 eV for 1.5 \AA and 0.238 eV for 0.9 \AA) are more accurate than those from ground-state reference space \mathcal{R}_{GS} (with error of 0.336 eV for 1.5 \AA and 0.905 eV for 0.9 \AA). It is noteworthy that MRSQK calculations with sCI reference space \mathcal{R}_{sCI} obtain the best excitation

energy estimation with small Trotter number ($m = 1, 2$).

Figure 2.10 shows the potential energy curve of the first singlet excited state of H_6 computed with MRSQK method using two reference spaces, as well as results from CISD, EOM-CCSD, EOM-CC3 method for comparison.

In Figure 2.11, we report the deviations in vertical excitation energies of 2^1A_g state (with respect to FCI results) along the dissociation curve. We also show mean absolute errors and nonparallelism errors in Table 2.7.

Table 2.5: Two reference spaces used in MRSQK method for computing the first singlet excited state (2^1A_g) of linear H_6 . The orbitals are ordered by the irreducible representation of the D_{2h} point group as $1a_g, 2a_g, 3a_g, 1b_{1u}, 2b_{1u}, 3b_{1u}$. The ordering of orbital energies (in ascending order) from the restricted Hartree–Fock calculation is given by $1a_g < 1b_{1u} < 2a_g < 2b_{1u} < 3a_g < 3b_{1u}$, so the Hartree–Fock determinant is $|220200\rangle$.

Reference	Ground-state reference space \mathcal{R}_{GS}	sCI reference space \mathcal{R}_{sCI}
$ \Phi_0\rangle$	$ 220200\rangle$	$ 200220\rangle$
$ \Phi_1\rangle$	$ 200220\rangle$	$ 220020\rangle$
	$-0.5771(2 \uparrow \downarrow \uparrow 0\rangle + 2 \downarrow \uparrow \downarrow 0\rangle)$	
$ \Phi_2\rangle$	$+0.3042(2 \uparrow \uparrow \downarrow 0\rangle + 2 \downarrow \downarrow \uparrow 0\rangle)$ $+0.2729(2 \uparrow \downarrow \uparrow 0\rangle + 2 \downarrow \uparrow \downarrow 0\rangle)$	$0.7071(220 \uparrow \downarrow 0\rangle + 220 \downarrow \uparrow 0\rangle)$
$ \Phi_3\rangle$	$ 222000\rangle$	$ 202200\rangle$
	$-0.5699(\uparrow \downarrow 02 \downarrow \uparrow\rangle + \downarrow \uparrow 02 \uparrow \downarrow\rangle)$	
$ \Phi_4\rangle$	$+0.3651(\uparrow \downarrow 02 \uparrow \downarrow\rangle + \downarrow \uparrow 02 \downarrow \uparrow\rangle)$ $+0.2047(\uparrow \uparrow 02 \downarrow \downarrow\rangle + \downarrow \downarrow 02 \uparrow \uparrow\rangle)$	$0.7071(2 \uparrow \downarrow 200\rangle + 2 \downarrow \uparrow 200\rangle)$

2.6.2 State-averaged approach with dynamic weights

The state-specific treatments in Sec. 2.6.1 would be deficient in describing excited states involved in avoided crossings and conical intersections, which

Table 2.6: Vertical excitation energies ΔE (in eV) for the first singlet excited state (2^1A_g) of linear H_6 at two bond distance 1.5 Å and 0.9 Å computed with MRSQK method in a STO-6G basis. MRSQK calculations use $N = d(s + 1)$ Krylov basis states using $\Delta t = 0.5$ a.u. and three steps ($s = 3$). The vertical excitation energy is calculated with respect to the corresponding ground-state energy obtained using the same values for N and m (as reported in Table 2.3). Note that we take the Trotter approximation with $m = 100$ as a good approximation to the infinite m limit. The data in parentheses show deviations from the FCI result ($\epsilon = \Delta E_{\text{MRSQK}} - \Delta E_{\text{FCI}}$, unit in eV). The best estimate of each reference space is indicated in bold type.

ΔE_{MRSQK}	N				
	4	8	12	16	20
$r_{\text{HH}} = 1.5 \text{ \AA}$					
Ground-state reference space					
$m = 1$	20.585(17.040)	7.265(3.720)	6.507(2.962)	6.285(2.74)	6.274(2.729)
$m = 2$	18.644(15.099)	5.492(1.947)	5.026(1.481)	4.893(1.348)	4.809(1.264)
$m = 4$	17.475(13.930)	4.593(1.048)	4.304(0.759)	4.209(0.664)	4.134(0.589)
$m = 8$	16.828(13.283)	4.271(0.726)	4.066(0.521)	4.007(0.462)	3.944(0.399)
$m = \infty$	16.254(12.709)	4.101(0.556)	3.964(0.419)	3.934(0.389)	3.881(0.336)
sCI reference space					
$m = 1$	4.864(1.319)	5.060(1.515)	5.161(1.616)	5.089(1.544)	3.902(0.357)
$m = 2$	3.369(-0.176)	3.627(0.082)	3.715(0.170)	3.624(0.079)	3.510(-0.035)
$m = 4$	2.656(-0.889)	2.735(-0.810)	2.768(-0.777)	2.548(-0.997)	2.564(-0.981)
$m = 8$	2.410(-1.135)	2.360(-1.185)	2.375(-1.170)	2.132(-1.413)	2.137(-1.408)
$m = \infty$	2.256(-1.289)	2.113(-1.432)	2.124(-1.421)	1.899(-1.646)	1.904(-1.641)
FCI	3.545				
$r_{\text{HH}} = 0.9 \text{ \AA}$					
Ground-state reference space					
$m = 1$	47.783(34.855)	17.156(4.228)	17.013(4.084)	16.678(3.749)	16.648(3.720)
$m = 2$	37.473(24.544)	16.054(3.125)	15.999(3.070)	15.671(2.742)	15.637(2.709)
$m = 4$	31.539(18.610)	15.205(2.277)	15.021(2.092)	14.496(1.567)	14.453(1.524)
$m = 8$	29.163(16.234)	14.900(1.971)	14.614(1.685)	14.073(1.144)	14.004(1.076)
$m = 100$	27.607(14.678)	14.754(1.825)	14.404(1.475)	13.919(0.991)	13.834(0.905)
sCI reference space					
$m = 1$	15.744(2.815)	15.879(2.950)	13.166(0.238)	13.184(0.256)	12.092(-0.837)
$m = 2$	13.547(0.618)	13.545(0.616)	12.627(-0.302)	12.626(-0.303)	11.900(-1.028)
$m = 4$	11.700(-1.229)	10.964(-1.965)	10.949(-1.980)	10.092(-2.837)	10.070(-2.859)
$m = 8$	10.907(-2.022)	9.873(-3.056)	9.866(-3.063)	8.977(-3.951)	8.968(-3.960)
$m = \infty$	10.403(-2.526)	9.287(-3.641)	9.289(-3.640)	8.429(-4.500)	8.429(-4.500)
FCI	12.929				

hold significant importance in nonradiative processes [193, 194, 195]. In such scenarios, multiple electronic states with distinct characters become de-

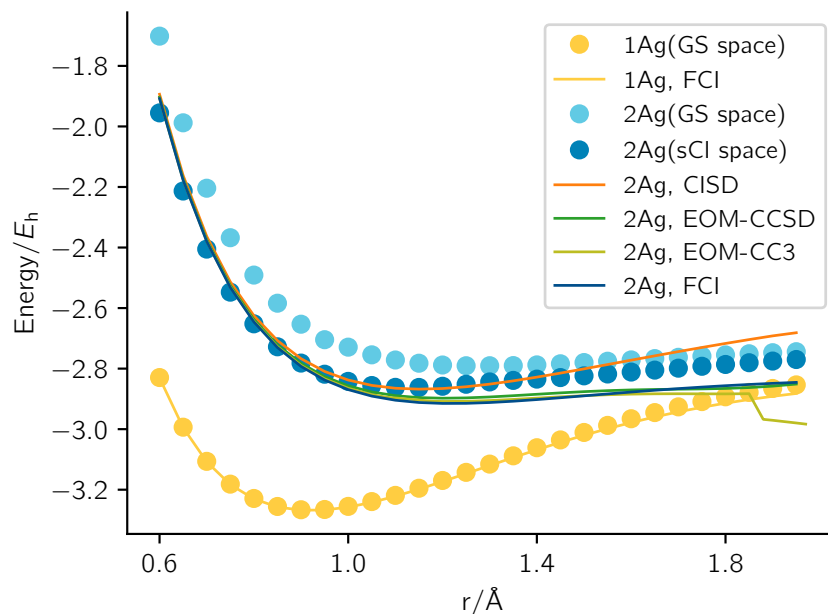


Figure 2.10: Potential energy curves (in E_h) of the ground state (1^1A_g) and the first singlet excited state (2^1A_g) for the symmetric dissociation of H_6 computed with the MRSQK method using two reference spaces. All calculations use a STO-6G basis. MRSQK computations use one Trotter step ($m = 1$), $\Delta t = 0.5$ a.u., three time steps ($s = 3$), and five references ($d = 4$) corresponding to 16 Krylov basis states.

Table 2.7: Statistical evaluation for deviations of vertical excitation energies (in eV) along the dissociation of H_6 as shown in Figure 2.11. The mean absolute error (MAE, in eV) is estimated as an arithmetic average of the absolute errors over 28 geometries. The nonparallelism error (NPE, in eV) is defined as the difference between the largest and smallest excitation energy deviation from the FCI vertical excitation energy along the symmetric dissociation curve.

Method	MAE	NPE
MRSQK(GS space)	3.274	3.583
MRSQK(sCI space)	1.145	3.057
CISD	0.934	0.948
EOM-CCSD	0.612	2.634
EOM-CC3	0.276	1.691
TDDFT	1.849	1.473

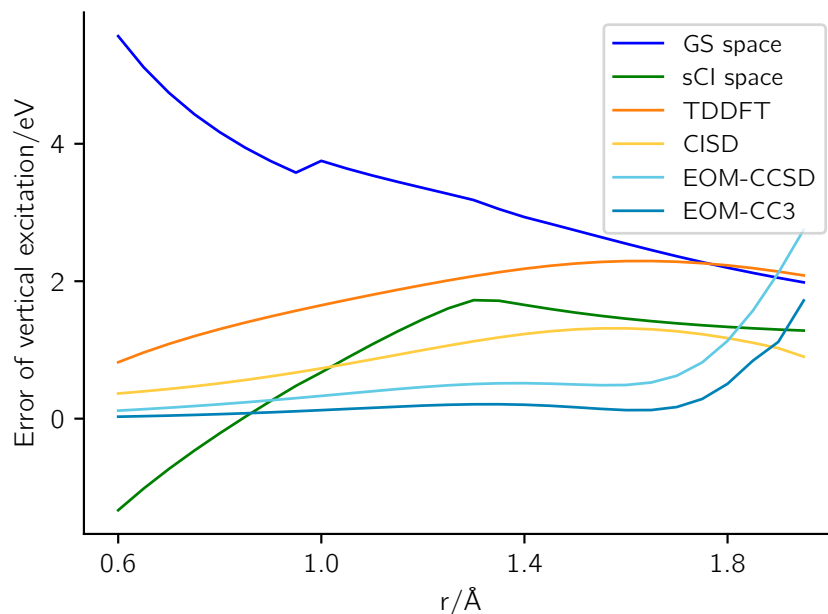


Figure 2.11: Deviations of vertical excitation energies (in eV) from FCI results of the first singlet excited state (2^1A_g) along the symmetric dissociation of H_6 computed with the MRSQK method using two reference spaces. All calculations use a STO-6G basis. MRSQK computations use one Trotter step ($m = 1$), $\Delta t = 0.5$ a.u., three time steps ($s = 3$), and five references ($d = 4$) corresponding to 16 Krylov basis states.

generate or nearly degenerate, posing challenges for describing them accurately using single-reference excited-state electronic structure methods[196] such as time-dependent density functional theory (TD-DFT)[197, 198] and the equation-of-motion coupled cluster hierarchy[199, 200], or state-specific multireference approaches [201]. This becomes particularly challenging when the states involved include the ground and first excited states.

Here we explore a state-averaged approach[191, 202] in which a single reference space is formed with dynamically-weighted references from multiple state-specific reference spaces that correspond to all roots of interest. We assume states in state-specific reference spaces are in descending order of

importance with respect to the target root. The k -th reference state in the state-averaged reference space \mathcal{R}_{SA} is given by

$$|\Phi_k^{\text{SA}}\rangle = \sum_r a_r |\Phi_k^r\rangle \quad (2.15)$$

where $|\Phi_k^r\rangle$ is the k -th reference state in the state-specific reference space \mathcal{R}_r , and the normalization condition $\sum_r a_r = 1$ is enforced. The dynamic weights $\{a_r\}$ provide more flexibility when we want to describe a large area of the potential energy surface on an equal footing.

Chapter 3

Leveraging small scale quantum computers with unitarily downfolded Hamiltonians

Most of this chapter is reprinted/adapted with permission from Renke Huang, Chenyang Li, and Francesco A. Evangelista. *PRX Quantum*, 4(2):020313, 2023, DOI:[10.1103/PRXQuantum.4.020313](https://doi.org/10.1103/PRXQuantum.4.020313). Copyright held by authors.

Molecules and materials that display strong electron correlation are hard to simulate with classical computers due to the exponential growth of the many-body Hilbert space [4]. Quantum computers [1, 3] are particularly well suited to simulate many-body systems, as they can efficiently represent and perform operations on many-particle wave functions. These features make them a promising solution to the electron correlation problem [85, 86], which, in its most general form, still defies classical algorithms. However, the accurate modeling of realistic many-electron systems requires the use of large

computational bases and, therefore, it is unlikely to be accessible to small-scale quantum computers with up to only a few hundred qubits. One of the most promising strategies to maximize the impact of near-term quantum devices is to pair a quantum algorithm with classical approaches that perform a reduction of the number of qubits required in a quantum computation [203].

Several strategies have been proposed to minimize quantum resources by combining quantum computations with traditional quantum chemistry approaches. Takeshita *et al.* [137] have applied quantum algorithms in combination with the active-space approximation and orbital optimization. This idea has been demonstrated experimentally for model molecules with up to ten orbitals using just two qubits [204]. Boyn *et al.* [205] have obtained active-space 2-RDMs from quantum computations and postprocessed them with two classical correlation methods, the anti-Hermitian contracted Schrödinger equation (ACSE) theory [206, 207, 208] and multiconfigurational pair density functional theory (MC-PDFT) [209]. Fujii *et al.* have combined the divide-and-conquer technique with quantum computations to solve the ground state of a 64-qubit two-dimensional Heisenberg model with 20-qubit simulations, [210] and have later extended it to obtain excited states of periodic hydrogen chain [211]. Malone *et al.* have devised an efficient active-space formulation of first-order symmetry-adapted perturbation theory (SAPT) that has produced accurate interaction energies between large molecular systems using low-depth wave functions from quantum computers [212] and, later, Loipersberger *et al.* have extended it to obtain second-order interaction energies [213]. Ma *et al.* have proposed a multiscale quantum computing framework based on the many-body expansion fragmentation

approach [214]. Tammaro *et al.* [215] have investigated the use of N -electron valence perturbation theory (NEVPT) [216, 217] in combination with the variational quantum eigensolver (VQE) [57, 58, 59] and quantum subspace expansion [91, 113] algorithms. Ryabinkin *et al.* [218] have used low-order perturbative corrections to reduce the quantum resources required in their iterative qubit coupled-cluster VQE approach. Huggins *et al.* have recently proposed a hybrid algorithm that combines quantum shadow tomography with the auxiliary-field quantum Monte Carlo method, achieving the largest-to-date chemical simulation on hardware of a 16-qubit chemical system [219].

Other works have focused on reducing the number of qubits and gates required by variational quantum algorithms using embedding techniques. For example, density-matrix embedding theory [220, 221] has been applied to simulate a H_{10} ring on an ion-trap quantum computer by decomposing this 20-qubit system into ten two-qubit problems [222]. Huang *et al.* have used quantum defect embedding theory to simulate spin defects on quantum computers [223]. Tazhigulov *et al.* have used simplified low-energy spin models and various error-mitigation protocols to simulate iron-sulfur clusters and spin-liquid materials [224]. Combining explicitly correlated methods with quantum algorithms is another strategy explored in several works [225, 226, 227, 228, 229] to achieve higher accuracy without increasing quantum resources. Motta *et al.* [225] have used a canonical transcorrelated F12 (CT-F12) Hamiltonian [230] in conjunction with the variational quantum eigensolver method, whereas McArdle *et al.* [226] have used Boys and Handy's transcorrelated approach, which produces a non-Hermitian Hamiltonian containing up to three-body

terms. A recent contribution also considers an *a posteriori* perturbative correction based on the explicitly correlated $[2]_{\text{R12}}$ approach [227].

Quantum chemical effective Hamiltonian theories [231, 232, 233, 234, 235, 236, 237] offer another way to downfold correlation effects into a small active-space quantum computation. In such approaches, one partitions the orbital space into two sets, active and inactive, and a transformation is applied to the Hamiltonian to eliminate terms that couple these two spaces. The resulting Hamiltonian then accounts for electron correlation effects in the inactive orbitals via effective many-body interactions. In principle, it is straightforward to adapt this strategy to a quantum-classical hybrid setting whereby a highly entangled quantum state involving only the active orbitals is solved for on a quantum computer and the remaining weak correlation effects are recovered with a polynomially scaling classical algorithm. However, there are several major potential issues when combining effective Hamiltonian methods and quantum algorithms. A particularly severe limitation of some approaches is the need to measure three- and four-body reduced density matrices (RDMs), introducing a prohibitively large prefactor in quantum computations that scales as the sixth to the eighth power of the number of active orbitals. A second important issue is the impact of noise in the measured RDMs on the energy (and other properties) and the numerical stability of methods that require the solution of nonlinear equations. Lastly, it is often necessary to go beyond low-order perturbative treatments to achieve accurate energetics. Several quantum downfolding methods have been proposed. The double unitary coupled-cluster (DUCC) approach [238, 239, 240] is a downfolding procedure based on a mean-field reference state. Le and Tran [241]

have employed their one-body second-order Møller-Plesset perturbation theory (OBMP2) to create an effective Hamiltonian with modified one-body interactions for the VQE method.

In this chapter, we present a quantum downfolding approach based on the driven similarity renormalization group (DSRG) [242, 243, 244, 245] that addresses the challenges highlighted above, including reducing the cost of measuring RDMs on quantum devices. The DSRG is an integral reformulation of numerical flow-renormalization group methods [246, 247, 248, 249]. Our quantum formulation of the DSRG (QDSRG) is compatible with any quantum algorithm capable of producing low-rank RDMs [57, 91, 134, 140, 250] (up to partial or full second-order) and augments it with an accurate, intruder-free, and nonperturbative treatment of weak (dynamical) correlation. We benchmark the performance of the QDSRG scheme in computing the dissociation curve of the nitrogen molecule and the adiabatic singlet-triplet splittings of the *para*-benzyne diradical. In addition to exact simulations, we demonstrate the usefulness of this strategy in the presence of realistic noise by combining the QDSRG with VQE experiments on IBM quantum computers. We compute the dissociation curve of the H₂ molecule with a nearly-complete quintuple- ζ basis and model the bicyclobutane isomerization pathways to *trans*-butadiene. This isomerization reaction proceeds via two transition states whose relative energies are impacted by significant orbital rearrangements and different correlation effects in the electronic states. Resolving the energetics of all reaction intermediates across the full pathway with sufficient accuracy is notoriously challenging for many quantum chemistry methods, including advanced coupled cluster methods [251]. The methodological advances introduced in this

work are complementary to others developed recently to model reactions of ever-increasing complexity on quantum hardware, including the hydrogen-transfer reaction studied at the Hartree–Fock level [252], the recent work of Motta *et al.* [253] on the simulation of ground- and excited-state properties of the sulfonium cation using VQE and quantum subspace expansion [91], and a study by O’Brien *et al.* of the ring-opening reaction in cyclobutadiene using VQE and a Hamiltonian projected on the seniority zero subspace [254]. Our work demonstrates that classical downfolding provides a path to modeling complex chemistry reactivity on near-term quantum devices, accounting for both electron correlation and basis set effects to approach relative energies within 1 kcal mol⁻¹ from experimental energies.

3.1 Methods

3.1.1 Unitary Hamiltonian downfolding via the DSRG

The DSRG method [242, 243, 244, 245, 255] starts from a reference correlated state Ψ_0 and performs a unitary transformation of the Hamiltonian, H , that brings it to a block-diagonal form

$$H \mapsto \bar{H} = e^{-A} H e^A, \quad (3.1)$$

where the operator A is anti-Hermitian. The goal of this transformation is to remove the second-quantized components of \bar{H} that couple Ψ_0 to excited configurations, which we refer to as the nondiagonal components of \bar{H} (denoted as \bar{H}^N).

One of the challenges associated with eliminating these couplings (i.e., solving for $\bar{H}^N = 0$) is the emergence of numerical instabilities, which are related to excitations with small energy denominators. To avoid this issue, the DSRG achieves only a partial block-diagonalization of H by solving a set of regularized equations

$$\bar{H}^N = R(s). \quad (3.2)$$

In this equation, $R(s)$ is an operator that depends on the flow parameter $s \in [0, \infty)$, and its purpose is to suppress excited configurations associated with an energy denominator smaller than the energy cutoff $\Lambda = 1/\sqrt{s}$. Hence, solving Eq. (3.2) imparts a dependence on s onto the A operator and the transformed Hamiltonian.

The DSRG operator $A(s)$ is expressed in terms of a s -dependent coupled cluster particle-hole excitation operator [256, 257, 258, 259] as $A = T - T^\dagger$ with $T = T_1 + T_2 + \dots$ where each k -body component is

$$T_k = \frac{1}{(k!)^2} \sum_{ij\dots}^{\text{hole}} \sum_{ab\dots}^{\text{particle}} t_{ab\dots}^{ij\dots}(s) \{\hat{a}_{ij\dots}^{ab\dots}\}, \quad (3.3)$$

where we write the normal-ordered creation and annihilation operators in a compact form $\{\hat{a}_{ij\dots}^{ab\dots}\} = \{\hat{a}^a \hat{a}^b \dots \hat{a}_j \hat{a}_i\}$ [260, 261], and the cluster amplitudes ($t_{ab\dots}^{ij\dots}$) are tensors antisymmetric with respect to the individual permutation of upper and lower indices. The hole space contains the occupied and partially occupied spin orbitals (labeled with the indices i, j, \dots), while the particle space contains the partially occupied and unoccupied spin orbitals (labeled with the indices a, b, \dots) of the reference Ψ_0 . One of the simplest nonpertur-

bative truncation schemes is the linearized DSRG (LDSRG) with one- and two-body operators [LDSRG(2)] [244] where: 1) T is truncated as $T \approx T_1 + T_2$, and 2) every commutator in the Baker–Campbell–Hausdorff expansion of \bar{H} contains only one- and two-body operators (indicated with subscript “1,2”) using a linear recursive commutator approximation [262, 232].

$$\bar{H} \approx \bar{H}_{1,2} = H + \sum_{k=1}^{\infty} \frac{1}{k!} \underbrace{[\cdots [[H, A]_{1,2}, A]_{1,2}, \cdots]_{1,2}}_{k \text{ nested commutators}}. \quad (3.4)$$

The resulting approximate DSRG transformed Hamiltonian ($\bar{H}_{1,2}$) contains a scalar term plus one- and two-body interactions, as the original Hamiltonian. We note that it is possible to go beyond this truncation scheme and include higher-order contributions in \bar{H} [263, 264]; however, this comes at the cost of increasing the number of unique terms and the computational scaling.

Once Eq. (3.2) is solved, the energy may be computed as the expectation value of $\bar{H}_{1,2}$

$$E = \langle \Psi_0 | \bar{H}_{1,2} | \Psi_0 \rangle. \quad (3.5)$$

Alternatively, one may solve the eigenvalue problem

$$\bar{H}_{1,2} |\tilde{\Psi}_0\rangle = \tilde{E} |\tilde{\Psi}_0\rangle, \quad (3.6)$$

and obtain a *relaxed* reference state $\tilde{\Psi}_0$ and its corresponding energy \tilde{E} . It is often the case that multireference quantum chemistry methods, like CASPT2 [265] or NEVPT2 [216, 217], only evaluate the energy as an expectation value via equations analogous to Eq. (3.5). In this case, one talks of a “diagonalize-then-perturb” approach and the resulting formalism only provides an energy

correction rather than a properly downfolded Hamiltonian. We note that, when performed exactly, the unitary transformation at the basis of the DSRG [Eq. (3.1)] would lead to a method similar to the ACSE [206, 207, 208]. In the case of a reference composed of a single Slater determinant, the DSRG becomes equivalent to a regularized form of unitary coupled cluster theory [266].

Solving the DSRG equations [Eq. (3.2)] requires the reduced density cumulants (RDCs) of the reference state (which we also refer to as “cumulants”) [267, 268]. A generic k -body reduced density cumulant (λ_k) is the connected part of the corresponding k -body RDM (γ_k), defined as

$$\gamma_{uv\dots}^{xy\dots} = \langle \Psi_0 | a_x^\dagger a_y^\dagger \cdots a_v a_u | \Psi_0 \rangle \dots \quad (3.7)$$

where the product $a_x^\dagger a_y^\dagger \cdots a_v a_u$ contains k creation and k annihilation operators. Throughout the paper, we use the indices u, v, w, x, y, z to label active spin orbitals partially occupied in Ψ_0 . The RDCs of the reference state encode all the information required to include correlation effects outside of the active orbitals. Therefore, any computational method capable of generating Ψ_0 and its RDMs can be interfaced with the DSRG downfolding procedure. It is convenient to express the DSRG equations in terms of cumulants, as any truncated scheme preserves the size extensivity of the energy. Reduced density cumulants enter the LDSRG(2) equations in the following way. Evaluation of the operator A requires λ_1 and λ_2 , while evaluation of the energy additionally requires λ_3 , which is challenging to measure on near-term devices. In the next section, we analyze a modified DSRG approach for a hybrid quantum-classical

scheme.

3.1.2 Hybrid quantum-classical DSRG downfolding

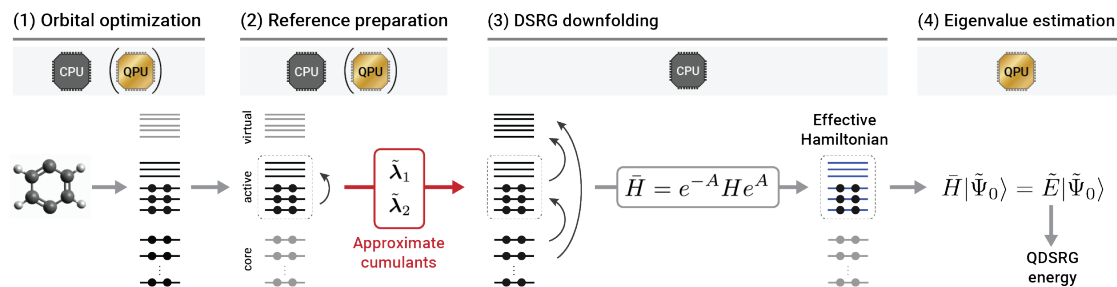


Figure 3.1: The QDSRG scheme for performing hybrid classical-quantum computations on strongly correlated molecules. The computation begins with a classical or hybrid orbital optimization (1), followed by the preparation of a correlated reference state defined in the subset of active molecular orbitals (2). This step yields the reduced density cumulants ($\tilde{\lambda}_k$), which are passed to a classical DSRG algorithm (3) to produce the effective Hamiltonian ($\tilde{H}_{1,2}$) and its expectation value with respect to the approximate cumulants ($\langle \tilde{H}_{1,2} \rangle_{\tilde{\lambda}_k}$). (4) In the last step, an eigenvalue of the DSRG effective Hamiltonian is found via a quantum algorithm.

An outline of how the DSRG downfolding scheme may be adapted to a hybrid quantum-classical scheme is illustrated in Figure 3.1. We can break down the procedure into four steps:

1. *Orbital optimization.* The first step is an optimization of the molecular orbitals for a target electronic state. To ensure that this scheme is applicable to large active spaces, it is important that the cost of the orbital optimization scales as a low-order polynomial of the size of the system. This step could employ a mean-field approximation (e.g., Hartree–Fock) or optimize the orbitals of a correlated state, as in the complete-active-

space self-consistent-field (CASSCF) method. In the latter case, a quantum computation may be used to optimize the correlated state.

2. *Reference preparation.* In the second step, we propose to employ an approximate reference state that might be obtained from a classical or quantum computation. In this step, the spin orbital basis is partitioned into three subsets: core (doubly occupied), active (partially occupied), and virtual (empty). The quantum computation involves only the active orbitals and uses a modified one-electron operator that accounts for the interaction with the occupied core orbitals. With these restrictions, the quantum computation requires at most $2 N_A$ qubits, where N_A is the number of active orbitals. As part of the quantum computation, the low-rank reduced density cumulants ($\tilde{\lambda}_k$) of the reference state are evaluated. This step requires only a coarsely optimized reference state, and therefore, it does not introduce a significant overhead in our hybrid quantum-classical scheme.
3. *DSRG downfolding.* The third step consists of a classical DSRG computation using the approximate reduced density cumulants ($\tilde{\lambda}_k$) from step 2. This step produces the anti-Hermitian operator A and the DSRG transformed Hamiltonian. We also obtain the expectation value of $\bar{H}_{1,2}$ with respect to the approximate RDCs, ($\langle \bar{H}_{1,2} \rangle_{\tilde{\lambda}_k}$); however, this quantity is generally a poor approximation to the exact energy. This step has polynomial scaling in the number of active and total orbitals.
4. *Eigenvalue estimation.* In the last step of this procedure, the approximate DSRG downfolded Hamiltonian is used in a quantum computation

that estimates one of its eigenvalues (\tilde{E}). Depending on the quantum resources available, this step may be performed with a hybrid quantum-classical algorithm like VQE, in which case one may obtain an exact or approximate eigenvalue of $\tilde{H}_{1,2}$, or use a pure quantum algorithm like phase estimation [85, 86] to target an exact eigenvalue.

For generality, we separate steps 1 and 2 of the QDSRG scheme; however, if the orbital optimization step minimizes the energy of a correlated state generated via a quantum computation (e.g., like in CASSCF), then these steps can be combined into a single one.

The most crucial differences between the conventional DSRG formulation and the QDSRG scheme are the density cumulant approximation in the DSRG downfolding procedure and the eigenvalue estimation (step 4). Here we consider approximations of the cumulants that are consistent with the measurement of, at most, a quadratic-scaling number of elements. The simplest approximation (1-QDSRG) retains only the diagonal elements of the one-body density cumulant, that is,

$$\tilde{\lambda}_v^u = \begin{cases} \lambda_u^u, & \text{if } u = v, \\ 0, & \text{otherwise.} \end{cases} \quad (3.8)$$

Since $\lambda_1 = \gamma_1$, this scheme requires only the diagonal parts of the one-body density matrix $\gamma_u^u = \langle \Psi_0 | a_u^\dagger a_u | \Psi_0 \rangle$. As the number operators $n_u = a_u^\dagger a_u$ commute with each other, the diagonal elements of arbitrary rank RDMs can be measured simultaneously. Therefore, if Ψ_0 is generated via a quantum computation, this would require performing only two experiments to measure the

energy ($\langle H \rangle$) and the diagonal elements of γ_1 .

The next approximation (2-QDSRG) requires access to a quadratic number of elements of the RDCs, and consists in taking the full one-body density matrix ($\tilde{\lambda}_1 = \lambda_1$) plus the diagonal components of the two-body reduced density cumulant

$$\tilde{\lambda}_{xy}^{uv} = \begin{cases} \lambda_{uv}^{uv}, & \text{if } u = x \text{ and } v = y, \\ \lambda_{vu}^{uv} = -\lambda_{uv}^{uv}, & \text{if } u = y \text{ and } v = x, \\ 0, & \text{otherwise.} \end{cases} \quad (3.9)$$

where the two-body RDC is computed from one- and two-body RDMs

$$\lambda_{xy}^{uv} = \gamma_{xy}^{uv} - \gamma_x^u \gamma_y^v + \gamma_y^u \gamma_x^v. \quad (3.10)$$

These cumulant approximations may be justified using a perturbative argument. At first order in perturbation theory (assuming a one-body diagonal zeroth-order operator, $H_0 = \sum_p \epsilon_p \{a_p^\dagger a_p\}$), one may show that the amplitudes corresponding to single and double excitations are given by [243]

$$t_a^{i,(1)} = [f_a^i + \sum_{ux}^A \Delta_{ux}^x t_{ax}^{iu,(1)} \gamma_u^x] \frac{1 - e^{-s(\Delta_a^i)^2}}{\Delta_a^i}, \quad (3.11)$$

$$t_{ab}^{ij,(1)} = \langle ab || ij \rangle \frac{1 - e^{-s(\Delta_{ab}^{ij})^2}}{\Delta_{ab}^{ij}}, \quad (3.12)$$

where the quantities f_a^i and $\langle ab || ij \rangle$ are elements of an effective one-body operator and antisymmetrized two-electron integrals, respectively, while the denominators are defined as $\Delta_a^i = \epsilon_i - \epsilon_a$ and $\Delta_{ab}^{ij} = \epsilon_i + \epsilon_j - \epsilon_a - \epsilon_b$, with $\epsilon_i = f_i^i$ [243]. These equations show that at first order, the double exci-

tation component of A is independent of the reference cumulants, and the single excitation component of A depends only on the off-diagonal elements of the active-active block of γ_1 [since when $x = u$ in Eq. (3.11) we have that $\gamma_u^u \Delta_u^u = \gamma_u^u (\epsilon_u - \epsilon_u) = 0$]. Therefore, the 2-QDSRG approximation is already consistent with a first-order approximation to the DSRG operator A , while 1-QDSRG neglects the off-diagonal terms of γ_u^x that enter into Eq. (3.11). The three-body cumulant λ_3 is neglected in both the 1-QDSRG and 2-QDSRG, and it may be shown to enter the energy at second-order in perturbation theory. The impact of neglecting λ_3 in the DSRG was analyzed in previous studies [243, 269, 270].

It is noteworthy that the QDSRG scheme significantly reduces the cost of state preparation and measurement. As shown by Zhao *et al.* [271], the number of repeated state preparations required to estimate the k -body RDM of a n -fermion system with precision ϵ can be reduced to $\binom{n}{k} k^{3/2} \log(n) / \epsilon^2$ via partial tomography. As other active space methods, the QDSRG scheme reduces n from the full basis to a limited number of active spin orbitals. More importantly, a significant cost reduction is achieved compared to other active space methods that require up to the 4-RDM ($k = 4$) [215] and the LDSRG(2) method, which requires up to the 3-RDM ($k = 3$). In the linearized 1-QDSRG with one- and two-body operators [1-QLDSRG(2)], the diagonal elements of 1-RDM can be measured with a cost independent of n , while the 2-QLDSRG(2) corresponds to the case $k = 1$ with the small additional cost of measuring the diagonal elements of the 2-RDM (independent of n), which needs $(n \log(n) + 1) / \epsilon^2$ state preparations and measurements for a desired precision ϵ .

Note that the computational cost of the DSRG classical downfolding proce-

dure (step 3) is also reduced by the cumulant approximation introduced in the QDSRG scheme. Specifically, the N_A^6 -scaling terms are eliminated completely in QLDSRG(2), compared to the original LDSRG(2) formalism. However, we should point out that this cost reduction is limited, since the overall scaling of the QLDSRG(2) transformation is still dominated by a term that scales as $\mathcal{O}(N_V^4 N_C^2)$, where N_V is the number of unoccupied orbitals and N_C the number of doubly occupied orbitals.

To enable the pipeline of QDSRG computations, we implement functionalities that export integrals and read/write the reference density matrices from external files in `Forte` [272], an open-source plugin for the *ab initio* quantum chemistry package `Psi4` [273]. We obtain the QDSRG effective Hamiltonian from `Forte` using a spin-free implementation [255].

Table 3.1: The energy error for the H₂ molecule (in mE_h) computed with the LDSRG(2) and QLDSRG(2) methods. All computations use a cc-pVTZ basis [274] and the flow parameter value $s = 0.5 E_h^{-2}$. The energy errors are computed with respect to full configuration interaction (FCI) energies (in E_h) reported in the last row of the table. For the LDSRG(2), the expectation value of the energy is designated with “ $\langle \bar{H}_{1,2} \rangle$,” while the lowest eigenvalue is indicated with “eig. $\bar{H}_{1,2}$.” For the QDSRG methods, we report two sets of data. Those labeled “ $\gamma_3 = 0$ ” use an approximate three-body cumulant reconstructed from λ_1 and λ_2 . The results for line M employ CCSD natural orbitals and the one-body relaxed CCSD reduced density matrix as input to the QDSRG procedure.

Case	Method	Orbital Type	Active orbitals	r_{HH} (Å)				
				0.75	1.50	2.25	3.00	
A	LDSRG(2) ($\langle \bar{H}_{1,2} \rangle$)	RHF	{1 σ_g , 1 σ_u }	0.306	7.337	15.454	17.428	
B	LDSRG(2) ($\langle \bar{H}_{1,2} \rangle$)	CASSCF(2,2)	{1 σ_g , 1 σ_u }	0.791	1.007	0.307	0.041	
C	LDSRG(2) ($\langle \bar{H}_{1,2} \rangle$)	CASSCF(2,2)	{1 σ_g , 1 σ_u , 2 σ_g , 2 σ_u }	0.064	0.280	0.080	0.012	
D	LDSRG(2) (eig. $\bar{H}_{1,2}$)	CASSCF(2,2)	{1 σ_g , 1 σ_u }	0.331	0.070	0.242	0.041	
E	2-QLDSRG(2) ($\gamma_3 = 0$)	CASSCF(2,2)	{1 σ_g , 1 σ_u }	0.327	0.055	0.235	0.039	
F	2-QLDSRG(2)	CASSCF(2,2)	{1 σ_g , 1 σ_u }	1.065	2.981	2.152	0.354	
G	1-QLDSRG(2) ($\gamma_3 = 0$)	CASSCF(2,2)	{1 σ_g , 1 σ_u }	2.455	6.422	4.591	1.203	
H	1-QLDSRG(2) ($\gamma_3 = 0$)	CASSCF(2,2)	{1 σ_g , 1 σ_u , 2 σ_g , 2 σ_u }	0.601	2.193	1.383	0.564	
I	1-QLDSRG(2) ($\gamma_3 = 0$)	CASSCF(2,2)	{1 σ_g , 1 σ_u , 2 σ_g , 2 σ_u , 3 σ_g , 3 σ_u }	0.324	0.511	0.071	-0.051	
J	1-QLDSRG(2)	CASSCF(2,2)	{1 σ_g , 1 σ_u }	1.061	2.732	1.890	0.327	
K	1-QLDSRG(2)	CASSCF(2,2)	{1 σ_g , 1 σ_u , 2 σ_g , 2 σ_u }	0.016	1.392	0.935	0.070	
L	1-QLDSRG(2)	CASSCF(2,2)	{1 σ_g , 1 σ_u , 2 σ_g , 2 σ_u , 3 σ_g , 3 σ_u }	-0.104	0.293	0.130	0.008	
M	1-QLDSRG(2)	CCSD NOs	{1 σ_g , 1 σ_u }	1.059	2.927	2.095	0.351	
FCI		RHF	All MOs	-1.172301	-1.066168	-1.010114	-1.000726	

3.2 Calibration

3.2.1 Noiseless simulations

To investigate the accuracy of the QDSRG procedure for quantum computing, we examine a numerical example. We consider the H_2 molecule at four geometries using a triple- ζ basis. As the H_2 molecule is stretched, the $1\sigma_g$ and $1\sigma_u$ orbitals become near-degenerate, and the reference state must be taken of the form $|\Psi_0\rangle = c_g |(1\sigma_g)^2\rangle + c_u |(1\sigma_u)^2\rangle$ to guarantee a continuous and qualitatively correct solution for all bond lengths. Table 3.1 reports the energy error with respect to a full configuration interaction (FCI) computation for the LDSRG(2) and the QLDSRG(2) methods. We report both the average energy $\langle \bar{H}_{1,2} \rangle$ and the eigenvalue of $\bar{H}_{1,2}$ using active spaces of various sizes and different orbitals choices. In addition to the $1\sigma_g$ and $1\sigma_u$ orbitals, which originate from the 1s shell, we consider active spaces augmented with the $2\sigma_g/2\sigma_u$ and $3\sigma_g/3\sigma_u$ orbitals (of mixed 2s/2p_z character). These are found to be the orbitals that give the most important energetic contributions at the equilibrium and stretched geometries. Active spaces that span the full 2s and 2p shells (including the $1\pi_u$ and $1\pi_g$ MOs) do not improve the energetics in a consistent way. In analyzing these results, we focus on the largest error and use the labels A–M to refer to a specific row of Table 3.1.

The importance of optimizing the orbitals is reflected in the significant difference in the accuracy of the LDSRG(2) $\langle \bar{H}_{1,2} \rangle$ when the orbitals $1\sigma_g$ and $1\sigma_u$ come from a restricted Hartree–Fock (RHF) or CASSCF calculation (using only the $1\sigma_g$ and $1\sigma_u$ as active MOs), whereby the latter optimizes both the

orbitals and coefficients of the determinants that define Ψ_0 . The LDSRG(2) error with RHF orbitals (A) is as large as $17.4 \text{ m}E_h \approx 0.47 \text{ eV}$ (at $r_{\text{H-H}} = 3 \text{ \AA}$), whereas CASSCF orbitals (B) give an error of ca. $1 \text{ m}E_h \approx 0.03 \text{ eV}$, and this error can be further reduced to less than $0.3 \text{ m}E_h$ (C) if the reference state is augmented with determinants formed out of a larger active space that includes the $2\sigma_g$ and $2\sigma_u$ orbitals. Diagonalization of $\bar{H}_{1,2}$ in an active space containing the $1\sigma_g$ and $1\sigma_u$ MOs (D) yields a maximum error similar to the one of case (C). Note that even with a full iterated solution of the equations, the LDSRG(2) method is not exact for two electrons and the potential energy curve of H_2 will deviate from FCI. This deviation is due to both truncation of the commutator expansion of \bar{H} and the use of a finite value of s .

For the QDSRG methods, we report two sets of results. We first examine the ones denoted with “ $\gamma_3 = 0$ ”, which use a three-body cumulant ($\tilde{\lambda}_3$) reconstructed from $\tilde{\lambda}_1$ and $\tilde{\lambda}_2$ [275, 267, 268, 276] and, therefore, differ slightly from the approximations defined in the previous section, where we set $\tilde{\lambda}_3 = 0$. The case $\gamma_3 = 0$ is consistent with the fact that a reference containing two electrons always yields a zero three-body RDM. Since the three-body cumulant contains disconnected contributions from products of the one- and two-body RDMs, its elements may be nonzero even for two-electron systems [268]. We note that the 2-QDSRG approach (E) leads to small errors (max $0.4 \text{ m}E_h$) that are similar to those of case D, where the energy comes from diagonalization of the LDSRG(2) $\bar{H}_{1,2}$. When we neglect entirely the three-body cumulant (F), the 2-QDSRG error increases for all points. This observation may be understood by considering how $\tilde{\lambda}_3$ enters into the DSRG equations. At the lowest order, $\tilde{\lambda}_3$ gives a scalar contribution to $\bar{H}_{1,2}$ via the

term $\frac{1}{4}\lambda_{uvw}^{xyz}(\langle mz||uv\rangle t_{xy}^{mw} + \langle we||xy\rangle t_{ez}^{uv})$, where implicit summation of repeated indices is assumed, and m and e run over all the doubly occupied and empty orbitals, respectively. We estimated this quantity using second-order perturbation theory and found that it explains the difference between the $\gamma_3 = 0$ and $\tilde{\lambda}_3 = 0$ energies of H_2 (and, therefore, provides also a means to correct for this difference). For example, at $r = 1.50 \text{ \AA}$, the contribution due to $\tilde{\lambda}_3$ amounts to about $-2.77 \text{ m}E_h$, a value close to minus the energy error increase (about $2.93 \text{ m}E_h$) seen between E and F.

The more drastic approximation (1-QDSRG) with $\gamma_3 = 0$ gives a large maximum error ($6.4 \text{ m}E_h$, G). In this case, it is possible to improve the accuracy by expanding the active space with a single or double set of σ_g/σ_u orbitals, reducing the maximum energy error to 2.2 and $0.5 \text{ m}E_h$ (H, I), respectively.

Interestingly, imposing $\tilde{\lambda}_3 = 0$ has a different impact on the 1-QDSRG, improving the agreement with FCI, an effect attributed to error cancellation. The different behavior of the “1-” and “2-” approximation going from $\gamma_3 = 0$ to $\tilde{\lambda}_3 = 0$ (e.g., E vs. F and G vs. J) is a consequence, in the latter case, of $\tilde{\lambda}_2$ not being included in the reconstruction of $\tilde{\lambda}_3$.

As mentioned earlier, a practical realization of the QDSRG scheme requires either two quantum computations (one to generate the orbitals and approximate cumulants plus a final diagonalization step) or it may use orbitals and cumulants from a polynomial-scaling classical method as a starting point. Here we demonstrate how this second option may be realized in practice using natural orbitals from coupled cluster theory [277]. In the results labeled “M”, we use coupled cluster theory with singles and doubles (CCSD) to compute an approximate unrelaxed density matrix γ_1^{CCSD} that spans the entire orbital

space. The orbitals are then rotated to the natural basis (defined as the basis in which γ_1^{CCSD} is diagonal). The active space occupation numbers are then scaled so that their sum equals to the number of electrons in the active orbitals (2) and these are used to reconstruct an approximate diagonal $\tilde{\lambda}_1$. The 1-QLDSRG(2) computations using CCSD natural orbitals (NOs) (M) give energies that are comparable to the ones using CASSCF(2,2) orbitals (J), with the energy difference between these two approximate methods being at most $0.2 \text{ m}E_h$ at $r_{\text{HH}} = 1.50 \text{ \AA}$. We reexamine the use of CCSD NOs as a way to reduce the cost of QDSRG computations in Sec. 3.3.

In Sec. 3.5.2, we provide a comparison of the QDSRG scheme with the DUCC downfolding approach for the H_2 molecule and the beryllium atom using data from Ref. [238]. Both methods employ an exponential unitary transformation of the Hamiltonian, but differ in several ways. For example, whereas, DUCC is formulated in a single-reference setting, the QDSRG method derives the A operator from a correlated state. This and other differences, have important consequences on the accuracy of these two methods, with our comparison showing that the QDSRG leads to smaller errors (up to an order of magnitude smaller), especially in computations with fewer active orbitals.

3.2.2 Sensitivity to noise

We conclude our initial assessment of the QDSRG approach by analyzing the sensitivity to stochastic errors introduced by quantum devices. As shown in Figure 3.1, step 2 of the QDSRG procedure allows for the approximate cumulants to be obtained from a quantum computation. In this case, there will

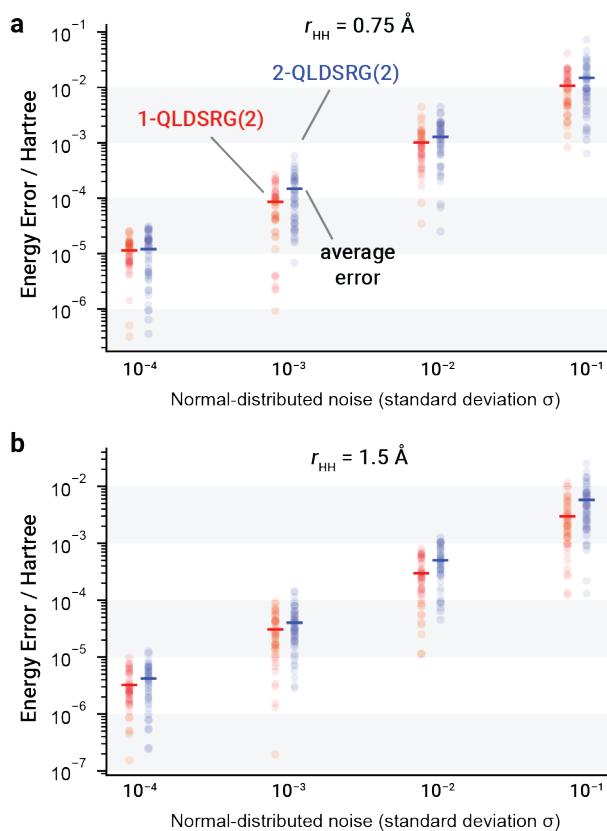


Figure 3.2: The energy error for the H_2 molecule (in mE_h) computed with the QLDSRG(2) with various amounts of stochastic noise (σ) added to the RDMs. For a given value of σ , the semiopaque circles aligned vertically show the distribution of errors from 50 computations, while the horizontal bars represent the average error. All computations use a cc-pVTZ basis [274] and the flow parameter value $s = 0.5 E_h^{-2}$. The energy errors are computed with respect to noiseless values. The data are obtained imposing $\gamma_3 = 0$ in the reconstruction of the approximate three-body cumulant.

be a compounding of errors due to the fact that the measured densities (later converted into cumulants) will be subject to finite measurement errors and gate and measurement noise.

To study the effect of noise on the measured RDMs, we performed QDSRG computations on the H_2 molecule at bond distances of 0.75 and 1.5 Å. Following Ref. [95], we model noise by augmenting the cumulants with stochastic error sampled from a Gaussian distribution with standard deviation σ and zero mean $[\mathcal{N}(0, \sigma^2)]$,

$$\gamma_{xy\dots}^{uv\dots, \text{measured}} = \gamma_{xy\dots}^{uv\dots} + \mathcal{N}(0, \sigma^2). \quad (3.13)$$

This simple noise model can mimic finite measurement errors, but cannot account for correlated noise among qubits and decoherence. Noise is added to the unique elements of the RDMs to avoid breaking antisymmetry with respect to permutation of the upper/lower indices (e.g., $\gamma_{xy}^{uv} = -\gamma_{xy}^{vu} = -\gamma_{yx}^{uv} = \gamma_{yx}^{vu}$); however, we do not enforce fermionic N -representability conditions [278, 279, 280, 281] onto the resulting RDMs, which likely leads to overestimating the resulting energy errors. Several works discuss how to utilize the N -representability constraints to accelerate and improve hybrid quantum algorithms mainly via reducing the measurement scaling [282, 252], which might be combined with the QDSRG approach to improve its accuracy.

Figure 3.2 shows the energy error computed with respect to noiseless results for the 1- and 2-QLDSRG(2) schemes (enforcing $\gamma_3 = 0$). At both geometries we observe that the 1-QLDSRG(2) is less sensitive to noise than the 2-QLDSRG(2), and that the average energy error increases linearly with σ .

Interestingly, the average error is slightly higher at the shorter bond distance (0.75 Å) than at the elongated one (1.5 Å). In both cases, a value of $\sigma = 0.01$ seems sufficient to recover the energy with an error less than 1 kcal/mol ($\approx 1.6 mE_h$), a threshold often referred to as *chemical accuracy*. These results can then inform an analysis of the quantum resources necessary to measure the RDMS with an accuracy sufficient for a hybrid quantum-classical procedure based on the QDSRG.

In summary, the preliminary results reported in Sec. 3.2.1 and 3.2.2 show that even a very drastic approximation of the cumulants that enter the DSRG *combined with* diagonalization of the resulting transformed Hamiltonian can yield energies with small absolute energy errors, even under the presence of noise. We expand this analysis to molecules with more complex electronic structures and larger basis sets in Sec. 3.3 with the goal of determining if it is possible to predict relative energies that approach chemical accuracy. There, we also report the results of experiments on NISQ devices that show the potential usefulness of QDSRG in leveraging near-term quantum computers.

3.3 Results and Discussion

In this section, we report two types of QDSRG results: the noiseless exact computations in Secs. 3.3.1 and 3.3.2, and device computations (Sec. 3.3.3) where we combine the QDSRG with variational quantum computations performed on IBM hardware.

3.3.1 Dissociation curve of the nitrogen molecule

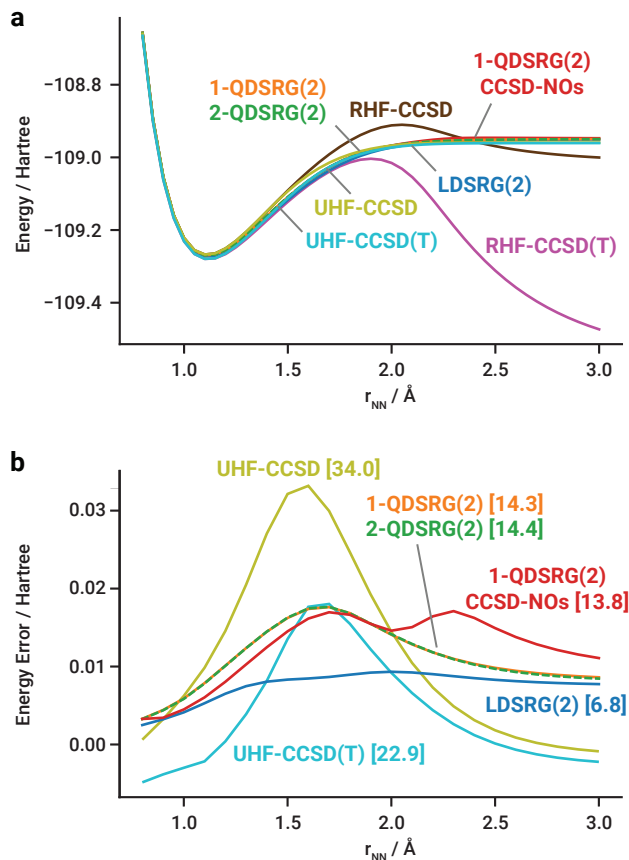


Figure 3.3: The dissociation curve for the ground-state N_2 computed with the LDSRG(2) and QLDSRG(2). (a) The total energy and (b) the energy error with respect to FCI in units of E_h . Nonparallelism errors (in mE_h) for each method are reported in square brackets. All computations use an active space containing six $2p$ N atomic orbitals, a cc-pVDZ basis [274], and the flow parameter value $s = 0.5 E_h^{-2}$. The 1-QLDSRG(2)-CCSD data employ natural orbitals and γ_1 from CCSD as the input to the QDSRG computation. All other results employ CASSCF(6,6) orbitals.

Table 3.2: Spectroscopic constants for the ground state ($X^1\Sigma_g^+$) of N_2 from the dissociation curves in Figure 3.3. The data in parentheses show deviations from FCI results. All LDSRG(2) and QLDSRG(2) computations as well as literature results listed here use the cc-pVDZ basis.

Method	$r_e/\text{\AA}$	ω_e/cm^{-1}	$\omega_e x_e/\text{cm}^{-1}$	D_e/eV
LDSRG(2)	1.1177 (-0.0024)	2344.6 (21.0)	15.0 (0.1)	8.766 (0.054)
2-QLDSRG(2)	1.1159 (-0.0042)	2365.2 (41.6)	14.8 (-0.1)	8.712 (0.000)
1-QLDSRG(2)	1.1159 (-0.0042)	2364.9 (41.3)	14.8 (-0.1)	8.716 (0.004)
1-QLDSRG(2) CCSD-NOs	1.1165 (-0.0036)	2365.6 (42.0)	15.3 (0.4)	8.834 (0.122)
UHF-CCSD	1.1123 (-0.0078)	2411.7 (88.2)	14.0 (-0.9)	8.396 (-0.316)
UHF-CCSD(T)	1.1184 (-0.0017)	2341.9 (18.3)	14.6 (-0.3)	8.700 (-0.012)
DMRG (6,6)-tCCSD ^a	1.1180 (-0.0022)	2327.0 (3.4)	-	-
MRCISD ^b	1.1192 (-0.0010)	2330.1 (6.5)	14.9 (-0.0)	-
MRCISD+Q ^b	1.1204 (0.0002)	2321.4 (-2.2)	14.9 (-0.0)	-
FCI	1.1202	2323.6	14.9	8.712

^a From Ref. [283]

^b From Ref. [284]

As the first benchmark of the QDSRG scheme, we compute the potential energy curve for the ground singlet state of N_2 using an active space containing six orbitals (built from combinations of the six 2p N orbitals). Figure 3.3a shows the potential energy curve for the LDSRG(2), the two approximate variants of the QDSRG, CCSD [177], and CCSD(T) [285]. In the DSRG computations, we employ CASSCF(6,6) orbitals and use the corresponding state as a reference, while the CCSD and CCSD(T) results employ restricted (RHF) and unrestricted broken symmetry (UHF) Hartree–Fock references. The DSRG methods produce curves that are nearly indistinguishable, except in the recoupling region (1.6–2.0 Å) where the QDSRG energy is slightly higher than the LDSRG(2) one. The RHF-CCSD and RHF-CCSD(T) curves, although accurate in the equilibrium region, deviate significantly from the DSRG one for large N–N distances, while the UHF-based counterparts give results that are close to the DSRG methods. In the bottom panel of Figure 3.3, we report the energy error with respect to FCI and the nonparallelism error (NPE), defined as the difference between the largest and smallest energy deviation from FCI along the dissociation curve. Here we notice that the 1- and 2-QLDSRG(2) lead to errors as large as $17.5 mE_h$ (and NPE as high as $14.4 mE_h$), while the LDSRG(2) is more accurate, with the maximum deviation from FCI always being less than $10 mE_h$. As observed for H_2 , the 1-QLDSRG(2) potential energy curve based on the CCSD-NOs reference is still accurate and displays maximum errors with respect to FCI smaller than those obtained using CASSCF orbitals and cumulants from exact diagonalization. In comparison, the UHF-based CCSD and CCSD(T) curves show larger deviations from FCI, with NPE values (22.9 and $34.0 mE_h$) larger than those of the 1- and 2-QLDSRG(2)

(14.3 and 14.4 mE_h).

Table 3.2 reports various spectroscopic constants, including the bond distance (r_e), the harmonic vibrational frequency (ω_e), the anharmonicity constant ($\omega_e x_e$), and the bond dissociation energy (D_e , electronic energy only) for the ground state ($X^1\Sigma_g^+$) of N_2 computed from the potential energy curves in Figure 3.3, as well as values from other methods, including the density matrix renormalization group [286], tailored coupled cluster theory with a CAS(6e,6o) active space [DMRG(6,6)-tCCSD] [283], MRCI with singles and doubles (MRCISD) [287, 288], and MRCISD with Davidson’s correction (MRCISD+Q) [289]. Notably, all LDSRG(2) and QLDSRG(2) computations yield results that considerably exceed the quality of the UHF-CCSD ones for all constants and dissociation energies, while the LDSRG(2) achieves an accuracy comparable to UHF-CCSD(T). While LDSRG(2) predicts an equilibrium bond length r_e similar to the DMRG(6,6)-tCCSD one, both LDSRG(2) and 2-QLDSRG(2) overestimate the vibrational constant ω_e .

3.3.2 Singlet-triplet gaps of *para*-benzyne

In our next example, we apply the QDSRG scheme to a medium-sized molecule. We compute the adiabatic singlet-triplet splitting ($\Delta E_{ST} = E_T - E_S$) of *para*-benzyne. The singlet ground state of this molecule exhibits pronounced diradical character and is dominated by two closed-shell determinants. *para*-benzyne and its isomers have been studied extensively both experimentally [292] and theoretically [290, 291, 293, 298, 299, 300, 297, 301, 302].

Table 3.3: Adiabatic singlet-triplet splittings ($\Delta E_{ST} = E_T - E_S$) in kcal mol⁻¹ of *para*-benzyne computed with the LDSRG(2) and QLDSRG(2) in the cc-pVTZ basis [274] with the flow parameter value $s = 1.0 E_h^{-2}$. The data in parentheses show the difference with respect to the experimental value of ΔE_{ST} (in kcal mol⁻¹). All LDSRG(2) and QLDSRG(2) results include a zero-point vibrational energy (ZPVE) correction equal to +0.30 kcal mol⁻¹ (see Ref. [290]). The geometries are taken from Ref. [291]. We use CASSCF(2,2) optimized orbitals for all computations of the singlet state and ROHF orbitals for the triplet state. For the LDSRG(2), the expectation value of the energy is designated with “ $\langle \bar{H}_{1,2} \rangle$ ”, while the lowest eigenvalue is indicated with “eig. $\bar{H}_{1,2}$ ”. For the QDSRG methods, we report two sets of data. Those labeled “ $\gamma_3 = 0$ ” use an approximate three-body cumulant reconstructed from approximate $\tilde{\lambda}_1$ and $\tilde{\lambda}_2$. All literature results listed here for comparison use the same cc-pVTZ basis.

Method	$\Delta E_{ST} / \text{kcal mol}^{-1}$
	Active orbitals: $\{\sigma_g, \sigma_u\}$
CASSCF(2,2)	0.31 (-3.49)
LDSRG(2) ($\langle \bar{H}_{1,2} \rangle$)	2.76 (-1.04)
LDSRG(2) (eig. $\bar{H}_{1,2}$)	3.48 (-0.32)
2-QLDSRG(2) ($\gamma_3 = 0$)	3.45 (-0.35)
1-QLDSRG(2) ($\gamma_3 = 0$)	3.22 (-0.58)
2-QLDSRG(2)	2.98 (-0.82)
1-QLDSRG(2)	3.38 (-0.42)
Mk-MRCCSD(T) ^{b,g}	4.45 (+0.65)
ic-MRCCSD(T) ^{c,g}	5.18 (+1.38)
DIP-EOM-CCSD ^f	4.40 (+0.60)
DEA-EOM-CCSD ^{e,h}	3.83 (+0.03)
SF-CCSD ^{d,h}	3.87 (+0.07)
Experiment ^a	3.8 ± 0.4

^a From Ref. [292]; experimental value taken from ultraviolet photoelectron spectra of *para*-benzyne radical anion.

^b From Ref. [291].

^c From Ref. [293].

^d From Ref. [294].

^e From Ref. [295].

^f From Ref. [296].

^g ZPVE correction of +0.30 kcal mol⁻¹ obtained using CCSD(T)/cc-pVDZ (see Ref. [290]) is included, same as that used for LDSRG(2) and QLDSRG(2).

^h ZPVE correction of 0.021 eV (+0.48 kcal mol⁻¹) at the SF-DFT/6-311G* level (see Ref. [297]) is included according to the paper.

Here we compute the singlet-triplet splitting using CASSCF(2,2) orbitals for the singlet state and ROHF orbitals for the triplet state. The experimental splitting value is taken from the ultraviolet photoelectron spectroscopy results of Ref. [292]. We utilize the singlet and triplet geometries from Ref. [291], which were optimized at the Mk-MRCCSD/cc-pVTZ level of theory. All computations use the cc-pVTZ basis set [274], and the value of the DSRG flow parameter is set to $1.0 E_h^{-2}$, based on previous studies [284, 269, 303]. We freeze the six 1s-like orbitals on carbon atoms in the DSRG correlation treatment.

Table 3.3 reports the singlet-triplet splitting obtained by the LDSRG(2) and the QLDSRG(2) methods. All splittings are shifted by $+0.30 \text{ kcal mol}^{-1}$ to account for zero-point vibrational energy (ZPVE) corrections [290]. Labels for methods are consistent with those in Table 3.1.

It is encouraging that most LDSRG(2) and QLDSRG(2) results are chemically accurate (deviation from experimental value less than 1 kcal mol^{-1}), with the largest deviation reaching $1.04 \text{ kcal mol}^{-1}$. For all QLDSRG(2) variants, the estimated ΔE_{ST} deviates from the LDSRG(2) (eig. $\bar{H}_{1,2}$) value by only $0.03 - 0.50 \text{ kcal mol}^{-1}$, which shows the robustness of the DSRG downfolding with respect to density cumulant approximations even for medium-sized systems. Interestingly, the simpler 1-QLDSRG(2) method more accurately estimates ΔE_{ST} ($3.38 \text{ kcal mol}^{-1}$) than the 2-QLDSRG(2) ($2.98 \text{ kcal mol}^{-1}$), likely due to error cancellation. For comparison, we also include in Table 3.3 theoretical ΔE_{ST} values from other methods, including Mukherjee’s multireference coupled cluster theory with singles, doubles, and perturbative triples [Mk-MRCCSD(T)] [291], internally contracted multirefer-

ence coupled cluster theory [ic-MRCCSD(T)] [293], double ionization potential and double electron attachment equation-of-motion coupled cluster theory with singles and doubles (DIP-EOM-CCSD [294] and DEA-EOM-CCSD [295]), and spin-flip coupled cluster theory with singles and doubles (SF-CCSD) [296, 297]. In general, both LDSRG(2) and QLDSRG(2) slightly underestimate ΔE_{ST} , while other methods tend to overestimate it by 0.03–1.38 kcal mol⁻¹. Most QLDSRG(2) splittings are more accurate than those from Mk-MRCCSD(T), ic-MRCCSD(T), and DIP-EOM-CCSD, while DEA-EOM-CCSD and SF-CCSD slightly outperform other methods.

3.3.3 Hardware implementation

In this section, we combine the 2-QLDSRG(2) method with the VQE [57, 58, 59] on the IBM quantum computers to demonstrate the ability of this hybrid scheme to compute the total energies under realistic noise from near-term quantum devices. We use the Qiskit [168] package to construct circuits and execute them on hardware.

Ideally, we would measure both density matrices and the QDSRG energy (steps 2 and 4 in Figure 3.1) from a quantum computation. Due to the high level of noise from near-term devices and the fact that density matrices are more sensitive to noise than the energy, we employ a quantum computer only to estimate the eigenvalue of the 2-QLDSRG(2) effective Hamiltonian $\bar{H}_{1,2}$. We use the VQE algorithm to optimize a trial wave function and measure its energy. To reduce the quantum resources (the number of qubits, the circuit depth, etc.) and minimize errors, we explore a symmetry-preserving one-qubit

ansatz (see Sec. 3.5.1 for details).

For each experiment on the device, we carry out the maximum number of measurements allowed, which differs by device. To ameliorate measurement errors, we utilize readout-error-mitigation tools in the Qiskit-Ignis module to construct a calibration matrix and apply its inverse to the raw measurement counts of each experiment.

Our first example is a computation of the dissociation curve of H_2 , which is a representative benchmark system for quantum computing. Figure 3.4 shows the dissociation curve and the energy error for the H_2 molecule in the cc-pV5Z basis [274] (110 orbitals) obtained by the one-qubit 2-QLDSRG(2) computations on the `ibmq_lagos` quantum computer. A direct second-quantized quantum computation would require 220 qubits (ignoring qubit tapering or other symmetry adaptation techniques). We also report the 2-QLDSRG(2) energy errors and the standard deviations of the device results in Table 3.4. The effectiveness of the QDSRG downfolding method can be seen from the small errors of the 2-QLDSRG(2) energies, which differ from noiseless simulations at most by $0.5 mE_h$ for all geometries. The 2-QLDSRG(2) energies from the device have unsigned average errors lower than $1 mE_h$ for over half of the geometries, with a maximum error of $2.0 mE_h$. Empirically, it is important to collect the measurement statistics of 10^5 shots to obtain a reliable estimate of the average energy from the device. We observe that device results have relatively large errors for short bond distances. This is due to the behavior of the matrix element c_z in the qubit Hamiltonian, which enters via the term $c_z Z$ [see Eq. (3.18) in Sec. 3.5.1]. By definition, c_z is half the energy difference between the $(1\sigma_g)^2$ and $(1\sigma_u)^2$ electron configurations generated by the VQE

Table 3.4: The errors of 2-QLDSRG(2) energies in mE_h (with respect to FCI energies) along the H_2 dissociation curve (Figure 3.4). For results from the `ibm_lagos` device, we show the unsigned average energy errors and standard deviations (in mE_h). Unsigned energy errors below $1 mE_h$ are highlighted in bold type.

$r/\text{\AA}$	$\Delta E_{\text{noiseless}}$	ΔE_{device}	Standard deviation
0.6	0.53	2.02	2.08
0.65	0.54	1.59	1.63
0.7	0.54	1.28	1.14
0.75	0.55	2.10	1.24
0.8	0.54	1.32	1.41
0.85	0.54	0.63	1.47
1.15	0.40	0.19	1.61
1.2	0.37	0.59	1.00
1.3	0.32	1.24	1.42
1.45	0.28	0.00	0.89
1.6	0.29	0.89	0.56
1.9	0.36	0.68	0.77
2.5	0.20	0.38	0.35
2.95	0.07	0.19	0.45
6.0	0.00	0.31	0.15

trial state. As the H_2 bond is stretched and the two configurations become near-degenerate, c_z decreases by several orders of magnitude (-0.819 at 0.70\AA , while -0.036 for 2.95\AA), reducing the impact of the error in the estimation of the expectation value of Z at large r values.

From this example, we see that errors from hardware (finite measurements, decoherence, etc.) are more significant than errors from the QDSRG downfolding.

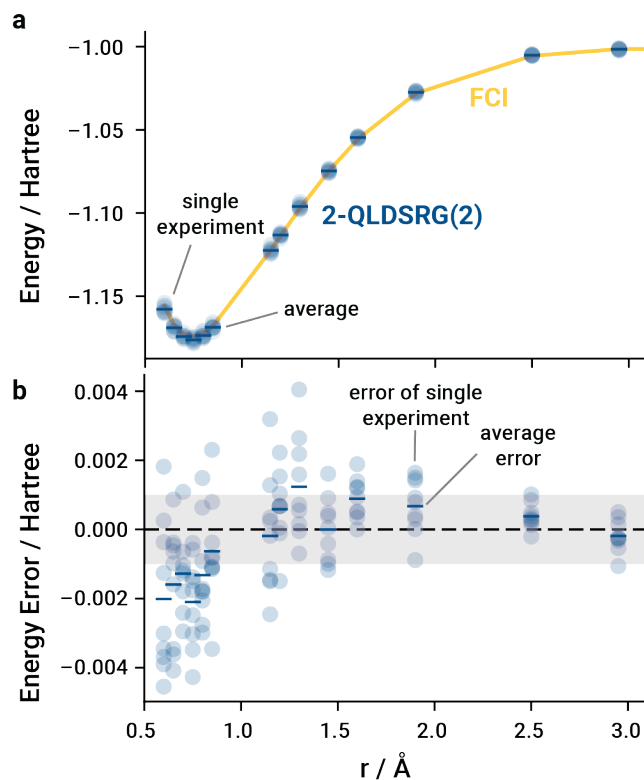


Figure 3.4: The dissociation curve (a) and the energy error (b) for the H_2 molecule computed with the 2-QLDSRG(2) using one qubit on the `ibm_lagos` device. The energy errors are with respect to FCI energies. For each geometry, the semiopaque blue circles aligned vertically show the distribution of energies (energy errors) from 9 experiments, with each experiment consisting of 32000 measurements, while the horizontal bars in blue denote average energies or average energy errors. All computations use the cc-pV5Z basis [274] (110 basis functions), CASSCF(2,2) orbitals, and the flow parameter value $s = 0.5 E_h^{-2}$. The gray-shaded area indicates unsigned energy errors below $1 mE_h$. The unsigned energy errors and the standard deviations are reported in Table 3.4.

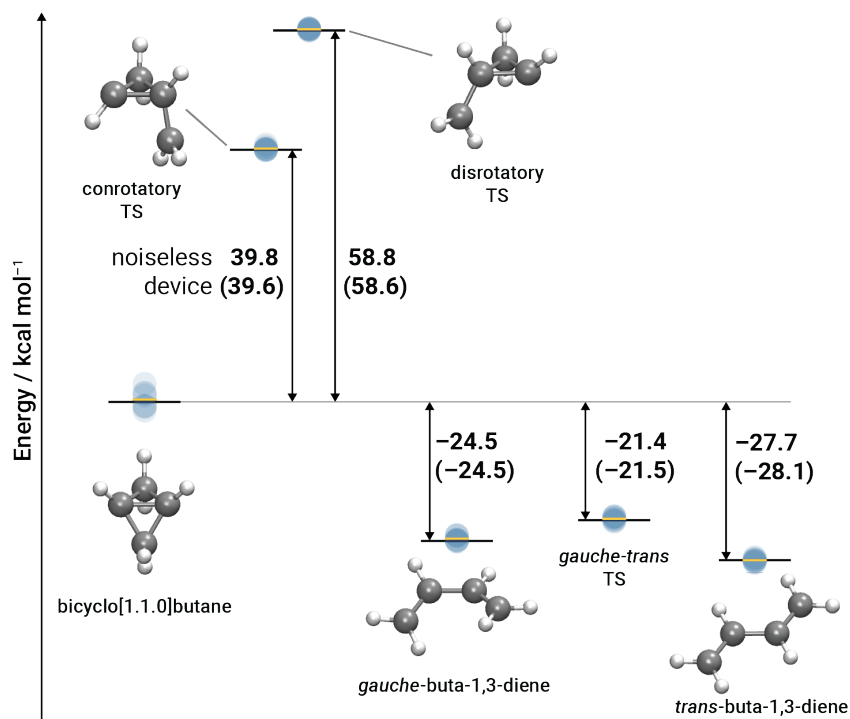


Figure 3.5: Conrotatory and disrotatory pathways describing the isomerization of bicyclo[1.1.0]butane (bicyclobutane) to *trans*-buta-1,3-diene (*trans*-butadiene). The enthalpies in kcal mol⁻¹ are relative to the reactant for relevant stationary points computed with the 2-QLDSRG(2) method using one qubit on the device *ibmq_manila*. The black horizontal bars represent the 2-QLDSRG(2) results obtained with noiseless simulations. The device results are shown in parentheses. The semiopaque blue circles aligned vertically show the distribution of the relative enthalpies from eight experiments (20000 measurements per experiment), while the yellow horizontal bars denote the average relative enthalpies. We use a cc-pVTZ basis [274] (204 basis functions) and CASSCF(2,2) natural orbitals, and the flow parameter value $s = 1.0 E_h^{-2}$ for all six stationary points.

Table 3.5: LDSRG(2) and QLDSRG(2) (exact and device) computations of the relative enthalpies (in kcal mol⁻¹) with respect to the bicyclobutane reactant of the conrotatory transition state and the disrotatory transition state, the *gauche*-butadiene intermediate, the transition state connecting *gauche*-butadiene and *trans*-butadiene, and the *trans*-butadiene product. We use the cc-pVTZ basis [274] (204 basis functions) and CASSCF(2,2) natural orbitals, and the flow parameter value $s = 1.0 E_h^{-2}$. All results include zero-point vibrational energy (ZPVE) corrections taken from Ref. [304]. The OMR3-DMC and CC(t;3) results also use the cc-pVTZ basis. The differences of values (in kcal mol⁻¹) with respect to the experimental data for the conrotatory transition state and *trans*-butadiene are shown in parentheses; values within 1 kcal mol⁻¹ deviation are indicated in bold type.

	conrotatory TS	disrotatory TS	<i>gauche</i> -butadiene	<i>gauche-trans</i> TS	<i>trans</i> -butadiene
LDSRG(2) ($\langle \bar{H}_{1,2} \rangle$)	41.3 (0.7)	58.5	-24.5	-21.5	-27.7 (-1.8)
LDSRG(2) (eig. $\bar{H}_{1,2}$)	39.6 (-1.0)	58.6	-24.5	-21.4	-27.8 (-1.9)
		2-QLDSRG(2)			
Exact	41.5 (0.9)	58.9	-24.3	-21.3	-27.5 (-1.6)
ibmq_manila ^a	42.6 (2.0)	57.8	-23.8	-22.2	-27.4 (-1.5)
ibm_lagos ^b	42.7 (2.1)	59.6	-23.3	-20.7	-26.4 (-0.5)
ibmq_jakarta ^c	40.5 (-0.1)	57.5	-25.6	-22.4	-28.4 (-2.5)
		2-QLDSRG(2) ($\gamma_3 = 0$)			
Exact	39.8 (-0.8)	58.8	-24.5	-21.4	-27.7 (-1.8)
ibmq_manila ^a	39.6 (-1.0)	58.6	-24.5	-21.5	-28.1 (-2.2)
ibm_lagos ^b	39.0 (-1.6)	57.7	-25.2	-22.2	-28.6 (-2.7)
ibmq_jakarta ^c	39.1 (-1.5)	58.4	-25.2	-21.7	-28.0 (-2.1)
OMR3-DMC ^d	40.4(5)	58.6(5)	-25.2(5)	-22.2(5)	-27.9(5)
CC(t;3) ^e	40.2	60.1	-25.3	-22.6	-28.3
Experiment	40.6 ± 2.5 ^f				-25.9 ± 0.4 ^g

^a The average is over 8 experiments (20000 shots per experiment).

^b The average is over 10 experiments (32000 shots per experiment).

^c The average is over 10 experiments (20000 shots per experiment).

^d From Ref. [305].

^e From Ref. [251].

^f From Ref. [306].

^g The reaction enthalpy at 298 K is based on enthalpies of the formation of bicyclo[1.1.0]butane and buta-1,3-diene reported in Ref. [307].

For our second set of hardware experiments, we consider a larger and more chemically-relevant problem, the pericyclic rearrangement reaction of bicyclo[1.1.0] butane (bicyclobutane) to *trans*-buta-1,3-diene (*trans*-butadiene). This isomerization process goes through a concerted conrotatory movement of the methylene groups with an activation barrier (enthalpy) of 40.6 ± 2.5 kcal mol⁻¹ [306], suggested by early experimental studies [306, 308, 309, 310, 311]. This mechanism has been investigated in many computational studies using high-level electronic structure methods, including MRMBPT [304, 312, 313], multi-reference configuration interaction (MRCI) [313], variants of single-reference coupled-cluster methods including CR-CC(2,3) [304, 314] and CC(t;3) [251], the diffusion quantum Monte Carlo [305] and the anti-Hermitian contracted Schrödinger equation (ACSE) method [312, 315].

These theoretical studies also investigate the unfavored concerted disrotatory pathway [304, 314, 312, 305, 313], characterized by a transition state (TS) that is estimated to be 15–25 kcal mol⁻¹ higher in energy than the conrotatory one. Both transition states display significant biradical character [304], and their ground state wave functions have large contributions from multiple determinants, requiring a multireference treatment. This makes the system suitable to treat with the QDSRG method. Previous studies also confirmed that for both concerted pathways, the reaction reaches a *gauche*-buta-1,3-diene intermediate (*gauche*-butadiene), and then proceeds through a low-energy rotational barrier to the *trans*-butadiene product.

We compute the reaction enthalpies along the full concerted conrotatory and disrotatory pathways from bicyclobutane to *trans*-butadiene. Cartesian coordinates of the structures of all six stationary points optimized at the

CASSCF(10,10)/cc-pVDZ level of theory are taken from Ref. [304]. Zero-point vibrational energies (ZPVE) obtained at the same level of theory are used to convert total electronic energies to enthalpies. For all six stationary points, we use CASSCF(2,2) natural orbitals, which yield a two-configuration reference that can be mapped to a one-qubit ansatz (see Sec. 3.5.1 for details). All computations use the cc-pVTZ basis [274] (204 orbitals) and we freeze four 1s-like orbitals on carbon atoms in the DSRG correlation treatment.

Figure 3.5 shows the concerted conrotatory and disrotatory pathways of the bicyclobutane \rightarrow *trans*-butadiene reaction and Table 3.5 reports the relative enthalpies (with respect to the bicyclobutane reactant) from the LDSRG(2) and the 2-QLDSRG(2) methods obtained via noiseless simulations and via VQE on three quantum devices. We show the best device results, obtained with the `ibmq_manila` device, in Figure 3.5.

Compared to the experimental value [306], both LDSRG(2) and the 2-QLDSRG(2) methods give relative enthalpies of the conrotatory transition state that achieve chemical accuracy, while the relative enthalpies of *trans*-butadiene predicted by the two methods are slightly underestimated [307]. For the other three stationary points, experimental data are not available; therefore, we compare our results with data from two high-level approaches, the optimized multireference diffusion quantum Monte Carlo (OMR3-DMC) [305] and an active-space coupled-cluster method with corrected triple excitations termed CC(t;3) [251] using the same cc-pVTZ basis. The relative enthalpy of the disrotatory transition state predicted by the LDSRG(2) and 2-QLDSRG(2) methods agrees with the OMR3-DMC result (58.6 kcal mol⁻¹)

[305] and is slightly lower than the CC(t;3) value (60.1 kcal mol⁻¹) [251]. For both *gauche*-butadiene and the transition state connecting *gauche*-butadiene and *trans*-butadiene, the LDSRG(2) and the 2-QLDSRG(2) results are about 1 kcal mol⁻¹ lower than the OMR3-DMC and CC(t;3) values. The 2-QLDSRG(2) results from three devices are in good agreement with the result from noiseless simulations, with most devices yielding values within 1 kcal mol⁻¹ from the exact result. Notably, two devices yield chemically accurate relative enthalpies for the conrotatory transition state (40.5 kcal mol⁻¹, 39.6 kcal mol⁻¹). The best device results in Table 3.5 give unsigned errors less than 0.5 kcal mol⁻¹ for all six stationary points.

The results for the bicyclobutane \rightarrow *trans*-butadiene reaction demonstrate that the QDSRG method can effectively downfold the dynamical correlation for a large basis with 204 orbitals, reducing the number of qubits from several hundred to just one.

3.4 Summary

In this work, we introduced a practical unitary downfolding method that enables accurate molecular computations on near-term quantum computers. The QDSRG is agnostic to the type of quantum algorithm (e.g., variational, phase estimation) and can be used with both noisy near-term computers and future fault-tolerant hardware. Therefore, we expect that the QDSRG will be a useful method to leverage small quantum computers in applications to large molecules and large basis sets.

The QDSRG is based on the driven similarity renormalization group

(DSRG) [242], a classical numerically-robust and polynomial-scaling approach to block-diagonalize many-body Hamiltonians. In this work, we propose a “diagonalize-then-dress-then-diagonalize” strategy that combines truncation of the reduced density cumulants provided to the DSRG with diagonalization of the resulting similarity-transformed Hamiltonian. This downfolding procedure may be justified by a perturbative analysis of the DSRG equations and leads to two practical computational schemes: in the 1-QDSRG we retain only the diagonal part of the one-body RDM, whereas in the 2-QDSRG we retain the full one-body RDM and the diagonal part of the two-body cumulants. These two schemes require estimating a number of reduced density matrix elements that is at most linear or quadratic in the number of active orbitals (N_A), substantially reducing the demands of conventional multireference theories, which require N_A^6 to N_A^8 RDM elements.

Our calibration of the QDSRG shows that the use of orbitals optimized for a reference correlated state is crucial to compute accurate energies. The QDSRG results show that the 2- approximation is able to accurately predict energies along the bond-breaking coordinate in a minimal active space. The 1- approximation leads to larger errors, but these can be suppressed by increasing the active space size. To simulate the effect of noise, we examined QDSRG computations starting with inaccurate RDMs and found that milliHartree accuracy can be retained when the standard deviation of the RDMs errors is as large as 10^{-3} – 10^{-2} .

In our computations on the more challenging N_2 and *p*-benzyne molecules, we were also able to accurately predict potential energy curves and singlet-triplet gaps using the QDSRG. In the case of N_2 , we demonstrate how the first

two steps of the QDSRG procedure (orbital optimization and reference preparation) could be approximated with the classical polynomial-scaling CCSD method, using the corresponding one-body reduced density matrix. Finally, we demonstrate the QDSRG procedure in combination with the VQE algorithm on the IBM quantum devices. We extend computations of the H_2 dissociation curve with a nearly-complete quintuple- ζ basis, corresponding to a full computation with 220 qubits. In this example, we find that hardware errors still remain the most significant source of error in comparison to the QDSRG downfolding error. We also apply the QDSRG method to model the reaction pathways of the bicyclobutane \rightarrow *trans*-butadiene isomerization process using a basis of 204 orbitals. We are able to obtain high-quality device results that reach sub-kcal mol⁻¹ accuracy with respect to the exact QDSRG and two high-level classical electronic structure approaches with a modest number of measurements, while a full VQE computation may need 10^9 number of measurements for one single energy evaluation based on the empirical resource estimation of Ref. [316].

The extension of the QDSRG with explicit correlation methods and to electronically excited states are two interesting directions worth exploring. We expect that with the availability of more accurate hardware and a larger number of qubits, the QDSRG will provide a systematic path to perform accurate quantum chemistry computations on chemically relevant systems.

Table 3.6: Summary of the number of qubits required for the full-space and QDSRG computations that use large basis sets in this study.

	basis set	$N_q(\text{full-space})$	Active space	$N_q(\text{QDSRG})$
<i>para</i> -benzynes	cc-pVTZ	236	(2e, 2o)	1
H ₂	cc-pV5Z	220	(2e, 2o)	1
bicyclobutane	cc-pVTZ	408	(2e, 2o)	1

3.5 Appendix

3.5.1 Symmetry-preserving ansatz for two-configuration wave functions

We exploit spin, particle number, and spatial symmetries to construct a hardware-efficient ansatz for two-configuration wave functions. Consider a two-electron wave function in a basis of two molecular orbitals ψ_1, ψ_2 . The singlet ground state in the most general case includes three configurations (bars over the number denote β spin orbitals),

$$\begin{aligned}
 |\Phi_1\rangle &= |\psi_1\psi_{\bar{1}}\rangle, \\
 |\Phi_2\rangle &= |\psi_2\psi_{\bar{2}}\rangle, \\
 |\Phi_3\rangle &= \frac{1}{\sqrt{2}}(|\psi_1\psi_{\bar{2}}\rangle - |\psi_{\bar{1}}\psi_2\rangle).
 \end{aligned}
 \tag{3.14}$$

We can remove the contribution of the open-shell configuration $|\Phi_3\rangle$ from the normalized ground-state wave function $|\Psi_0\rangle = C'_1|\Phi_1\rangle + C'_2|\Phi_2\rangle + C'_3|\Phi_3\rangle$

without changing the energy via an orbital rotation

$$\begin{aligned} |\psi'_1\rangle &= \cos\theta |\psi_1\rangle + \sin\theta |\psi_2\rangle, \\ |\psi'_2\rangle &= \sin\theta |\psi_1\rangle - \cos\theta |\psi_2\rangle, \end{aligned} \tag{3.15}$$

where $\tan 2\theta = \frac{\sqrt{2}C'_3}{(C'_1 - C'_2)}$ [317, 318, 290]. We refer interested readers to Ref. [290] (Sec IV.) for detailed discussions on this basis transformation.

For H_2 , the ground-state wave function expanded in the CASSCF(2,2) orbitals can be accurately described by two closed-shell configurations. While for two transition states in the bicyclobutane \rightarrow *trans*-butadiene reaction, the open-shell contribution to the wave function cannot be neglected due to the strong biradical character (especially for the disrotatory TS). Therefore, we transform to the CASSCF(2,2) natural orbital basis, which is mathematically equivalent to enforcing Eq. 3.15. The ground states of the other four stationary points in the pathways are generally well described by a single determinant in the CASSCF(2,2) basis; however, for consistency, we employ CASSCF(2,2) natural orbitals for all computations.

The resulting two-configuration wave function $|\Psi_0\rangle = C_1 |\psi'_1\psi'_1\rangle + C_2 |\psi'_2\psi'_2\rangle$ can be mapped to a one-qubit space

$$\begin{aligned} |\psi'_1\psi'_1\rangle &\rightarrow |0\rangle, \\ |\psi'_2\psi'_2\rangle &\rightarrow |1\rangle, \end{aligned} \tag{3.16}$$

which leads to the one-qubit wave function ansatz

$$|\Psi\rangle = C_1 |0\rangle + C_2 |1\rangle. \tag{3.17}$$

This state can be prepared by applying to the $|0\rangle$ state a single Y-rotation gate $\hat{R}_y(t) = e^{-\frac{itY}{2}}$ with one variational parameter t , giving $C_1 = \cos(\frac{t}{2})$, $C_2 = \sin(\frac{t}{2})$. The Hamiltonian in the one-qubit basis is represented as $H = h_{00}|0\rangle\langle 0| + h_{11}|1\rangle\langle 1| + h_{10}(|0\rangle\langle 1| + |1\rangle\langle 0|)$ where h_{00} , h_{11} , h_{10} are calculated from the one- and two-electron integrals. The Hamiltonian can be decomposed into a weighted sum of single-qubit Pauli operators

$$H = c_0 + c_z Z + c_x X, \quad (3.18)$$

with coefficients given by $c_0 = (h_{00} + h_{11})/2$, $c_z = (h_{00} - h_{11})/2$, $c_x = h_{10}$.

The expectation value of this one-qubit Hamiltonian with respect to $|\Psi\rangle$ has the definite tomography [319, 320] given by

$$\langle H \rangle_t = a + b \cos t + c \sin t, \quad (3.19)$$

The coefficients a, b, c can be found using a three-point Fourier quadrature [319] that requires measuring expectation values for three parameters t_0, t_1, t_2 . The corresponding linear equation to solve is:

$$\begin{pmatrix} 1 & \langle Z \rangle_{t_0} & \langle X \rangle_{t_0} \\ 1 & \langle Z \rangle_{t_1} & \langle X \rangle_{t_1} \\ 1 & \langle Z \rangle_{t_2} & \langle X \rangle_{t_2} \end{pmatrix} \begin{pmatrix} a \\ b \\ c \end{pmatrix} = \begin{pmatrix} \langle H \rangle_{t_0} \\ \langle H \rangle_{t_1} \\ \langle H \rangle_{t_2} \end{pmatrix}.$$

In this work, we use the following three-point Fourier quadrature:

$$t_0, t_0 - \pi/3, t_0 + \pi/3, \quad (3.20)$$

Table 3.7: The relations between the elements of the fermionic 1-RDM ($\gamma_q^p = \langle a_p^\dagger a_q \rangle$) and 2-RDM ($\gamma_{rs}^{pq} = \langle a_p^\dagger a_q^\dagger a_s a_r \rangle$) and the measured quantities for the one-qubit ansatz. Only nonzero elements are shown; others are zero due to symmetries. $|C_1|^2 = \langle \Psi|0\rangle \langle 0|\Psi\rangle$ and $|C_2|^2 = \langle \Psi|1\rangle \langle 1|\Psi\rangle$ are obtained from projective measurements [51, 321] of the optimized state in the computational basis; $\langle X \rangle$ is the expectation value of the Pauli X operator.

RDM element	Analytical	Measurement
$\gamma_1^1, \gamma_{\bar{1}}^{\bar{1}}, \gamma_{\bar{1}\bar{1}}^{\bar{1}\bar{1}}, \gamma_{\bar{1}\bar{1}}^{\bar{1}\bar{1}}$	$\cos^2 \frac{t}{2}$	$ C_1 ^2$
$\gamma_2^2, \gamma_{\bar{2}}^{\bar{2}}, \gamma_{\bar{2}\bar{2}}^{\bar{2}\bar{2}}, \gamma_{\bar{2}\bar{2}}^{\bar{2}\bar{2}}$	$\sin^2 \frac{t}{2}$	$ C_2 ^2$
$\gamma_{\bar{1}\bar{1}}^{\bar{1}\bar{1}}, \gamma_{\bar{1}\bar{1}}^{\bar{1}\bar{1}}$	$-\cos^2 \frac{t}{2}$	$- C_1 ^2$
$\gamma_{\bar{2}\bar{2}}^{\bar{2}\bar{2}}, \gamma_{\bar{2}\bar{2}}^{\bar{2}\bar{2}}$	$-\sin^2 \frac{t}{2}$	$- C_2 ^2$
$\gamma_{\bar{2}\bar{2}}^{\bar{1}\bar{1}}, \gamma_{\bar{2}\bar{2}}^{\bar{1}\bar{1}}, \gamma_{\bar{1}\bar{1}}^{\bar{2}\bar{2}}, \gamma_{\bar{1}\bar{1}}^{\bar{2}\bar{2}}$	$\cos \frac{t}{2} \sin \frac{t}{2}$	$\langle X \rangle / 2$
$\gamma_{\bar{2}\bar{2}}^{\bar{1}\bar{1}}, \gamma_{\bar{2}\bar{2}}^{\bar{1}\bar{1}}, \gamma_{\bar{1}\bar{1}}^{\bar{2}\bar{2}}, \gamma_{\bar{1}\bar{1}}^{\bar{2}\bar{2}}$	$-\cos \frac{t}{2} \sin \frac{t}{2}$	$-\langle X \rangle / 2$

where t_0 is arbitrary. For convenience, we use the analytic solution for the optimal angle

$$t_0 = \arctan2(c_x, c_z). \quad (3.21)$$

For the reference preparation (step 2 in Figure 3.1), we run the VQE algorithm to obtain the 1- and 2-RDMs. These quantities can be measured from the state tomography of the optimal wave function. Table 3.7 summarizes the expressions for the 1- and 2-RDMs in terms of analytical expressions of the variational parameter t and quantities from direct measurements.

Note that for both the 1- and 2-QDSRG methods, we only need to measure the Pauli Z operator to compute the full 1-RDM and the approximate 2-RDM, while the Pauli X operator only contributes to the non-diagonal components of the two-body reduced density cumulant. Finally, we use the VQE algorithm to estimate the eigenvalue of the DSRG effective Hamiltonian (step 4 in Figure 3.1).

3.5.2 Comparing QDSRG with double unitary coupled cluster approach

Table 3.8: A comparison of the energy errors (in mE_h) of the QDSRG and the DUCC for the H_2 molecule at four bond lengths in the cc-pVTZ basis using DSRG flow parameter $s = 0.5 E_h^{-2}$. The size of the active space is denoted in parentheses. The energy errors are with respect to the full-space (30-orbital) FCI computations [absolute energies (in E_h) are shown in the first row]. The DUCC data are taken from Ref. [238].

Method	Orbital type (N_{act})	0.8 a.u.	1.4008 a.u.	4.00 a.u.	10.00 a.u.
FCI (full space)	RHF (30)	-1.015729	-1.172455	-1.014872	-0.999623
FCI (active space)	RHF (4)	32.729	25.755	7.872	2.523
DUCC	RHF (4)	7.129	4.555	-0.328	-1.977
LDSRG(2) (diag. $\bar{H}_{1,2}$)	RHF (4)	-0.130	-0.234	1.920	0.122
1-QLDSRG(2)	RHF (4)	-0.094	-0.098	4.047	0.524
2-QLDSRG(2)	RHF (4)	-0.087	-0.084	3.794	0.126
1-QLDSRG(2)	CASSCF(2,2) (4)	0.455	0.169	1.498	0.006
2-QLDSRG(2)	CASSCF(2,2) (4)	0.460	0.179	1.662	0.006

Here we compare the QDSRG method with the DUCC downfolding technique for the H_2 molecule and the Be atom. In Table 3.8, we report energies of H_2 at four geometries obtained by diagonalizing the bare, the QDSRG-downfolded, and the DUCC downfolded Hamiltonians in a four-orbital active space, together with the energy errors with respect to the full-space FCI results which use 30 orbitals. We also compute QDSRG energies using different types of orbitals. The DUCC data are taken from Ref. [238]. We observe that for three geometries, all QDSRG computations consistently give less significant energy errors than the DUCC results. For instance, the largest error for the DUCC using RHF orbitals is 7.13 mE_h , while the QDSRG shows smaller errors (at most 4.1 mE_h). The use of CASSCF orbitals further reduces the maximum QDSRG errors to at most 1.7 mE_h .

Table 3.9: A comparison of the energy errors (in mE_h) of the QDSRG and the DUCC for the Be atom with different basis sets and active spaces. The DSRG flow parameter $s = 2.0 E_h^{-2}$. All computations use RHF orbitals. The energy errors are with respect to the full-space FCI computations [absolute energies (in E_h) are shown in the last column], which use 14, 30 and 55 orbitals for the cc-pVDZ, cc-pVTZ, and cc-pVQZ basis sets, respectively. The DUCC data are taken from Ref. [238].

Method	5 orbitals	6 orbitals	9 orbitals	All orbitals
cc-pVDZ				
FCI	22.242	20.575	0.493	-14.617409
DUCC	19.009	18.109	1.809	
1-QLDSRG(2)	3.408	1.998	3.067	
2-QLDSRG(2)	3.430	2.074	3.065	
cc-pVTZ				
FCI	34.881	33.621	7.024	-14.623810
DUCC	26.710	24.410	5.010	
1-QLDSRG(2)	4.199	3.202	1.216	
2-QLDSRG(2)	4.200	3.192	2.751	
cc-pVQZ				
FCI	54.950	54.366	26.798	-14.640147
DUCC	30.547	27.547	7.347	
1-QLDSRG(2)	4.927	4.166	0.879	
2-QLDSRG(2)	4.923	4.158	2.909	

Tab. 3.9 shows the comparison of the Be atom results using active spaces of different sizes and three basis sets. Here we see that the DUCC method introduces errors in the range of 18–30.5 mE_h when five or six active orbitals are used, and that this error is reduced to smaller values (1.8–7.3 mE_h) when using nine active orbitals, while QDSRG results consistently show much smaller energy errors (0.9–4.9 mE_h) for all active spaces and basis sets. Notably, the QDSRG downfolding is most effective for the large cc-pVQZ basis, which significantly reduces the energy errors of the active-space FCI results by 50, 50.2 and 26 mE_h for five-, six- and nine-orbital active spaces, while the DUCC method merely gives a reduction of 24, 27 and 19 mE_h .

Chapter 4

Simulating conical intersections on quantum computers with unitarily downfolded Hamiltonians

Solving the electronic structure of strongly correlated systems with sufficient accuracy is a challenging task in computational quantum chemistry and material science [4]. These problems are argued as the most promising applications for quantum computers to achieve a practical quantum speedup [9, 322, 1]. Though the debate regarding the existence of the exponential quantum advantage for determining quantum chemistry problems in general is still ongoing [323], many efforts have been undertaken to maximize the impact of near-term small-scale quantum devices to obtain the ground state of the time-independent Schrödinger equation in a problem-tailored manner [137, 205, 215, 225, 238, 254]. Quantum algorithms for computing excited states are less explored and have primarily been tested on small diatomic

molecules in minimal one-electron computational basis sets [91, 113, 112, 324]. However, achieving accurate modeling of realistic excited-state dynamics in numerous photochemical processes requires the utilization of large basis sets. This, in turn, demands a substantial number of qubits that exceeds the capabilities of near-term quantum computers. One of the most promising strategies to resolve excited-state energy surfaces using limited quantum resources is quantum downfolding based on effective Hamiltonian theories [325, 238, 239, 240].

In a recent work, we have introduced a practical quantum unitary downfolding scheme based on the driven similarity renormalization group (QDSRG) that enables accurate ground-state molecular computations on near-term noisy small-scale quantum devices. Notably, our device results have achieved *chemical accuracy* (relative energies within 1 kcal mol⁻¹ from experimental energies) in modeling the reaction pathways of the bicyclobutane \rightarrow *trans*-butadiene isomerization process utilizing a large basis set with 204 orbitals [325].

This work aims to extend the QDSRG scheme to treat near-degenerate excited states via a state-averaged downfolding formalism (SA-QDSRG) [326]. We note that such state-averaged formalism has been employed in several multireference excited-state electronic structure methods [327, 191, 202]. Consistent with the previous work, we reduce the cost of measuring reduced density matrices (RDMs) from quantum devices via a systematic truncation of RDMs. We combine the SA-QDSRG scheme with the variational quantum eigensolver (VQE) to calculate ground states and the quantum subspace expansion (QSE) [91, 113] algorithm to obtain excited states.

We are particularly interested in studying near-degenerate states in ethylene photodynamics. Ethylene is an important prototype system for understanding the ultrafast energy conversion through nonadiabatic transitions, and has been investigated in many computational studies using high-level electronic structure methods [193, 328, 329, 330, 331, 332, 333, 334]. The ethylene photodynamics is characterized by the following processes, with geometrical coordinates defined in Fig. 4.1. Following a vertical $\pi\pi^*$ excitation to the first valence state S_1 , the system's potential energy decreases through a torsional motion (torsion angle τ) around the C-C bond, transitioning from a planar geometry to a twisted-orthogonal structure (see the upper panel in Fig. 4.1). In this structure, two planes defined by two CH_2 groups are orthogonal to each other. Subsequently, the energy of the S_1 state is reduced by a **pyramidalization** motion (angle β) of one CH_2 group. During this process, the system reaches a **twisted-pyramid conical intersection** between the S_1 and S_0 ground state. This conical intersection allows for a rapid non-radiative pathway back to the ground state. Systems that contain a conical intersection between the ground and first excited state have posed significant challenges for single-reference excited state methods such as time-dependent density functional theory (TD-DFT) [335] and equation-of-motion coupled cluster theory [336, 337, 338].

In this study, we apply the SA-QDSRG method to investigate this nonradiative process in ethylene molecule by computing excitation energies of the twisted-pyramid conical intersection, as well as resolving the energetics along the pyramidalization coordinate.

This work demonstrates a rare example to resolve complex energetics of

a photodynamical process that involves near-degenerate states on near-term quantum processors.

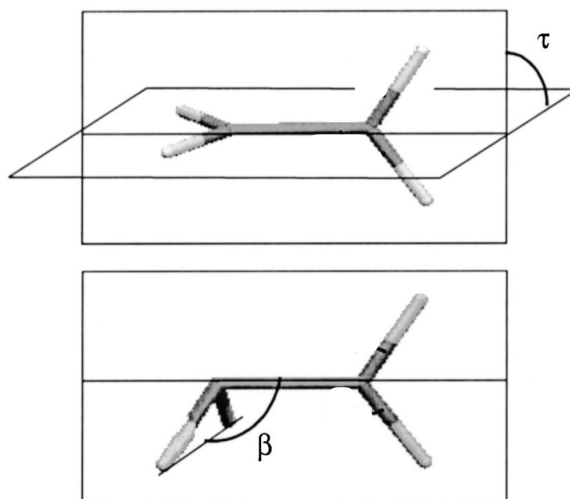


Figure 4.1: Definition of geometrical coordinates, torsion angle τ and pyramidalization angle β utilized in this study. The figure is adapted with permission from *J. Chem. Phys.*, 121(23):11614–11624, 2004, DOI:[10.1063/1.1807378](https://doi.org/10.1063/1.1807378). Copyright 2023 American Institute of Physics.

4.1 Methods

4.1.1 State-averaged Hamiltonian downfolding via QDSRG

The workflow of the state-averaged QDSRG downfolding scheme is nearly identical to that shown in Fig. 3.1, only differing in the preparation of the reference state.

The DSRG downfolding for ground states [242, 243, 244, 245, 255] starts from a single reference correlated state Ψ_0 , while in the state-averaged scheme [326], we use the density matrix ($\hat{\rho}$) for an ensemble of N correlated states,

$\mathbb{E}_0 \equiv \{|\Psi_0^\alpha\rangle, \alpha = 1, 2, \dots, N\}$. Each state in the ensemble is spanned by the same set of determinants $\{|\Phi_\mu\rangle\}$

$$|\Psi_0^\alpha\rangle = \sum_{\mu=1}^{N_{\text{CAS}}} c_i^\alpha |\Phi_\mu\rangle \quad (4.1)$$

where N_{CAS} is the total number of determinants in the active space.

Similar to the original QDSRG scheme, the state-averaged DSRG downfolding uses one unitary transformation $H \mapsto \bar{H} = e^{-A} H e^A$, but now this transformation decouples the ensemble of reference states $\{|\Psi_0^\alpha\rangle\}$ from their corresponding excited configurations in an averaged way. The DSRG effective Hamiltonian \bar{H}_{SA} is computed using equal-weighted averaged one- and two-body RDMs γ over N correlated states

$$\gamma_{xy\dots}^{uv\dots} = \frac{1}{N} \sum_{\alpha=1}^N [\gamma^\alpha]_{xy\dots}^{uv\dots} \quad (4.2)$$

Here, γ^α denotes the generic k -body RDMs of α -th reference state in the ensemble given by

$$[\gamma^\alpha]_{xy\dots}^{uv\dots} = \langle \Psi_0^\alpha | \hat{a}_u^\dagger \hat{a}_v^\dagger \dots \hat{a}_y \hat{a}_x | \Psi_0^\alpha \rangle \quad (4.3)$$

where the product $\hat{a}_u^\dagger \hat{a}_v^\dagger \dots \hat{a}_y \hat{a}_x$ contains k creation and k annihilation operators; we use indices u, v, w, x, y, z to label active spin orbitals partially occupied in each reference state.

The density cumulant approximations introduced in 1-QDSRG (Eq. 3.8) and 2-QDSRG (Eq. 3.9) are consistent with the previous treatments. The 3-body density cumulants are set to zero in all QDSRG treatments.

For the truncation level of the DSRG effective Hamiltonian, we consider

two treatments with increasing accuracy: (1) the perturbative truncation of multireference DSRG at second order [DSRG-PT2] [243]; (2) the nonperturbative linearized DSRG (LDSRG) with one- and two-body operators [LDSRG(2)] (shown in Eq. 3.4) as employed in the previous study. The details of obtaining DSRG-PT2 effective Hamiltonian can be found at Sec 2.6 of Ref. [245] or Ref. [243]. Here we employ two truncated effective Hamiltonians for the sake of the computational cost. The latter is crucial for determining the structure of the conical intersection in an economic way.

4.1.2 Quantum subspace expansion for excited states

The quantum subspace expansion (QSE) algorithm [91, 113, 137] obtains the electronic excited states with an additional measurement overhead upon the ground-state computations. Given an optimized ground state $|\Psi_0\rangle$, we expand the Hamiltonian in a subspace formed by $\{\hat{O}_J|\Psi_0\rangle\}$, where $\hat{O}_J \in \{\hat{a}_a^\dagger\hat{a}_i, \hat{a}_a^\dagger\hat{a}_b^\dagger\hat{a}_j\hat{a}_i\}$. Note that the subspace is truncated at double excitations that are sufficient for modeling the electronic states of ethylene. Since the basis is nonorthogonal, we solve a generalized eigenvalue problem $\mathbf{H}\mathbf{c} = \mathbf{S}\mathbf{c}E$ where elements of the overlap matrix (\mathbf{S}) and Hamiltonian (\mathbf{H}) are given by

$$S_{\alpha\beta} = \langle\Psi_0|\hat{O}_\alpha\hat{O}_\beta|\Psi_0\rangle, \quad H_{\alpha\beta} = \langle\Psi_0|\hat{O}_\alpha\hat{H}\hat{O}_\beta|\Psi_0\rangle \quad (4.4)$$

We further reduce the measurement cost of the QSE procedure by exploiting various symmetries of the system (particle number, total spin).

4.1.3 Spin-restricted ansatz

The process of ethylene photodynamics involving valence states can be well described by a multireference treatment employing an active space with two electrons in two orbitals [CAS(2,2)]. Fig. 4.2 shows two active molecular orbitals used for the twisted-pyramid conical intersection geometry.

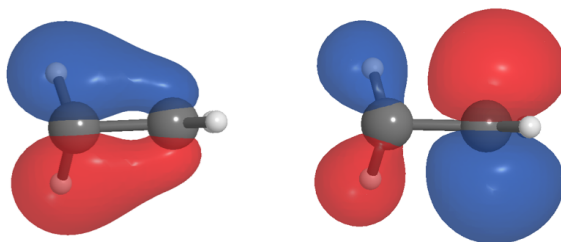


Figure 4.2: Two π -like molecular orbitals in the active space for the twisted-pyramid conical intersection geometry. The orbitals are optimized at the CASSCF(2,2)/aug-cc-pVTZ level of theory.

For the quantum simulations, we utilize a minimal spin-restricted circuit ansatz to encode the system which preserve the electron number, S_z and S^2 symmetries [339, 340] which only use two qubits, as shown in Fig. 4.3.

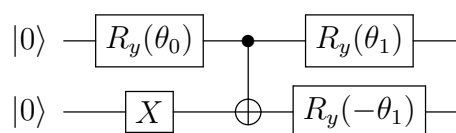


Figure 4.3: Circuit for singlet-restricted ansatz for a CAS(2,2) system

We use Jordan-Wigner encoding with a subsequent qubit tapering procedure that applies Z_2 symmetry reduction [167, 341, 342] to obtain the two-qubit Hamiltonian. The mapping between determinants and qubit computa-

tional basis states is given by

$$\begin{aligned}
 |\pi^2\rangle &\rightarrow |01\rangle \\
 |\pi^{*2}\rangle &\rightarrow |10\rangle \\
 |\pi^\uparrow\pi^{*\downarrow}\rangle &\rightarrow |11\rangle \\
 |\pi^\downarrow\pi^{*\uparrow}\rangle &\rightarrow |00\rangle.
 \end{aligned}
 \tag{4.5}$$

The wavefunction ansatz has the analytical expression as follows:

$$\begin{aligned}
 |\psi(\theta_0, \theta_1)\rangle &= \frac{1}{\sqrt{2}} \left[\sin\left(\frac{\theta_0}{2} + \frac{\pi}{4}\right) - \cos\left(\frac{\theta_0}{2} + \frac{\pi}{4}\right) \cos\theta_1 \right] |01\rangle \\
 &+ \frac{1}{\sqrt{2}} \left[\sin\left(\frac{\theta_0}{2} + \frac{\pi}{4}\right) + \cos\left(\frac{\theta_0}{2} + \frac{\pi}{4}\right) \cos\theta_1 \right] |10\rangle \\
 &+ \frac{1}{\sqrt{2}} \cos\left(\frac{\theta_0}{2} + \frac{\pi}{4}\right) \sin\theta_1 (|00\rangle + |11\rangle)
 \end{aligned}
 \tag{4.6}$$

4.2 Computational Details

The SA-QDSRG effective Hamiltonians are computed using Forte [272], an open-source plugin for the *ab initio* quantum chemistry package Psi4 [273]. All computations use CASSCF(2,2) orbitals optimized averaged over three lowest singlet states in the aug-cc-pVTZ basis [274, 343], with the density-fitting approximation of the two-electron integrals in the JKFIT basis set [344]. We freeze two 1s-like orbitals on carbon atoms in the DSRG correlation treatment. All DSRG computations use the flow parameter $s=2.0 E_h^{-2}$, based on the previous study [345]. We take the geometry of the twisted-pyramid conical intersection from Ref. [345], which was optimized via the gradient projection method [346] at the SA-DSRG-PT2/aug-cc-pVTZ level of theory with

the flow parameter value $s = 2.0 E_h^{-2}$ and CASSCF(2,2) orbitals optimized averaged over three lowest singlet states.

4.3 Results and Discussion

We first show results of noiseless simulations. We compute the excitation energies of the three low-lying singlet states of the twisted-pyramid conical intersection geometry at the SA-DSRG-PT2, 1(2)-SA-QDSRG-PT2, SA-LDSRG(2) and 1(2)-SA-QLDSRG(2) levels, as reported in Table 4.1. We also include values from other methods for comparison, including MRCI with singles and doubles (MRCISD) [287, 288], MRCISD with Davidson’s correction (MRCISD+Q) [289]. For this system, the impact of density cumulant approximations introduced in the QDSRG is negligible for excited-state calculations, because we observe very small deviations (0.0–0.3 eV) of the SA-QDSRG results from the SA-DSRG ones. We can see that the state-averaged DSRG and QDSRG formalism are well capable of describing degenerate states, since the energy differences between 2^1A and 1^1A states are generally small, within 0.01–0.04 eV, which slightly outperform MRCISD+Q result, while MRCISD is better at capturing the degeneracy of 2^1A and 1^1A states.

In Fig. 4.4, we show potential energy curves of the three lowest singlet states along the pyramidalization motion of one CH_2 group obtained with the bare Hamiltonian (Figure 4.4c) and the QDSRG downfolded Hamiltonians (SA-DSRG-PT2 and 2-SA-QDSRG-PT2 in Figure 4.4a, SA-LDSRG(2) and 2-SA-QLDSRG(2) in Figure 4.4b). For each method, all energies are shifted to ensure that the energy of the ground state at the planar geometry is zero. Dy-

dynamic correlation beyond the active space is crucial for accurately describing the energetics in the vicinity of the conical intersection, since diagonalizing the bare Hamiltonian within the active space alone does not yield the distinctive “double-cone” shape in the near-degenerate region. In contrast, all QDSRG downfolded Hamiltonians correctly capture the "double-cone" shape that characterizes the conical intersection. We note that the exact geometry of the conical intersection is dependent on the level of theory employed in computations. As seen in Figure 4.4, SA-DSRG-PT2 and 2-SA-QDSRG-PT2 give a pyramidalization angle of 106° at the conical intersection geometry, while SA-LDSRG(2) and 2-SA-QLDSRG(2) predict an angle of 98° . The inclusion of more dynamic correlation moves the location of the conical intersection to a smaller pyramidalization angle.

Table 4.1: Excitation energies (in eV) of the three lowest singlet states of the twisted-pyramid conical intersection geometry. The excitation energies are computed with respect to the ground-state energy of the planar geometry (Franck-Condon point) calculated at the corresponding computational level.

Method	$1\ ^1A$	$2\ ^1A$	$3\ ^1A$
SA-DSRG-PT2(eig. \bar{H}_{pt2})	4.11	4.12	8.55
2-SA-QDSRG-PT2	4.10	4.12	8.55
1-SA-QDSRG-PT2	4.09	4.12	8.56
SA-LDSRG(2)(eig. $\bar{H}_{1,2}$)	4.87	4.90	9.96
2-SA-QLDSRG(2)	4.87	4.90	9.96
1-SA-QLDSRG(2)	4.86	4.90	9.99
MRCISD ^a	4.83	4.83	9.83
MRCISD+Q ^a	4.50	4.54	9.26

^a From Ref. [329].

4.4 Summary and future work

This chapter summarizes the results from noiseless SA-QDSRG computations of the twisted-pyramid conical intersection on the ethylene excited-state energy surfaces and the energetics of the relevant nonradiative process. As of the completion of this dissertation, ongoing efforts are being made to obtain satisfactory results from experiments on quantum devices. There are several aspects worth exploring for the device computations

- the sensitivity of SA-QDSRG energies with respect to the stochastic noises (finite measurement errors) in the reference RDMs;
- how various error mitigation techniques may improve upon the raw data since we have a CNOT gate in the ansatz. We always perform readout-error mitigation [347] since it is quite standardized in the workflow. Other typical error mitigation methods include zero-noise extrapolation [38] with linear [348] or exponential function form [37], probabilistic error cancellation [36, 37, 349].

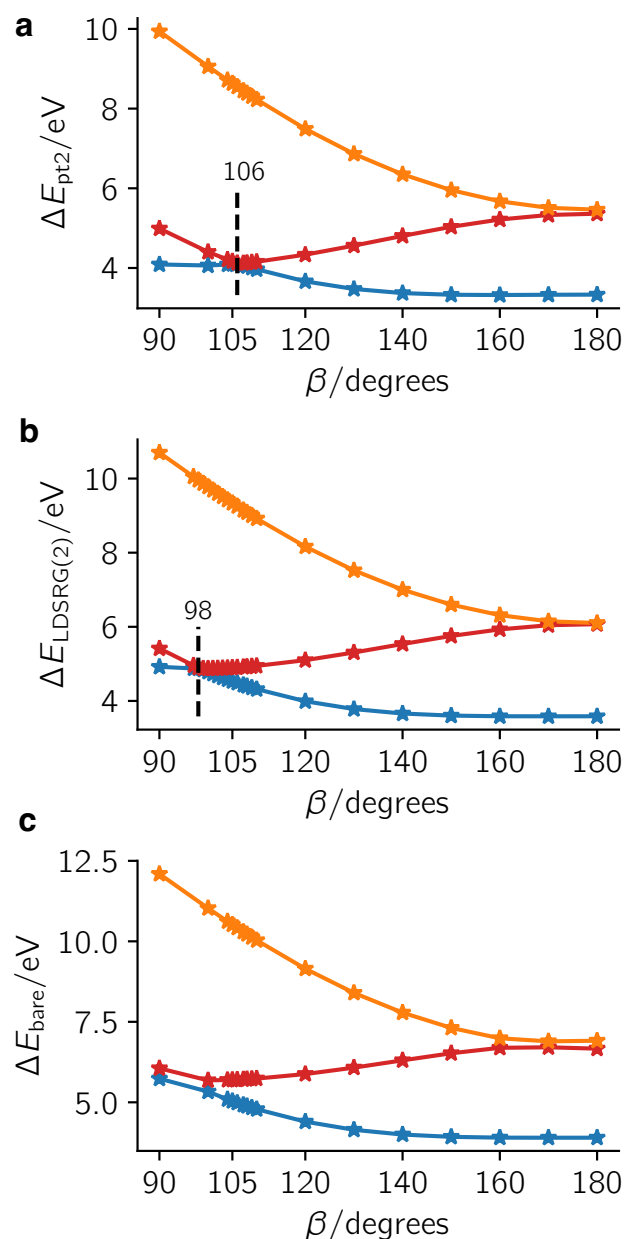


Figure 4.4: Potential energy curves of the three lowest singlet states along the pyramidalization motion of one CH_2 group computed with (a) SA-DSRG-PT2 [solid lines] and 2-SA-QDSRG-PT2 [asterisks], (b) SA-LDSRG(2) [solid lines], 2-SA-QLDSRG(2) [asterisks], (c) diagonalizing the bare Hamiltonian. Energies are shifted with respect to the ground-state energy of the planar geometry calculated using the same method. The vertical dash lines and angle values denote the twisted-pyramid conical intersection geometry at the corresponding computational level.

Chapter 5

Conclusions and perspectives

In this dissertation, we have shown that quantum simulations of many-body problems are practical applications of quantum computers.

In Chapter 2, we introduced a novel quantum algorithm, termed the multireference selected quantum Krylov (MRSQK) method that combines a compact quantum Krylov subspace, unitary real-time evolution, and multi-reference strategy to facilitate a numerically-robust treatment of strongly-correlated systems. Benchmarks on various systems demonstrate the feasibility of MRSQK to use compact Krylov bases for predicting ground state energies. MRSQK provides a natural extension to compute excited states. An open problem is how to select a good reference space for the target excited state.

Achieving realistic chemical simulations on current small, noisy quantum devices involves addressing two key challenges. Firstly, many quantum algorithms for chemistry are solely tested in classical exact emulations, neglecting intrinsic errors that occur in real quantum hardware, such as finite measure-

ment errors and device noise. This limitation hinders the accurate representation of quantum behavior on the actual hardware. Secondly, performing realistic chemical applications requires large one-electron orbital basis sets, which is resource-intensive due to the linear scaling of qubits with the number of correlated molecular orbitals. To overcome these obstacles, we propose a practical solution in Chapter 3 - a quantum unitary downfolding formalism based on the driven similarity renormalization group (QDSRG), which optimizes the quantum resource and enables more accurate and efficient chemical simulations on noisy quantum devices. The QDSRG is a polynomial-scaling downfolding method that retains the accuracy of classical multireference many-body theories while avoiding the evaluation of expensive higher-order reduced density matrices. This method effectively reduces the dimensionality of the problem and minimizes the required quantum resources, which enables resource-efficient simulations on small-scale quantum computers using large computational basis sets. We model the bicyclobutane isomerization pathways to *trans*-butadiene on IBM quantum devices, demonstrating the viability of QDSRG to leverage near-term quantum devices for estimating molecular properties with chemical accuracy.

In Chapter 4, we extend the QDSRG downfolding method to a state-averaged formalism (SA-QDSRG) that is capable of treating near-degenerate states which pose great challenges for many quantum chemical methods. We have shown results from noiseless SA-QDSRG computations of the twisted-pyramid conical intersection on the ethylene excited-state energy surfaces and the energetics of the relevant nonradiative process.

We believe that the QDSRG downfolding scheme provides a robust and el-

egant framework to simulate complex chemical processes with limited quantum resources, demonstrating practical applications of near-term small quantum devices. With the continuous advancements in quantum hardware and the increasing availability of qubits, we hope this general Hamiltonian unitary downfolding scheme based on DSRG could enable rapid and precise simulations of large systems with industry relevance that could potentially achieve a real quantum advantage over classical computing.

Bibliography

- [1] Richard P. Feynman. Simulating Physics with Computers. *Int. J. Theor. Phys.*, 21:467–488, 1982.
- [2] Richard P Feynman. Quantum mechanical computers. *Found. Phys.*, 16:507–531, 1986.
- [3] Yuri I Manin. Computable and uncomputable [in Russian]. *Sovetskoye Radio, Moscow*, 1980; see *Mathematics as Metaphor: Selected Essays of Yuri I. Manin* (American Mathematical Society, Providence, 2007), pp. 77–78 for an English translation.
- [4] R B Laughlin and D Pines. The theory of everything. *Proc. Natl. Acad. Sci. U.S.A.*, 97(1):28–31, January 2000.
- [5] Norbert Schuch and Frank Verstraete. Computational complexity of interacting electrons and fundamental limitations of density functional theory. *Nat. Phys.*, 5(10):732, 2009.
- [6] I M Georgescu, S Ashhab, and Franco Nori. Quantum simulation. *Rev. Mod. Phys.*, 86(1):153–185, March 2014.

- [7] Ehud Altman, Kenneth R. Brown, Giuseppe Carleo, Lincoln D. Carr, Eugene Demler, Cheng Chin, Brian DeMarco, Sophia E. Economou, Mark A. Eriksson, Kai-Mei C. Fu, Markus Greiner, Kaden R.A. Hazard, Randall G. Hulet, Alicia J. Kollár, Benjamin L. Lev, Mikhail D. Lukin, Ruichao Ma, Xiao Mi, Shashank Misra, Christopher Monroe, Kater Murch, Zaira Nazario, Kang-Kuen Ni, Andrew C. Potter, Pedram Roushan, Mark Saffman, Monika Schleier-Smith, Irfan Siddiqi, Raymond Simmonds, Meenakshi Singh, I.B. Spielman, Kristan Temme, David S. Weiss, Jelena Vučković, Vladan Vuletić, Jun Ye, and Martin Zwierlein. Quantum simulators: Architectures and opportunities. *PRX Quantum*, 2:017003, Feb 2021.
- [8] Yuri Alexeev, Dave Bacon, Kenneth R. Brown, Robert Calderbank, Lincoln D. Carr, Frederic T. Chong, Brian DeMarco, Dirk Englund, Edward Farhi, Bill Fefferman, Alexey V. Gorshkov, Andrew Houck, Jungsang Kim, Shelby Kimmel, Michael Lange, Seth Lloyd, Mikhail D. Lukin, Dmitri Maslov, Peter Maunz, Christopher Monroe, John Preskill, Martin Roetteler, Martin J. Savage, and Jeff Thompson. Quantum computer systems for scientific discovery. *PRX Quantum*, 2:017001, Feb 2021.
- [9] Torsten Hoefler, Thomas Häner, and Matthias Troyer. Disentangling hype from practicality: on realistically achieving quantum advantage. *Commun. ACM*, 66(5):82–87, 2023.
- [10] Aram W Harrow, Avinandan Hassidim, and Seth Lloyd. Quantum algorithm for linear systems of equations. *Phys. Rev. Lett.*, 103(15):150502, 2009.

- [11] Lov K Grover. Quantum mechanics helps in searching for a needle in a haystack. *Phys. Rev. Lett.*, 79(2):325, 1997.
- [12] Lov K Grover. A fast quantum mechanical algorithm for database search. In *Proceedings of the 28th Annual ACM Symp. Theory of Computing*, pages 212–219, 1996.
- [13] Ryan Babbush, Jarrod R McClean, Michael Newman, Craig Gidney, Sergio Boixo, and Hartmut Neven. Focus beyond quadratic speedups for error-corrected quantum advantage. *PRX Quantum*, 2(1):010103, 2021.
- [14] Carlos Outeiral, Martin Strahm, Jiye Shi, Garrett M Morris, Simon C Benjamin, and Charlotte M Deane. The prospects of quantum computing in computational molecular biology. *WIREs Comput Mol Sci*, 11(1):e1481, 2021.
- [15] Markus Reiher, Nathan Wiebe, Krysta M Svore, Dave Wecker, and Matthias Troyer. Elucidating reaction mechanisms on quantum computers. *Proc. Natl. Acad. Sci. U.S.A.*, 114(29):7555–7560, 2017.
- [16] Sabre Kais. Introduction to Quantum Information and Computation for Chemistry. In Sabre Kais, editor, *Quantum Information and Computation for Chemistry*, Advances in Chemical Physics, chapter 1, pages 1–38. Wiley Online Library, 2014.
- [17] Javier Argüello-Luengo, Alejandro González-Tudela, Tao Shi, Peter Zoller, and J Ignacio Cirac. Analogue quantum chemistry simulation. *Nature*, 574(7777):215–218, October 2019.

- [18] Toby S Cubitt, Ashley Montanaro, and Stephen Piddock. Universal quantum hamiltonians. *Proc. Natl. Acad. Sci. U.S.A.*, 115(38):9497–9502, 2018.
- [19] E Torrontegui, A Ruschhaupt, David Guéry-Odelin, and JG Muga. Simulation of quantum collinear chemical reactions with ultracold atoms. *J. Phys. B: At. Mol. Opt. Phys.*, 44(19):195302, 2011.
- [20] A Yu Smirnov, S Savel'ev, LG Mourokh, and Franco Nori. Modelling chemical reactions using semiconductor quantum dots. *EPL*, 80(6):67008, 2007.
- [21] Joonsuk Huh, Gian Giacomo Guerreschi, Borja Peropadre, Jarrod R McClean, and Alán Aspuru-Guzik. Boson sampling for molecular vibronic spectra. *Nat. Photonics*, 9(9):615–620, 2015.
- [22] Joonsuk Huh and Man-Hong Yung. Vibronic boson sampling: generalized Gaussian boson sampling for molecular vibronic spectra at finite temperature. *Sci. Rep.*, 7(1):7462, 2017.
- [23] Seungbeom Chin and Joonsuk Huh. Quantum computing for molecular vibronic spectra and Gaussian boson sampling. In *J. Phys.: Conf. Ser.*, volume 1071, page 012009. IOP Publishing, 2018.
- [24] William R Clements, Jelmer J Renema, Andreas Eckstein, Antonio A Valido, Adriana Lita, Thomas Gerrits, Sae Woo Nam, W Steven Kolthammer, Joonsuk Huh, and Ian A Walmsley. Approximating vibronic spectroscopy with imperfect quantum optics. *J. Phys. B: At. Mol. Opt. Phys.*, 51(24):245503, 2018.

- [25] Chris Sparrow, Enrique Martín-López, Nicola Maraviglia, Alex Neville, Christopher Harrold, Jacques Carolan, Yogesh N Joglekar, Toshikazu Hashimoto, Nobuyuki Matsuda, Jeremy L O'Brien, et al. Simulating the vibrational quantum dynamics of molecules using photonics. *Nature*, 557(7707):660–667, 2018.
- [26] Yangchao Shen, Yao Lu, Kuan Zhang, Junhua Zhang, Shuaining Zhang, Joonsuk Huh, and Kihwan Kim. Quantum optical emulation of molecular vibronic spectroscopy using a trapped-ion device. *Chem. Sci.*, 9(4):836–840, 2018.
- [27] Da-Wei Luo, Michele Modugno, Mike Guidry, JQ You, and Lian-Ao Wu. Quantum simulation of electron Coulomb interactions. *EPL*, 130(1):10001, 2020.
- [28] Debadrita Saha, Srinivasan S Iyengar, Philip Richerme, Jeremy M Smith, and Amr Sabry. Mapping quantum chemical dynamics problems to spin-lattice simulators. *J. Chem. Theory Comput.*, 17(11):6713–6732, 2021.
- [29] Ling Hu, Yue-Chi Ma, Yuan Xu, Wei-Ting Wang, Yu-Wei Ma, Ke Liu, Hai-Yan Wang, Yi-Pu Song, Man-Hong Yung, and Lu-Yan Sun. Simulation of molecular spectroscopy with circuit quantum electrodynamics. *Sci. Bulletin*, 63(5):293–299, 2018.
- [30] Markus Greiner, Olaf Mandel, Tilman Esslinger, Theodor W Hänsch, and Immanuel Bloch. Quantum phase transition from a superfluid to

- a mott insulator in a gas of ultracold atoms. *Nature*, 415(6867):39, 2002.
- [31] Hannes Bernien, Sylvain Schwartz, Alexander Keesling, Harry Levine, Ahmed Omran, Hannes Pichler, Soonwon Choi, Alexander S Zibrov, Manuel Endres, Markus Greiner, et al. Probing many-body dynamics on a 51-atom quantum simulator. *Nature*, 551(7682):579, 2017.
- [32] Jiehang Zhang, Guido Pagano, Paul W Hess, Antonis Kyprianidis, Patrick Becker, Harvey Kaplan, Alexey V Gorshkov, Z-X Gong, and Christopher Monroe. Observation of a many-body dynamical phase transition with a 53-qubit quantum simulator. *Nature*, 551(7682):601–604, 2017.
- [33] Daniel González-Cuadra, Dolev Bluvstein, Marcin Kalinowski, Raphael Kaubruegger, Nishad Maskara, Piero Naldesi, Torsten V Zache, Adam M Kaufman, Mikhail D Lukin, Hannes Pichler, et al. Fermionic quantum processing with programmable neutral atom arrays. *arXiv preprint arXiv:2303.06985*, 2023.
- [34] Austin G Fowler, Matteo Mariantoni, John M Martinis, and Andrew N Cleland. Surface codes: Towards practical large-scale quantum computation. *Phys. Rev. A*, 86:032324, September 2012.
- [35] Sagar Vijay, Timothy H Hsieh, and Liang Fu. Majorana fermion surface code for universal quantum computation. *Phys. Rev. X*, 5:041038, December 2015.

- [36] Kristan Temme, Sergey Bravyi, and Jay M Gambetta. Error Mitigation for Short-Depth Quantum Circuits. *Phys. Rev. Lett.*, 119(18):180509, 2017.
- [37] Suguru Endo, Simon C. Benjamin, and Ying Li. Practical quantum error mitigation for near-future applications. *Phys. Rev. X*, 8:031027, Jul 2018.
- [38] Abhinav Kandala, Kristan Temme, Antonio D Córcoles, Antonio Mezzacapo, Jerry M Chow, and Jay M Gambetta. Error mitigation extends the computational reach of a noisy quantum processor. *Nature*, 567:491–495, March 2019.
- [39] Andrew M Childs and Wim Van Dam. Quantum algorithms for algebraic problems. *Rev. Mod. Phys.*, 82(1):1–52, 2010.
- [40] Trygve Helgaker, Poul Jorgensen, and Jeppe Olsen. *Molecular electronic-structure theory*. John Wiley & Sons, Chichester, England, 2014.
- [41] Attila Szabo and Neil S Ostlund. *Modern quantum chemistry: Introduction to advanced electronic structure theory*. Dover Publications, Mineola, NY, 1996.
- [42] Francesco A Evangelista. Notes on electronic structure theory. <https://github.com/fevangelista/CHEM532-ElectronicStructure-Notes>, 2022.

- [43] C. Roothaan. Self-consistent field theory for open shells of electronic systems. *Rev. Mod. Phys.*, 32(2):179, 1960.
- [44] Daniel KW Mok, Ralf Neumann, and Nicholas C Handy. Dynamical and nondynamical correlation. *J. Phys. Chem.*, 100(15):6225–6230, 1996.
- [45] Daniel Roca-Sanjuán, Francesco Aquilante, and Roland Lindh. Multiconfiguration second-order perturbation theory approach to strong electron correlation in chemistry and photochemistry. *Wiley Interdiscip. Rev. Comput. Mol. Sci.*, 2(4):585–603, 2012.
- [46] Ivan Kassal, Stephen P Jordan, Peter J Love, Masoud Mohseni, and Alán Aspuru-Guzik. Polynomial-time quantum algorithm for the simulation of chemical dynamics. *Proc. Natl. Acad. Sci. U.S.A.*, 105(48):18681–18686, 2008.
- [47] Pawel Wocjan and Shengyu Zhang. Several natural BQP-complete problems. *arXiv e-prints*, pages arXiv:quant-ph/0606179, 2006.
- [48] James D Whitfield, Man-Hong Yung, David Gabriel Tempel, S Boixo, and Alan Aspuru-Guzik. Computational complexity of time-dependent density functional theory. *New J. Phys.*, 16(8):083035, 2014.
- [49] Benjamin Schumacher. Quantum coding. *Phys. Rev. A*, 51(4):2738, 1995.
- [50] Michael A Nielsen and Isaac L Chuang. *Quantum Computation and Quantum Information*. Cambridge University Press, New York, NY, 2010.

- [51] Eleanor G Rieffel and Wolfgang H Polak. *Quantum computing: a gentle introduction*. MIT Press, Cambridge, Massachusetts, 2011.
- [52] John Preskill. Quantum Computing in the NISQ era and beyond. *Quantum*, 2:79, 2018.
- [53] Pascual Jordan and Eugene Paul Wigner. über das paulische äquivalenzverbot. In *The Collected Works of Eugene Paul Wigner*, pages 109–129. Springer, 1993.
- [54] Jacob T Seeley, Martin J Richard, and Peter J Love. The Bravyi-Kitaev transformation for quantum computation of electronic structure. *J. Chem. Phys.*, 137(22):224109, December 2012.
- [55] Sergey B Bravyi and Alexei Yu Kitaev. Fermionic Quantum Computation. *Ann. of Phys.*, 298(1):210–226, 2002.
- [56] Alán Aspuru-Guzik, Anthony D Dutoi, Peter J Love, and Martin Head-Gordon. Simulated quantum computation of molecular energies. *Science*, 309:1704–1707, September 2005.
- [57] Alberto Peruzzo, Jarrod McClean, Peter Shadbolt, Man-Hong Yung, Xiao-Qi Zhou, Peter J Love, Alán Aspuru-Guzik, and Jeremy L O’Brien. A variational eigenvalue solver on a photonic quantum processor. *Nat. Commun.*, 5(1):4213, July 2014.
- [58] Man-Hong Yung, J Casanova, L Lamata, E Solano, Alán Aspuru-Guzik, Jarrod R McClean, and Antonio Mezzacapo. From transistor to trapped-ion computers for quantum chemistry. *Sci. Rep.*, 4:3589, 2014.

- [59] Jarrod R McClean, Jonathan Romero, Ryan Babbush, and Alán Aspuru-Guzik. The theory of variational hybrid quantum-classical algorithms. *New J. Phys.*, 18:023023, 2016.
- [60] Ryan Babbush, Jarrod McClean, Dave Wecker, Alán Aspuru-Guzik, and Nathan Wiebe. Chemical basis of Trotter-Suzuki errors in quantum chemistry simulation. *Phys. Rev. A*, 91(2):106–16, February 2015.
- [61] Pierre-Luc Dallaire-Demers, Jonathan Romero, Libor Veis, Sukin Sim, and Alán Aspuru-Guzik. Low-depth circuit ansatz for preparing correlated fermionic states on a quantum computer. *Quantum Sci. Technol.*, 4(4):045005–18, October 2019.
- [62] Norm M Tubman, Carlos Mejuto-Zaera, Jeffrey M Epstein, Diptarka Hait, Daniel S Levine, William Huggins, Zhang Jiang, Jarrod R McClean, Ryan Babbush, Martin Head-Gordon, and K Birgitta Whaley. Postponing the orthogonality catastrophe: efficient state preparation for electronic structure simulations on quantum devices. *arXiv preprint arXiv:1809.05523 [quant-ph]*, 2018.
- [63] Kenji Sugisaki, Satoru Yamamoto, Shigeaki Nakazawa, Kazuo Toyota, Kazunobu Sato, Daisuke Shiomi, and Takeji Takui. Quantum Chemistry on Quantum Computers: A Polynomial-Time Quantum Algorithm for Constructing the Wave Functions of Open-Shell Molecules. *J. Phys. Chem. A*, 120(32):6459–6466, August 2016.
- [64] Kenji Sugisaki, Satoru Yamamoto, Shigeaki Nakazawa, Kazuo Toyota, Kazunobu Sato, Daisuke Shiomi, and Takeji Takui. Open shell elec-

tronic state calculations on quantum computers: A quantum circuit for the preparation of configuration state functions based on Serber construction. *Chem. Phys. Lett.: X*, 737:100002, January 2019.

- [65] Hefeng Wang, Sabre Kais, Alán Aspuru-Guzik, and Mark R Hoffmann. Quantum algorithm for obtaining the energy spectrum of molecular systems. *Phys. Chem. Chem. Phys.*, 10(35):5388–5393, 2008.
- [66] Roger Fletcher. *Practical methods of optimization*. John Wiley & Sons, Chichester, England, 1987.
- [67] Mario Motta, Chong Sun, Adrian T. K. Tan, Matthew J O'Rourke, Erika Ye, Austin J Minnich, Fernando G S L Brandao, and Garnet Kin-Lic Chan. Determining eigenstates and thermal states on a quantum computer using quantum imaginary time evolution. *Nat. Phys.*, 16:205–210, November 2019.
- [68] Gian-Carlo Wick. Properties of bethe-salpeter wave functions. *Phys. Rev.*, 96(4):1124, 1954.
- [69] Lauri Lehtovaara, Jari Toivanen, and Jussi Eloranta. Solution of time-independent schrödinger equation by the imaginary time propagation method. *J. Comput. Phys.*, 221(1):148–157, 2007.
- [70] Matthew J S Beach, Roger G Melko, Tarun Grover, and Timothy H Hsieh. Making trotters sprint: A variational imaginary time ansatz for quantum many-body systems. *Phys. Rev. B*, 100(9):094434, September 2019.

- [71] Shi-Ning Sun, Mario Motta, Ruslan N Tazhigulov, Adrian T. K. Tan, Garnet Kin-Lic Chan, and Austin J Minnich. Quantum Computation of Finite-Temperature Static and Dynamical Properties of Spin Systems Using Quantum Imaginary Time Evolution. *PRX Quantum*, 2(1):010317, February 2021.
- [72] Hirsh Kamakari, Shi-Ning Sun, Mario Motta, and Austin J Minnich. Digital quantum simulation of open quantum systems using quantum imaginary-time evolution. *PRX Quantum*, 3(1):010320, 2022.
- [73] Jinfeng Zeng, Chenfeng Cao, Chao Zhang, Pengxiang Xu, and Bei Zeng. A variational quantum algorithm for Hamiltonian diagonalization. *Quantum Sci. Technol.*, 6(4):045009, July 2021.
- [74] Raja Selvarajan, Vivek Dixit, Xingshan Cui, Travis S Humble, and Sabre Kais. Prime factorization using quantum variational imaginary time evolution. *Sci. Rep.*, 11(1):1–8, 2021.
- [75] Kübra Yeter-Aydeniz, Eleftherios Moschandreou, and George Siopsis. Quantum imaginary-time evolution algorithm for quantum field theories with continuous variables. *Phys. Rev. A*, 105(1):012412, 2022.
- [76] Niladri Gomes, Feng Zhang, Noah F Berthusen, Cai-Zhuang Wang, Kai-Ming Ho, Peter P Orth, and Yongxin Yao. Efficient Step-Merged Quantum Imaginary Time Evolution Algorithm for Quantum Chemistry. *J. Chem. Theory Comput.*, 16(10):6256–6266, September 2020.
- [77] Kübra Yeter-Aydeniz, Raphael C Pooser, and George Siopsis. Practical quantum computation of chemical and nuclear energy levels using

- quantum imaginary time evolution and Lanczos algorithms. *npj Quantum Inf.*, 6(1):63, July 2020.
- [78] Hirofumi Nishi, Taichi Kosugi, and Yu-ichiro Matsushita. Implementation of quantum imaginary-time evolution method on NISQ devices by introducing nonlocal approximation. *npj Quantum Inf.*, 7:85, June 2021.
- [79] Jean-Loup Ville, Alexis Morvan, Akel Hashim, Ravi K Naik, Marie Lu, Bradley Mitchell, John-Mark Kreikebaum, Kevin P O'Brien, Joel J Wallman, Ian Hincks, et al. Leveraging randomized compiling for the quantum imaginary-time-evolution algorithm. *Phys. Rev. Research*, 4(3):033140, 2022.
- [80] Sam McArdle, Tyson Jones, Suguru Endo, Ying Li, Simon C Benjamin, and Xiao Yuan. Variational ansatz-based quantum simulation of Imaginary Time Evolution. *npj Quantum Inf.*, 5(1):1–6, September 2019.
- [81] Suguru Endo, Tyson Jones, Sam McArdle, Xiao Yuan, and Simon C Benjamin. Variational quantum algorithms for discovering Hamiltonian spectra. *Phys. Rev. A*, 99:062304, June 2019.
- [82] Niladri Gomes, Anirban Mukherjee, Feng Zhang, Thomas Iadecola, Cai-Zhuang Wang, Kai-Ming Ho, Peter P Orth, and Yong-Xin Yao. Adaptive Variational Quantum Imaginary Time Evolution Approach for Ground State Preparation. *Adv. Quantum Technol.*, page 2100114, 2021.
- [83] Frank Arute, Kunal Arya, Ryan Babbush, Dave Bacon, Joseph C Bardin, Rami Barends, Rupak Biswas, Sergio Boixo, Fernando G S L Brandao,

- David A Buell, et al. Quantum supremacy using a programmable superconducting processor. *Nature*, 574(7779):505–510, October 2019.
- [84] Yudong Cao, Jonathan Romero, Jonathan P Olson, Matthias Degroote, Peter D Johnson, Mária Kieferová, Ian D Kivlichan, Tim Menke, Borja Peropadre, Nicolas P D Sawaya, Sukin Sim, Libor Veis, and Alán Aspuru-Guzik. Quantum Chemistry in the Age of Quantum Computing. *Chem. Rev.*, 119(19):10856–10915, October 2019.
- [85] Daniel S Abrams and Seth Lloyd. Simulation of Many-Body Fermi Systems on a Universal Quantum Computer. *Phys. Rev. Lett.*, 79(13):2586–2589, September 1997.
- [86] Daniel S Abrams and Seth Lloyd. Quantum algorithm providing exponential speed increase for finding eigenvalues and eigenvectors. *Phys. Rev. Lett.*, 83(24):5162–5165, 1999.
- [87] G Ortiz, J E Gubernatis, E Knill, and R Laflamme. Quantum algorithms for fermionic simulations. *Phys. Rev. A*, 64(2):022319, July 2001.
- [88] Pedro MQ Cruz, Gonçalo Catarina, Ronan Gautier, and Joaquín Fernández-Rossier. Optimizing quantum phase estimation for the simulation of hamiltonian eigenstates. *Quantum Sci. Technol.*, 5(4):044005, 2020.
- [89] B P Lanyon, J D Whitfield, G G Gillett, M E Goggin, M P Almeida, I Kassal, J D Biamonte, M Mohseni, B J Powell, M Barbieri, A Aspuru-Guzik, and A G White. Towards quantum chemistry on a quantum computer. *Nat. Chem.*, 2(2):106–111, 2010.

- [90] Edward Farhi, Jeffrey Goldstone, and Sam Gutmann. A Quantum Approximate Optimization Algorithm. *arXiv e-prints*, pages arXiv:1411.4028 [quant-ph], November 2014.
- [91] Jarrod R McClean, Mollie E Kimchi-Schwartz, Jonathan Carter, and Wibe A de Jong. Hybrid quantum-classical hierarchy for mitigation of decoherence and determination of excited states. *Phys. Rev. A*, 95(4):042308–10, 2017.
- [92] Sam McArdle, Suguru Endo, Alán Aspuru-Guzik, Simon C Benjamin, and Xiao Yuan. Quantum computational chemistry. *Rev. Mod. Phys.*, 92(1):015003, March 2020.
- [93] P J J O’Malley, Jonathan Romero, R Barends, J Kelly, P Roushan, A Tranter, N Ding, B Campbell, Y Chen, Z Chen, B Chiaro, A Dunsworth, A G Fowler, E Jeffrey, A Megrant, J Y Mutus, C Neill, C Quintana, D Sank, A Vainsencher, J Wenner, T C White, P V Coveney, J M Martinis, Alán Aspuru-Guzik, Ryan Babbush, Ian D Kivlichan, Peter J Love, Jarrod R McClean, and Hartmut Neven. Scalable Quantum Simulation of Molecular Energies. *Phys. Rev. X*, 6:031007, 2016.
- [94] Panagiotis Kl Barkoutsos, Jerome F Gonthier, Igor Sokolov, Nikolaj Moll, Gian Salis, Andreas Fuhrer, Marc Ganzhorn, Daniel J Egger, Matthias Troyer, Antonio Mezzacapo, Stefan Filipp, and Ivano Tavernelli. Quantum algorithms for electronic structure calculations: Particle-hole Hamiltonian and optimized wave-function expansions. *Phys. Rev. A*, 98(2):022322, August 2018.

- [95] Jonathan Romero, Ryan Babbush, Jarrod R McClean, Cornelius Hempel, Peter J Love, and Alán Aspuru-Guzik. Strategies for quantum computing molecular energies using the unitary coupled cluster ansatz. *Quantum Sci. Technol.*, 4(1):014008–23, January 2019.
- [96] Rodney J Bartlett, Stanislaw A Kucharski, and Jozef Noga. Alternative coupled-cluster ansätze ii. the unitary coupled-cluster method. *Chem. Phys. Lett.*, 155(1):133–140, 1989.
- [97] Werner Kutzelnigg. Error analysis and improvements of coupled-cluster theory. *Theor. Chim. Acta*, 80(4-5):349–386, 1991.
- [98] Péter G Szalay, Marcel Nooijen, and Rodney J Bartlett. Alternative Ansatz in Single Reference Coupled-Cluster Theory .III. A Critical Analysis of Different Methods. *J. Chem. Phys.*, 103(1):281–298, July 1995.
- [99] Andrew G Taube and Rodney J Bartlett. New perspectives on unitary coupled-cluster theory. *Int. J. Quantum Chem.*, 106(15):3393–3401, January 2006.
- [100] Bridgette Cooper and Peter J Knowles. Benchmark studies of variational, unitary and extended coupled cluster methods. *J. Chem. Phys.*, 133(23):234102, 2010.
- [101] Francesco A Evangelista and Jürgen Gauss. An orbital-invariant internally contracted multireference coupled cluster approach. *J. Chem. Phys.*, 134(11):114102, March 2011.

- [102] Gaurav Harsha, Toru Shiozaki, and Gustavo E Scuseria. On the difference between variational and unitary coupled cluster theories. *J. Chem. Phys.*, 148(4):044107, January 2018.
- [103] Joonho Lee, William J Huggins, Martin Head-Gordon, and K Birgitta Whaley. Generalized Unitary Coupled Cluster Wave functions for Quantum Computation. *J. Chem. Theory Comput.*, 15(1):311–324, 2019.
- [104] Ilya G Ryabinkin, Tzu-Ching Yen, Scott N Genin, and Artur F Izmaylov. Qubit Coupled Cluster Method: A Systematic Approach to Quantum Chemistry on a Quantum Computer. *J. Chem. Theory Comput.*, 14(12):6317–6326, November 2018.
- [105] Ilya G Ryabinkin, Robert A Lang, Scott N Genin, and Artur F Izmaylov. Iterative Qubit Coupled Cluster Approach with Efficient Screening of Generators. *J. Chem. Theory Comput.*, 16(2):1055–1063, February 2020.
- [106] Ilya G Ryabinkin, Scott N Genin, and Artur F Izmaylov. Constrained Variational Quantum Eigensolver: Quantum Computer Search Engine in the Fock Space. *J. Chem. Theory Comput.*, 15(1):249–255, January 2019.
- [107] Harper R Grimsley, Sophia E Economou, Edwin Barnes, and Nicholas J Mayhall. An adaptive variational algorithm for exact molecular simulations on a quantum computer. *Nat. Commun.*, 10(1):3007, 2019.
- [108] Ho Lun Tang, V.O. Shkolnikov, George S Barron, Harper R Grimsley, Nicholas J Mayhall, Edwin Barnes, and Sophia E Economou.

Qubit-ADAPT-VQE: An Adaptive Algorithm for Constructing Hardware-Efficient Ansätze on a Quantum Processor. *PRX Quantum*, 2(2):020310, April 2021.

- [109] Abhinav Kandala, Antonio Mezzacapo, Kristan Temme, Maika Takita, Markus Brink, Jerry M Chow, and Jay M Gambetta. Hardware-efficient variational quantum eigensolver for small molecules and quantum magnets. *Nature*, 549(7671):242–246, 2017.
- [110] M. Ganzhorn, D. J. Egger, P. Barkoutsos, P. Ollitrault, G. Salis, N. Salis, M. Roth, A. Fuhrer, P. Mueller, S. Woerner, I. Tavernelli, and S Filipp. Gate-Efficient Simulation of Molecular Eigenstates on a Quantum Computer. *Phys. Rev. Appl.*, 11:044092, 2019.
- [111] Arthur G Rattew, Shaohan Hu, Marco Pistoia, Richard Chen, and Steve Wood. A Domain-agnostic, Noise-resistant Evolutionary Variational Quantum Eigensolver for Hardware-efficient Optimization in the Hilbert Space. *arXiv e-prints*, pages arXiv:1910.09694 [quant-ph], October 2019.
- [112] Oscar Higgott, Daochen Wang, and Stephen Brierley. Variational quantum computation of excited states. *Quantum*, 3:156, 2019.
- [113] J I Colless, V V Ramasesh, D Dahlen, M S Blok, M E Kimchi-Schwartz, Jarrod R McClean, J Carter, W A de Jong, and I Siddiqi. Computation of molecular spectra on a quantum processor with an error-resilient algorithm. *Phys. Rev. X*, 8(1):011021, 2018.

- [114] Robert M Parrish, Edward G Hohenstein, Peter L McMahon, and Todd J Martinez. Quantum Computation of Electronic Transitions Using a Variational Quantum Eigensolver. *Phys. Rev. Lett.*, 122(23):230401, June 2019.
- [115] Ken M Nakanishi, Kosuke Mitarai, and Keisuke Fujii. Subspace-search variational quantum eigensolver for excited states. *Phys. Rev. Research*, 1(3):033062, 2019.
- [116] P Jouzdani, M Kostuk, and Stefan Bringuier. A Method of Determining Excited-States for Quantum Computation. *arXiv e-prints*, pages arXiv:1908.05238 [quant-ph], August 2019.
- [117] Gabriel Greene-Diniz and David Muñoz Ramo. Calculation of excited states via symmetry constraints in the Variational Quantum Eigensolver. *arXiv e-prints*, pages arXiv:1910.05168 [quant-ph], October 2019.
- [118] Jules Tilly, Glenn Jones, Hongxiang Chen, Leonard Wossnig, and Edward Grant. Computation of molecular excited states on IBM quantum computers using a discriminative variational quantum eigensolver. *Phys. Lett. A*, 102(6):062425, December 2020.
- [119] Daochen Wang, Oscar Higgott, and Stephen Brierley. Accelerated Variational Quantum Eigensolver. *Phys. Rev. Lett.*, 122(14):140504, April 2019.
- [120] Raffaele Santagati, Jianwei Wang, Antonio A Gentile, Stefano Paesani, Nathan Wiebe, Jarrod R McClean, Sam Morley-Short, Peter J Shadbolt,

- Damien Bonneau, Joshua W Silverstone, David P Tew, Xiaoqi Zhou, Jeremy L O'Brien, and Mark G Thompson. Witnessing eigenstates for quantum simulation of Hamiltonian spectra. *Sci. Adv.*, 4(1):eaap9646, January 2018.
- [121] Cornelius Hempel, Christine Maier, Jonathan Romero, Thomas Monz, Heng Shen, Petar Jurcevic, Ben P Lanyon, Ryan Babbush, Alán Aspuru-Guzik, Rainer Blatt, Christian F Roos, Peter J Love, and Jarrod R McClean. Quantum Chemistry Calculations on a Trapped-Ion Quantum Simulator. *Phys. Rev. X*, 8(3):1, July 2018.
- [122] Yangchao Shen, Xiang Zhang, Shuaining Zhang, Jing-Ning Zhang, Man-Hong Yung, and Kihwan Kim. Quantum implementation of the unitary coupled cluster for simulating molecular electronic structure. *Phys. Rev. A*, 95(2):020501(R), February 2017.
- [123] Jarrod R McClean, Sergio Boixo, Vadim N Smelyanskiy, Ryan Babbush, and Hartmut Neven. Barren plateaus in quantum neural network training landscapes. *Nat. Commun.*, 9(1):4812, November 2018.
- [124] Panagiotis Kl Barkoutsos, Giacomo Nannicini, Anton Robert, Ivano Tavernelli, and Stefan Woerner. Improving Variational Quantum Optimization using CVaR. *arXiv e-prints*, pages arXiv:1907.04769 [quant-ph], 2019.
- [125] Francesco A Evangelista, Garnet Kin-Lic Chan, and Gustavo E Scuseria. Exact parameterization of fermionic wave functions via unitary coupled cluster theory. *J. Chem. Phys.*, 151(24):244112, December 2019.

- [126] P O Löwdin. On the Non-Orthogonality Problem Connected with the Use of Atomic Wave Functions in the Theory of Molecules and Crystals. *J. Chem. Phys.*, 18(3):365–375, 1950.
- [127] Harry F King, Richard E Stanton, Hojing Kim, Robert E Wyatt, and Robert G Parr. Corresponding Orbitals and the Nonorthogonality Problem in Molecular Quantum Mechanics. *J. Chem. Phys.*, 47(6):1936–1941, 1967.
- [128] Louis Noodleman. Valence bond description of antiferromagnetic coupling in transition metal dimers. *J. Chem. Phys.*, 74(10):5737–5743, 1981.
- [129] Arthur F Voter and William A Goddard III. The generalized resonating valence bond method: Barrier heights in the HF + D and HCl + D exchange reactions. *J. Chem. Phys.*, 75(7):3638–3639, June 1981.
- [130] P-Å Malmqvist. Calculation of transition density matrices by nonunitary orbital transformations. *Int. J. Quantum Chem.*, 30(4):479–494, October 1986.
- [131] Henrik Koch and E Dalgaard. Linear superposition of optimized nonorthogonal Slater determinants for singlet-states. *Chem. Phys. Lett.*, 212(1-2):193–200, 1993.
- [132] Alex JW Thom and Martin Head-Gordon. Hartree–fock solutions as a quasidiabatic basis for nonorthogonal configuration interaction. *J. Chem. Phys.*, 131(12):124113, 2009.

- [133] Eric J Sundstrom and Martin Head-Gordon. Non-orthogonal configuration interaction for the calculation of multielectron excited states. *J. Chem. Phys.*, 140(11):114103, 2014.
- [134] Robert M Parrish and Peter L McMahon. Quantum Filter Diagonalization: Quantum Eigendecomposition without Full Quantum Phase Estimation. *arXiv e-prints*, pages arXiv:1909.08925 [quant-ph], September 2019.
- [135] William J Huggins, Joonho Lee, Unpil Baek, Bryan O’Gorman, and K Birgitta Whaley. A Non-Orthogonal Variational Quantum Eigensolver. *New J. Phys.*, 22(7):073009, July 2020.
- [136] Pauline J Ollitrault, Abhinav Kandala, Chun-Fu Chen, Panagiotis Kl Barkoutsos, Antonio Mezzacapo, Marco Pistoia, Sarah Sheldon, Stefan Woerner, Jay M Gambetta, and Ivano Tavernelli. Quantum equation of motion for computing molecular excitation energies on a noisy quantum processor. *Phys. Rev. Research*, 2(4):043140, October 2020.
- [137] Tyler Takeshita, Nicholas C Rubin, Zhang Jiang, Eunseok Lee, Ryan Babbush, and Jarrod R McClean. Increasing the Representation Accuracy of Quantum Simulations of Chemistry without Extra Quantum Resources. *Phys. Rev. X*, 10(1):011004, January 2020.
- [138] Nick S Blunt, Ali Alavi, and George H Booth. Nonlinear biases, stochastically sampled effective Hamiltonians, and spectral functions in quantum Monte Carlo methods. *Phys. Rev. B*, 98(8):085118, 2018.

- [139] Hale Freeman Trotter. On the product of semi-groups of operators. *Proc. Amer. Math. Soc.*, 10(4):545–545, April 1959.
- [140] Nicholas H. Stair, Renke Huang, and Francesco A Evangelista. A Multireference Quantum Krylov Algorithm for Strongly Correlated Electrons. *J. Chem. Theory Comput.*, 16(4):2236–2245, February 2020.
- [141] Dorit Aharonov, Vaughan Jones, and Zeph Landau. A polynomial quantum algorithm for approximating the jones polynomial. *Algorithmica*, 55(3):395–421, 2009.
- [142] Daniel Neuhauser. Circumventing the Heisenberg principle: A rigorous demonstration of filter-diagonalization on a LiCN model. *J. Chem. Phys.*, 100(7):5076–5079, April 1994.
- [143] Daniel Neuhauser. Bound state eigenfunctions from wave packets: Time→energy resolution. *J. Chem. Phys.*, 93(4):2611–2616, August 1990.
- [144] Michael R Wall and Daniel Neuhauser. Extraction, through filter-diagonalization, of general quantum eigenvalues or classical normal mode frequencies from a small number of residues or a short-time segment of a signal. i. theory and application to a quantum-dynamics model. *J. Chem. Phys.*, 102(20):8011–8022, 1995.
- [145] Vladimir A Mandelshtam and Howard S Taylor. A low-storage filter diagonalization method for quantum eigenenergy calculation or for spectral analysis of time signals. *J. Chem. Phys.*, 106(12):5085–5090, 1997.

- [146] Rolando D Somma, Gerardo Ortiz, R Laflamme, James E Gubernatis, and Emanuel Knill. Simulating Physical Phenomena by Quantum Networks. *Phys. Rev. A*, 65:042323, April 2002.
- [147] Rolando D Somma. Quantum eigenvalue estimation via time series analysis. *New J. Phys.*, 21:123025, 2019.
- [148] Thomas E O’Brien, Brian Tarasinski, and Barbara M Terhal. Quantum phase estimation of multiple eigenvalues for small-scale (noisy) experiments. *New J. Phys.*, 21(2):023022, February 2019.
- [149] Oleksandr Kyriienko. Quantum inverse iteration algorithm for programmable quantum simulators. *npj Quantum Inf.*, 6(1):7, 2020.
- [150] James D Whitfield, Jacob Biamonte, and Alán Aspuru-Guzik. Simulation of electronic structure hamiltonians using quantum computers. *Mol. Phys.*, 109(5):735–750, 2011.
- [151] Roger A Horn and Charles R Johnson. *Matrix analysis*. Cambridge University Press, New York, NY, 2012.
- [152] Masuo Suzuki. General theory of fractal path integrals with applications to many-body theories and statistical physics. *J. Math. Phys.*, 32(2):400–407, February 1991.
- [153] Naomichi Hatano and Masuo Suzuki. Finding Exponential Product Formulas of Higher Orders . In *Quantum Annealing and Other Optimization Methods*, pages 37–68. Springer, Berlin, Heidelberg, 2005.

- [154] Masuo Suzuki. Generalized Trotter's formula and systematic approximations of exponential operators and inner derivations with applications to many-body problems. *Commun. Math. Phys.*, 51(2):183–190, June 1976.
- [155] Dominic W Berry, Graeme Ahokas, Richard Cleve, and Barry C Sanders. Efficient Quantum Algorithms for Simulating Sparse Hamiltonians. *Commun. Math. Phys.*, 270(2):359–371, 2007.
- [156] Dominic W Berry, Andrew M Childs, Richard Cleve, Robin Kothari, and Rolando D Somma. Simulating Hamiltonian Dynamics with a Truncated Taylor Series. *Phys. Rev. Lett.*, 114(9):090502, March 2015.
- [157] Ryan Babbush, Dominic W Berry, Ian D Kivlichan, Annie Y Wei, Peter J Love, and Alán Aspuru-Guzik. Exponentially more precise quantum simulation of fermions in second quantization. *New J. Phys.*, 18(3):033032–18, March 2016.
- [158] Andrew M Childs and Nathan Wiebe. Hamiltonian Simulation Using Linear Combinations of Unitary Operations. *Quantum Inf. Comput.*, 12:901–924, November 2012.
- [159] Sathyawageeswar Subramanian, Stephen Brierley, and Richard Jozsa. Implementing smooth functions of a Hermitian matrix on a quantum computer. *J. Phys. Commun.*, 3(6):065002, June 2019.
- [160] Guang Hao Low and Isaac L. Chuang. Hamiltonian simulation by qubitization. *Quantum*, 3:163, July 2019.

- [161] Dominic W Berry, Mária Kieferová, Artur Scherer, Yuval R Sanders, Guang Hao Low, Nathan Wiebe, Craig Gidney, and Ryan Babbush. Improved techniques for preparing eigenstates of fermionic Hamiltonians. *npj Quantum Inf.*, 4:22, May 2018.
- [162] Guang Hao Low and Isaac L Chuang. Optimal Hamiltonian Simulation by Quantum Signal Processing. *Phys. Rev. Lett.*, 118(1):901–5, January 2017.
- [163] Matthew B Hastings, Dave Wecker, Bela Bauer, and Matthias Troyer. Improving Quantum Algorithms for Quantum Chemistry. *Quantum Inf. Comput.*, 15(1-2):1, January 2015.
- [164] Rolando D Somma, Gerardo Ortiz, Emanuel Knill, and James E Gubernatis. Quantum Simulations of Physics Problems. *Int. J. Quantum Inf.*, 1:189–206, 2003.
- [165] Kenji Sugisaki, Shigeaki Nakazawa, Kazuo Toyota, Kazunobu Sato, Daisuke Shiomi, and Takeji Takui. Quantum Chemistry on Quantum Computers: A Method for Preparation of Multiconfigurational Wave Functions on Quantum Computers without Performing Post-Hartree–Fock Calculations. *ACS Cent. Sci.*, 5(1):167–175, January 2019.
- [166] Nikolaj Moll, Andreas Fuhrer, Peter Staar, and Ivano Tavernelli. Optimizing qubit resources for quantum chemistry simulations in second quantization on a quantum computer. *J. Phys. A: Math. Theor.*, 49(29):295301, June 2016.

- [167] Sergey Bravyi, Jay M Gambetta, Antonio Mezzacapo, and Kristan Temme. Tapering off qubits to simulate fermionic Hamiltonians. *arXiv preprint arXiv:1701.08213*, 2017.
- [168] G. Aleksandrowicz et al. Qiskit: An Open-source Framework for Quantum Computing. 2023.
- [169] Nicholas H Stair and Francesco A Evangelista. Qforte: An efficient state-vector emulator and quantum algorithms library for molecular electronic structure. *J. Chem. Theory Comput.*, 18(3):1555–1568, 2022.
- [170] Robert M Parrish, Lori A Burns, Daniel G A Smith, Andrew C Simmonett, A Eugene DePrince III, Edward G Hohenstein, Uğur Bozkaya, Alexander Yu Sokolov, Roberto Di Remigio, Ryan M Richard, Jérôme F Gonthier, Andrew M James, Harley R McAlexander, Ashutosh Kumar, Masaaki Saitow, Xiao Wang, Benjamin P Pritchard, Prakash Verma, Henry F Schaefer III, Konrad Patkowski, Rollin A King, Edward F Valeev, Francesco A Evangelista, Justin M Turney, T Daniel Crawford, and C David Sherrill. Psi4.1.1: An Open-Source Electronic Structure Program Emphasizing Automation, Advanced Libraries, and Interoperability. *J. Chem. Theory Comput.*, 13(7):3185–3197, June 2017.
- [171] W. J. Hehre, R. F. Stewart, and J. A. Pople. Self-consistent molecular-orbital methods. i. use of gaussian expansions of slater-type atomic orbitals. *J. Chem. Phys.*, 51, 1969.

- [172] Jarrod R McClean, Kevin J Sung, Ian D Kivlichan, Yudong Cao, Chengyu Dai, E Schuyler Fried, Craig Gidney, Brendan Gimby, Pranav Gokhale, Thomas Häner, Tarini Hardikar, Oscar Higgott, Cupjin Huang, Josh Izaac, Zhang Jiang, Xinle Liu, Sam McArdle, Matthew Neeley, Thomas O'Brien, Bryan O'Gorman, Isil Ozfidan, Maxwell D Radin, Jonathan Romero, Nicholas Rubin, Nicolas P D Sawaya, Kanav Setia, Sukin Sim, Damian S Steiger, Mark Steudtner, Qiming Sun, Wei Sun, Daochen Wang, Fang Zhang, and Ryan Babbush. OpenFermion: The Electronic Structure Package for Quantum Computers. *Quantum Sci. Technol.*, 5:034014, June 2020.
- [173] Anton V Sinitskiy, Loren Greenman, and David A Mazziotti. Strong correlation in hydrogen chains and lattices using the variational two-electron reduced density matrix method. *J. Chem. Phys.*, 133(1):014104, 2010.
- [174] Lorenzo Stella, Claudio Attaccalite, Sandro Sorella, and Angel Rubio. Strong electronic correlation in the hydrogen chain: A variational monte carlo study. *Phys. Rev. B*, 84(24):245117, 2011.
- [175] Mario Motta, David M Ceperley, Garnet Kin-Lic Chan, John A Gomez, Emanuel Gull, Sheng Guo, Carlos A Jiménez-Hoyos, Tran Nguyen Lan, Jia Li, and Fengjie Ma. Towards the solution of the many-electron problem in real materials: equation of state of the hydrogen chain with state-of-the-art many-body methods. *Phys. Rev. X*, 7(3):031059, 2017.

- [176] Mario Motta, Claudio Genovese, Fengjie Ma, Zhi-Hao Cui, Randy Sawaya, Garnet Kin-Lic Chan, Natalia Chepiga, Phillip Helms, Carlos Jimenez-Hoyos, Andrew J Millis, Ushnish Ray, Enrico Ronca, Hao Shi, Sandro Sorella, Edwin M Stoudenmire, Steven R White, and Shiwei Zhang. Ground-state properties of the hydrogen chain: insulator-to-metal transition, dimerization, and magnetic phases. *Phys. Rev. X*, pages arXiv:1911.01618 [cond-mat.str-el], November 2019.
- [177] Isaiah Shavitt and Rodney J Bartlett. *Many-body methods in chemistry and physics: MBPT and coupled-cluster theory*. Cambridge University Press, New York, NY, 2009.
- [178] B Huron, Jean Paul Malrieu, and P Rancurel. Iterative perturbation calculations of ground and excited state energies from multiconfigurational zeroth-order wavefunctions. *J. Chem. Phys.*, 58(12):5745, 1973.
- [179] Jeffrey B. Schriber and Francesco A. Evangelista. Communication: An adaptive configuration interaction approach for strongly correlated electrons with tunable accuracy. *J. Chem. Phys.*, 144(16):161106, 2016.
- [180] Adam A. Holmes, Norm M. Tubman, and C. J. Umrigar. Heat-bath configuration interaction: An efficient selected configuration interaction algorithm inspired by heat-bath sampling. *J. Chem. Theory and Comput.*, 12(8):3674–3680, 2016.
- [181] Norm M Tubman, Joonho Lee, Tyler Y Takeshita, Martin Head-Gordon, and K Birgitta Whaley. A deterministic alternative to the full config-

- uration interaction quantum Monte Carlo method. *J. Chem. Phys.*, 145(4):044112, July 2016.
- [182] Yann Garniron, Anthony Scemama, Pierre-François Loos, and Michel Caffarel. Hybrid stochastic-deterministic calculation of the second-order perturbative contribution of multireference perturbation theory. *J. Chem. Phys.*, 147(3):034101, July 2017.
- [183] David Poulin, Alexei Kitaev, Damian S Steiger, Matthew B Hastings, and Matthias Troyer. Quantum Algorithm for Spectral Measurement with a Lower Gate Count. *Phys. Rev. Lett.*, 121(1):010501, July 2018.
- [184] Andrew Tranter, Peter J Love, Florian Mintert, Nathan Wiebe, and Peter V Coveney. Ordering of trotterization: Impact on errors in quantum simulation of electronic structure. *Entropy*, 21(12):1218, 2019.
- [185] Kosuke Mitarai and Keisuke Fujii. Methodology for replacing indirect measurements with direct measurements. *Phys. Rev. Research*, 1(1):013006, August 2019.
- [186] Artur F Izmaylov, Tzu-Ching Yen, and Ilya G Ryabinkin. Revising the measurement process in the variational quantum eigensolver: is it possible to reduce the number of separately measured operators? *Chem. Sci.*, 10(13):3746–3755, 2019.
- [187] Artur F Izmaylov, Tzu-Ching Yen, Robert A Lang, and Vladyslav Verteletskyi. Unitary Partitioning Approach to the Measurement Problem in the Variational Quantum Eigensolver Method. *J. Chem. Theory Comput.*, 16(1):190–195, November 2019.

- [188] Pranav Gokhale, Olivia Angiuli, Yongshan Ding, Kaiwen Gui, Teague Tomesh, Martin Suchara, Margaret Martonosi, and Frederic T Chong. Minimizing State Preparations in Variational Quantum Eigensolver by Partitioning into Commuting Families. *arXiv e-prints*, pages arXiv:1907.13623 [quant-ph], July 2019.
- [189] Andrew Zhao, Andrew Tranter, William M Kirby, Shu Fay Ung, Akimasa Miyake, and Peter J Love. Measurement reduction in variational quantum algorithms. *arXiv e-prints*, pages arXiv:1908.08067 [quant-ph], 2019.
- [190] Pranav Gokhale, Olivia Angiuli, Yongshan Ding, Kaiwen Gui, Teague Tomesh, Martin Suchara, Margaret Martonosi, and Frederic T Chong. $O(N^3)$ Measurement Cost for Variational Quantum Eigensolver on Molecular Hamiltonians. *IEEE Trans. on Quantum Eng.*, 1:1–24, 2020.
- [191] Jeffrey B Schriber and Francesco A Evangelista. Adaptive Configuration Interaction for Computing Challenging Electronic Excited States with Tunable Accuracy. *J. Chem. Theory Comput.*, 13(11):5354–5366, October 2017.
- [192] Jeffrey B Schriber, Kevin P Hannon, Chenyang Li, and Francesco A Evangelista. A Combined Selected Configuration Interaction and Many-Body Treatment of Static and Dynamical Correlation in Oligoacenes. *J. Chem. Theory Comput.*, 14(12):6295–6305, November 2018.
- [193] Spiridoula Matsika and Pascal Krause. Nonadiabatic Events and Conical Intersections. *Annu. Rev. Phys. Chem.*, 62(1):621–643, May 2011.

- [194] David R Yarkony. Nonadiabatic Quantum Chemistry—Past, Present, and Future. *Chem. Rev.*, 112(1):481–498, January 2012.
- [195] Lluís Blancafort. Photochemistry and Photophysics at Extended Seams of Conical Intersection. *ChemPhysChem*, 15(15):3166–3181, October 2014.
- [196] Andreas Dreuw and Martin Head-Gordon. Single-Reference ab Initio Methods for the Calculation of Excited States of Large Molecules. *Chem. Rev.*, 105(11):4009–4037, November 2005.
- [197] E Runge and E K U Gross. Density-functional theory for time-dependent systems. *Phys. Rev. Lett.*, 52(12):997–1000, 1984.
- [198] Kieron Burke, Jan Werschnik, and E K U Gross. Time-dependent density functional theory: Past, present, and future. *J. Chem. Phys.*, 123(6):062206, 2005.
- [199] John F Stanton and Rodney J Bartlett. The equation of motion coupled-cluster method. A systematic biorthogonal approach to molecular excitation energies, transition probabilities, and excited state properties. *J. Chem. Phys.*, 98(9):7029–7039, 1993.
- [200] Ove Christiansen, Henrik Koch, and Poul Jørgensen. The second-order approximate coupled cluster singles and doubles model CC2. *Chem. Phys. Lett.*, 243(5-6):409–418, 1995.
- [201] J Patrick Zobel, Juan J Nogueira, and Leticia González. The IPEA dilemma in CASPT2. *Chem. Sci.*, 8(2):1482–1499, 2017.

- [202] J P Coe and M J Paterson. State-averaged Monte Carlo configuration interaction applied to electronically excited states. *J. Chem. Phys.*, 139(15):154103, 2013.
- [203] Bela Bauer, Dave Wecker, Andrew J Millis, Matthew B Hastings, and Matthias Troyer. Hybrid Quantum-Classical Approach to Correlated Materials. *Phys. Rev. X*, 6:031045, September 2016.
- [204] Miroslav Urbanek, Daan Camps, Roel Van Beeumen, and Wibe A de Jong. Chemistry on Quantum Computers with Virtual Quantum Subspace Expansion. *J. Chem. Theory Comput.*, 16(9):5425–5431, August 2020.
- [205] Jan-Niklas Boyn, Aleksandr O Lykhin, Scott E Smart, Laura Gagliardi, and David A Mazziotti. Quantum-classical hybrid algorithm for the simulation of all-electron correlation. *J. Chem. Phys.*, 155(24):244106, December 2021.
- [206] David A Mazziotti. Anti-Hermitian Contracted Schrödinger Equation: Direct Determination of the Two-Electron Reduced Density Matrices of Many-Electron Molecules. *Phys. Rev. Lett.*, 97(14):143002, October 2006.
- [207] Scott E Smart and David A Mazziotti. Quantum Solver of Contracted Eigenvalue Equations for Scalable Molecular Simulations on Quantum Computing Devices. *Phys. Rev. Lett.*, 126(7):070504, February 2021.

- [208] Scott E Smart, Jan-Niklas Boyn, and David A Mazziotti. Resolving correlated states of benzyne with an error-mitigated contracted quantum eigensolver. *Phys. Rev. A*, 105(2):022405, February 2022.
- [209] Giovanni Li Manni, Rebecca K Carlson, Sijie Luo, Dongxia Ma, Jeppe Olsen, Donald G Truhlar, and Laura Gagliardi. Multiconfiguration Pair-Density Functional Theory. *J. Chem. Theory Comput.*, 10(9):3669–3680, September 2014.
- [210] Keisuke Fujii, Kaoru Mizuta, Hiroshi Ueda, Kosuke Mitarai, Wataru Mizukami, and Yuya O Nakagawa. Deep variational quantum eigensolver: a divide-and-conquer method for solving a larger problem with smaller size quantum computers. *PRX Quantum*, 3(1):010346, 2022.
- [211] Kaoru Mizuta, Mikiya Fujii, Shigeki Fujii, Kazuhide Ichikawa, Yutaka Imamura, Yukihiro Okuno, and Yuya O Nakagawa. Deep variational quantum eigensolver for excited states and its application to quantum chemistry calculation of periodic materials. *Phys. Rev. Res.*, 3(4):043121, 2021.
- [212] Fionn D Malone, Robert M Parrish, Alicia R Welden, Thomas Fox, Matthias Degroote, Elica Kyoseva, Nikolaj Moll, Raffaele Santagati, and Michael Streif. Towards the simulation of large scale protein–ligand interactions on nisq-era quantum computers. *Chem. Sci.*, 13(11):3094–3108, 2022.
- [213] Matthias Loipersberger, Fionn Malone, Robert M Parrish, Alicia R Welden, Thomas Fox, Matthias Degroote, Elica Kyoseva, Nikolaj Moll,

- Raffaele Santagati, and Michael Streif. Accurate non-covalent interaction energies on noisy intermediate-scale quantum computers via second-order symmetry-adapted perturbation theory. *Chem. Sci.*, 2023.
- [214] Huan Ma, Jie Liu, Honghui Shang, Yi Fan, Zhenyu Li, and Jinlong Yang. Multiscale quantum algorithms for quantum chemistry. *Chem. Sci.*, 14(12):3190–3205, 2023.
- [215] Alessandro Tammaro, Davide E Galli, Julia E Rice, and Mario Motta. N-electron valence perturbation theory with reference wave functions from quantum computing: Application to the relative stability of hydroxide anion and hydroxyl radical. *J. Phys. Chem. A*, 127(3):817–827, 2023.
- [216] Celestino Angeli, Renzo Cimiraglia, Stefano Evangelisti, T Leininger, and Jean Paul Malrieu. Introduction of n-electron valence states for multireference perturbation theory. *J. Chem. Phys.*, 114:10252, 2001.
- [217] Celestino Angeli, Mariachiara Pastore, and Renzo Cimiraglia. New perspectives in multireference perturbation theory: the n-electron valence state approach. *Theor. Chem. Acc.*, 117(5-6):743–754, December 2007.
- [218] Ilya G Ryabinkin, Artur F Izmaylov, and Scott N Genin. A posteriori corrections to the iterative qubit coupled cluster method to minimize the use of quantum resources in large-scale calculations. *Quantum Sci. Technol.*, 6(2):024012, mar 2021.
- [219] William J Huggins, Bryan A O’Gorman, Nicholas C Rubin, David R Reichman, Ryan Babbush, and Joonho Lee. Unbiasing fermionic quantum

- Monte Carlo with a quantum computer. *Nature*, 603(7901):416–420, March 2022.
- [220] Gerald Knizia and Garnet Kin-Lic Chan. Density Matrix Embedding: A Simple Alternative to Dynamical Mean-Field Theory. *Phys. Rev. Lett.*, 109(18):186404, November 2012.
- [221] Sebastian Wouters, Carlos A Jiménez-Hoyos, Qiming Sun, and Garnet K-L Chan. A practical guide to density matrix embedding theory in quantum chemistry. *J. Chem. Theory Comput.*, 12(6):2706–2719, 2016.
- [222] Yukio Kawashima, Erika Lloyd, Marc P Coons, Yunseong Nam, Shunji Matsuura, Alejandro J Garza, Sonika Johri, Lee Huntington, Valentin Senicourt, Andrii O Maksymov, Jason H V Nguyen, Jungsang Kim, Nima Alidoust, Arman Zaribafiyani, and Takeshi Yamazaki. Optimizing electronic structure simulations on a trapped-ion quantum computer using problem decomposition. *Commun Phys*, 4:245, November 2021.
- [223] Benchen Huang, Marco Govoni, and Giulia Galli. Simulating the electronic structure of spin defects on quantum computers. *PRX Quantum*, 3(1):010339, March 2022.
- [224] Ruslan N Tazhigulov, Shi-Ning Sun, Reza Haghshenas, Huanchen Zhai, Adrian TK Tan, Nicholas C Rubin, Ryan Babbush, Austin J Minnich, and Garnet Kin Chan. Simulating challenging correlated molecules and materials on the sycamore quantum processor. *arXiv preprint arXiv:2203.15291*, 2022.

- [225] Mario Motta, Tanvi P Gujarati, Julia E Rice, Ashutosh Kumar, Conner Masteran, Joseph A Latone, Eunseok Lee, Edward F Valeev, and Tyler Y Takeshita. Quantum simulation of electronic structure with a transcorrelated Hamiltonian: improved accuracy with a smaller footprint on the quantum computer. *Phys. Chem. Chem. Phys.*, 22(42):24270–24281, 2020.
- [226] Sam McArdle and David P Tew. Improving the accuracy of quantum computational chemistry using the transcorrelated method. *arXiv preprint arXiv:2006.11181*, 2020.
- [227] Philipp Schleich, Jakob S Kottmann, and Alán Aspuru-Guzik. Improving the accuracy of the variational quantum eigensolver for molecular systems by the explicitly-correlated perturbative [2] R12 - correction. *Phys. Chem. Chem. Phys.*, 24(22):13550–13564, 2022.
- [228] Ashutosh Kumar, Ayush Asthana, Conner Masteran, Edward F Valeev, Yu Zhang, Lukasz Cincio, Sergei Tretiak, and Pavel A Dub. Quantum simulation of molecular electronic states with a transcorrelated hamiltonian: Higher accuracy with fewer qubits. *J. Chem. Theory Comput.*, 18(9):5312–5324, 2022.
- [229] Igor O Sokolov, Werner Dobrautz, Hongjun Luo, Ali Alavi, and Ivano Tavernelli. Orders of magnitude increased accuracy for quantum many-body problems on quantum computers via an exact transcorrelated method. *Phys.Rev. Res.*, 5(2):023174, 2023.

- [230] Takeshi Yanai and Toru Shiozaki. Canonical transcorrelated theory with projected Slater-type geminals. *J. Chem. Phys.*, 136(8):084107–10, February 2012.
- [231] Steven R White. Numerical canonical transformation approach to quantum many-body problems. *J. Chem. Phys.*, 117(16):7472–7482, 2002.
- [232] T Yanai and Garnet Kin-Lic Chan. Canonical transformation theory for multireference problems. *J. Chem. Phys.*, 124(19):194106, 2006.
- [233] Takeshi Yanai, Yuki Kurashige, Eric Neuscamman, and Garnet Kin-Lic Chan. Multireference quantum chemistry through a joint density matrix renormalization group and canonical transformation theory. *J. Chem. Phys.*, 132(2):024105, 2010.
- [234] F. Spiegelmann and J. P. Malrieu. The use of effective Hamiltonians for the treatment of avoided crossings. I. Adiabatic potential curves. *J. Phys. B At. Mol. Phys.*, 17(7):1235–1257, 1984.
- [235] Dmitry I Lyakh, Monika Musiał, Victor F Lotrich, and Rodney J Bartlett. Multireference Nature of Chemistry: The Coupled-Cluster View. *Chem. Rev.*, 112(1):182–243, January 2012.
- [236] Andreas Köhn, Matthias Hanauer, Leonie Anna Mück, Thomas-Christian Jagau, and Jürgen Gauss. State-specific multireference coupled-cluster theory. *Wiley Interdiscip. Rev.: Comput. Mol. Sci.*, 3(2):176–197, March 2013.

- [237] Francesco A Evangelista. Perspective: Multireference coupled cluster theories of dynamical electron correlation. *J. Chem. Phys.*, 149(3):030901, July 2018.
- [238] Nicholas P Bauman, Eric J Bylaska, Sriram Krishnamoorthy, Guang Hao Low, Nathan Wiebe, Christopher E Granade, Martin Roetteler, Matthias Troyer, and Karol Kowalski. Downfolding of many-body Hamiltonians using active-space models: Extension of the sub-system embedding sub-algebras approach to unitary coupled cluster formalisms. *J. Chem. Phys.*, 151(1):014107, 2019.
- [239] Mekena Metcalf, Nicholas P Bauman, Karol Kowalski, and Wibe A de Jong. Resource-Efficient Chemistry on Quantum Computers with the Variational Quantum Eigensolver and the Double Unitary Coupled-Cluster Approach. *J. Chem. Theory Comput.*, 16(10):6165–6175, October 2020.
- [240] Nicholas P Bauman, Jaroslav Chladek, Libor Veis, Jiří Pittner, and Karol Kowalski. Variational quantum eigensolver for approximate diagonalization of downfolded Hamiltonians using generalized unitary coupled cluster ansatz. *Quantum Sci. Technol.*, 6(3):034008, June 2021.
- [241] Nhan Trong Le and Lan Nguyen Tran. Correlated reference-assisted variational quantum eigensolver. e-print arXiv:2205.03539 [cond-mat.str-el], 2022.

- [242] Francesco A Evangelista. A driven similarity renormalization group approach to quantum many-body problems. *J. Chem. Phys.*, 141(5):054109, 2014.
- [243] Chenyang Li and Francesco A Evangelista. Multireference driven similarity renormalization group: a second-order perturbative analysis. *J. Chem. Theory Comput.*, 11(5):2097–2108, 2015.
- [244] Chenyang Li and Francesco A Evangelista. Towards numerically robust multireference theories: The driven similarity renormalization group truncated to one-and two-body operators. *J. Chem. Phys.*, 144(16):164114, 2016.
- [245] Chenyang Li and Francesco A Evangelista. Multireference theories of electron correlation based on the driven similarity renormalization group. *Annu. Rev. Phys. Chem.*, 70:245–273, 2019.
- [246] Franz Wegner. Flow-equations for Hamiltonians. *Ann. Phys.*, 506(2):77–91, 1994.
- [247] Stanislaw D Głazek and Kenneth G Wilson. Perturbative renormalization group for Hamiltonians. *Phys. Rev. D*, 49(8):4214–4218, 1994.
- [248] K Tsukiyama, S K Bogner, and A Schwenk. In-medium similarity renormalization group for open-shell nuclei. *Phys. Rev. C*, 85(6):061304, June 2012.
- [249] H Hergert. In-medium similarity renormalization group for closed and open-shell nuclei. *Physica Scripta*, 92(2):023002, February 2017.

- [250] Jeffrey Cohn, Mario Motta, and Robert M Parrish. Quantum Filter Diagonalization with Compressed Double-Factorized Hamiltonians. *PRX Quantum*, 2(4):040352, December 2021.
- [251] Jun Shen and Piotr Piecuch. Combining active-space coupled-cluster methods with moment energy corrections via the cc (p; q) methodology, with benchmark calculations for biradical transition states. *J. Chem. Phys.*, 136(14):144104, 2012.
- [252] Google AI Quantum and Collaborators. Hartree-Fock on a superconducting qubit quantum computer. *Science*, 369(6507):1084–1089, August 2020.
- [253] Mario Motta, Gavin O Jones, Julia E Rice, Tanvi P Gujarati, Rei Sakuma, Ieva Liepuoniute, Jeannette M Garcia, and Yu-ya Ohnishi. Quantum chemistry simulation of ground-and excited-state properties of the sulfonium cation on a superconducting quantum processor. *arXiv preprint arXiv:2208.02414*, 2022.
- [254] Thomas E O’Brien, G Anselmetti, Fotios Gkritis, VE Elfving, Stefano Polla, William J Huggins, Oumarou Oumarou, Kostyantyn Kechedzhi, Dmitry Abanin, Rajeev Acharya, et al. Purification-based quantum error mitigation of pair-correlated electron simulations. *arXiv preprint arXiv:2210.10799*, 2022.
- [255] Chenyang Li and Francesco A Evangelista. Spin-free formulation of the multireference driven similarity renormalization group: A benchmark

- study of first-row diatomic molecules and spin-crossover energetics. *J. Chem. Phys.*, 155(11):114111, September 2021.
- [256] John D Watts, Gary W Trucks, and Rodney J Bartlett. The unitary coupled-cluster approach and molecular properties. Applications of the UCC(4) method. *Chem. Phys. Lett.*, 157(4):359–366, 1989.
- [257] Monika Musial and Rodney J Bartlett. Intermediate Hamiltonian Fock-space multireference coupled-cluster method with full triples for calculation of excitation energies. *J. Chem. Phys.*, 129(4):044101, 2008.
- [258] Monika Musial and Rodney J Bartlett. Multireference Fock-space coupled-cluster and equation-of-motion coupled-cluster theories: The detailed interconnections. *J. Chem. Phys.*, 129(13):134105–134105–12, 2008.
- [259] T Daniel Crawford and Henry F Schaefer. An introduction to coupled cluster theory for computational chemists. *Rev. Comp. Chem.*, 14:33–136, 2000.
- [260] Debashis Mukherjee. Normal ordering and a Wick-like reduction theorem for fermions with respect to a multi-determinantal reference state. *Chem. Phys. Lett.*, 274(5-6):561–566, 1997.
- [261] Werner Kutzelnigg and Debashis Mukherjee. Normal order and extended Wick theorem for a multiconfiguration reference wave function. *J. Chem. Phys.*, 107(2):432–449, 1997.

- [262] Francesco A Evangelista and Jürgen Gauss. On the approximation of the similarity-transformed Hamiltonian in single-reference and multi-reference coupled cluster theory. *Chem. Phys.*, 401:27–35, June 2012.
- [263] Eric Neuscamman, Takeshi Yanai, and Garnet Kin-Lic Chan. Quadratic canonical transformation theory and higher order density matrices. *J. Chem. Phys.*, 130(12):124102, 2009.
- [264] Chenyang Li and Francesco A Evangelista. Connected three-body terms in single-reference unitary many-body theories: Iterative and perturbative approximations. *J. Chem. Phys.*, 152(23):234116, 2020.
- [265] Kerstin Andersson, Per-Åke Malmqvist, and Björn O Roos. Second-order perturbation theory with a complete active space self-consistent field reference function. *J. Chem. Phys.*, 96(2):1218–1226, 1992.
- [266] Werner Kutzelnigg. Quantum chemistry in Fock space. I. The universal wave and energy operators. *J. Chem. Phys.*, 77(6):3081–3097, 1982.
- [267] David A Mazziotti. Contracted schrödinger equation: Determining quantum energies and two-particle density matrices without wave functions. *Phys. Rev. A*, 57(6):4219–4234, 1998.
- [268] W Kutzelnigg and Debashis Mukherjee. Cumulant expansion of the reduced density matrices. *The Journal of Chemical Physics*, 110(6):2800–2809, 1999.
- [269] Shuhe Wang, Chenyang Li, and Francesco A Evangelista. Analytic Energy Gradients for the Driven Similarity Renormalization Group Mul-

- reference Second-Order Perturbation Theory. *J. Chem. Theory Comput.*, 17(12):7666–7681, 2021.
- [270] Nan He, Chenyang Li, and Francesco A Evangelista. Second-Order Active-Space Embedding Theory. *J. Chem. Theory Comput.*, 18(3):1527–1541, 2022.
- [271] Andrew Zhao, Nicholas C Rubin, and Akimasa Miyake. Fermionic partial tomography via classical shadows. *Phys. Rev. Lett.*, 127(11):110504, 2021.
- [272] Francesco A Evangelista. Forte: a suite of quantum chemistry methods for strongly correlated electrons. <https://github.com/evangelistalab/forte>, 2023.
- [273] Daniel G A Smith, Lori A Burns, Andrew C Simmonett, Robert M Parrish, Matthew C Schieber, Raimondas Galvelis, Peter Kraus, Holger Kruse, Roberto Di Remigio, Asem Alenaizan, Andrew M James, Susi Lehtola, Jonathon P Misiewicz, Maximilian Scheurer, Robert A Shaw, Jeffrey B Schriber, Yi Xie, Zachary L Glick, Dominic A Sirianni, Joseph Senan O'Brien, Jonathan M Waldrop, Ashutosh Kumar, Edward G Hohenstein, Benjamin P Pritchard, Bernard R Brooks, Henry F III Schaefer, Alexander Yu Sokolov, Konrad Patkowski, A Eugene III DePrince, Ugur Bozkaya, Rollin A King, Francesco A Evangelista, Justin M Turney, T Daniel Crawford, and C David Sherrill. Psi4 1.4: Open-source software for high-throughput quantum chemistry. *J. Chem. Phys.*, 152(18):184108, 2020.

- [274] Thom H Dunning. Gaussian basis sets for use in correlated molecular calculations. I. The atoms boron through neon and hydrogen. *J. Chem. Phys.*, 90(2):1007–1023, 1989.
- [275] F Colmenero, C Pérez del Valle, and C Valdemoro. Approximating q -order reduced density matrices in terms of the lower-order ones. i. general relations. *Phys. Rev. A*, 47(2):971–978, 1993.
- [276] A Eugene DePrince and David A Mazziotti. Cumulant reconstruction of the three-electron reduced density matrix in the anti-hermitian contracted schrödinger equation. *J. Chem. Phys.*, 127(10):104104, 2007.
- [277] Micah L Abrams and C David Sherrill. Natural orbitals as substitutes for optimized orbitals in complete active space wavefunctions. *Chem. Phys. Lett.*, 395(4–6):227–232, 2004.
- [278] C Garrod and J K Percus. Reduction of the n -particle variational problem. *J. Math. Phys.*, 5:1756–1776, 1964.
- [279] R M Erdahl. Representability. *Int. J. Quantum Chem.*, 13:697–718, 1978.
- [280] Z Zhao, B J Braams, M Fukuda, M L Overton, and J K Percus. The reduced density matrix method for electronic structure calculations and the role of three-index representability conditions. 120:2095–2104, 2004.
- [281] D A Mazziotti. Structure of fermionic density matrices: Complete n -representability conditions. 108:263002, 2012.

- [282] Nicholas C Rubin, Ryan Babbush, and Jarrod McClean. Application of fermionic marginal constraints to hybrid quantum algorithms. *New J. Phys.*, 20(5):053020, 2018.
- [283] Aleksandra Leszczyk, Mihály Máté, Ors Legeza, and Katharina Boguslawski. Assessing the accuracy of tailored coupled cluster methods corrected by electronic wave functions of polynomial cost. *J. Chem. Theory Comput.*, 18(1):96–117, 2021.
- [284] Chenyang Li and Francesco A Evangelista. Towards numerically robust multireference theories: The driven similarity renormalization group truncated to one- and two-body operators. *J. Chem. Phys.*, 144(16):164114, April 2016.
- [285] K Raghavachari, Gary W Trucks, John A Pople, and Martin Head-Gordon. A fifth-order perturbation comparison of electron correlation theories. *Chem. Phys. Lett.*, 157(6):479, 1989.
- [286] Steven R. White. Density matrix formulation for quantum renormalization groups. *Phys. Rev. Lett.*, 69:2863–2866, Nov 1992.
- [287] Hans-Joachim Werner and Peter J Knowles. An efficient internally contracted multiconfiguration reference configuration-interaction method. *J. Chem. Phys.*, 89(9):5803–5814, 1988.
- [288] Peter J Knowles and Hans-Joachim Werner. An efficient method for the evaluation of coupling-coefficients in configuration-interaction calculations. *Chem. Phys. Lett.*, 145(6):514–522, 1988.

- [289] Stephen R Langhoff and Ernest R Davidson. Configuration interaction calculations on the nitrogen molecule. *Int. J. Quantum Chem.*, 8(1):61–72, January 1974.
- [290] Francesco A Evangelista, Wesley D Allen, and Henry F Schaefer. Coupling term derivation and general implementation of state-specific multireference coupled cluster theories. *J. Chem. Phys.*, 127(2):024102, July 2007.
- [291] Francesco A Evangelista, Matthias Hanauer, Andreas Koehn, and Juer-gen Gauss. A sequential transformation approach to the internally contracted multireference coupled cluster method. *J. Chem. Phys.*, 136(20):204108, 2012.
- [292] P Wenthold, RR Squires, and WC Lineberger. Ultraviolet Photoelectron Spectroscopy of the *o*-, *m*-, and *p*-Benzyne negative ions. Electron Affinities and Singlet-Triplet Splittings for *o*-, *m*-, and *p*-Benzyne. *J. Am. Chem. Soc.*, 120(21):5279–5290, June 1998.
- [293] Matthias Hanauer and Andreas Köhn. Perturbative treatment of triple excitations in internally contracted multireference coupled cluster theory. *J. Chem. Phys.*, 136(20):204107–204107–18, 2012.
- [294] Ajith Perera, Robert W Molt, Victor F Lotrich, and Rodney J Bartlett. Singlet–triplet separations of di-radicals treated by the dea/dip-eom-ccsd methods. *Theor. Chem. Acc.*, 133:1514, 2014.
- [295] Sahil Gulania, Eirik F. Kjørstad, John F. Stanton, Henrik Koch, and Anna I. Krylov. Equation-of-motion coupled-cluster method with dou-

- ble electron-attaching operators: Theory, implementation, and benchmarks. *J. Chem. Phys.*, 154(11):114115, 2021.
- [296] Prashant U. Manohar and Anna I. Krylov. A noniterative perturbative triples correction for the spin-flipping and spin-conserving equation-of-motion coupled-cluster methods with single and double substitutions. *J. Chem. Phys.*, 129(19):194105, 2008.
- [297] LV Slipchenko and Anna I Krylov. Singlet-triplet gaps in diradicals by the spin-flip approach: A benchmark study. *J. Chem. Phys.*, 117:4694, 2002.
- [298] Xiangzhu Li and Josef Paldus. Electronic structure of organic diradicals: Evaluation of the performance of coupled-cluster methods. *J. Chem. Phys.*, 129:174101, 2008.
- [299] Christopher J Cramer, JJ Nash, and RR Squires. A reinvestigation of singlet benzyne thermochemistry predicted by CASPT2, coupled-cluster and density functional calculations. *Chem. Phys. Lett.*, 277(4):311–320, October 1997.
- [300] Roland Lindh, A Bernhardsson, and Martin Schütz. Benzyne thermochemistry: A benchmark ab initio study. *J. Phys. Chem. A*, 103(48):9913–9920, December 1999.
- [301] Hua Li, Shu-Yuan Yu, Ming-Bao Huang, and Zhi-Xiang Wang. The s1 states of o-, m-, and p-benzyne studied using multiconfiguration second-order perturbation theory. *Chem. Phys. Lett.*, 450(1-3):12–18, 2007.

- [302] Evan B Wang, Carol A Parish, and Hans Lischka. An extended multireference study of the electronic states of para-benzyne. *J. Chem. Phys.*, 129(4):044306, 2008.
- [303] Shuhe Wang, Chenyang Li, and Francesco A Evangelista. Analytic gradients for the single-reference driven similarity renormalization group second-order perturbation theory. *J. Chem. Phys.*, 151(4):044118, July 2019.
- [304] Armağan Kinal and Piotr Piecuch. Computational investigation of the conrotatory and disrotatory isomerization channels of bicyclo [1.1. 0] butane to buta-1, 3-diene: a completely renormalized coupled-cluster study. *J. Phys. Chem. A*, 111(4):734–742, 2007.
- [305] Raphael Berner and Arne Lüchow. Isomerization of bicyclo [1.1. 0] butane by means of the diffusion quantum monte carlo method. *J. Phys. Chem. A*, 114(50):13222–13227, 2010.
- [306] R Srinivasan, AA Levi, and I Haller. The thermal decomposition of bicyclo [1.1. 0] butane. *J. Phys. Chem.*, 69(5):1775–1777, 1965.
- [307] Kenneth B Wiberg and Richard A Fenoglio. Heats of formation of c4h6 hydrocarbons. *J. Am. Chem. Soc.*, 90(13):3395–3397, 1968.
- [308] EP Blanchard Jr and A Cairncross. Bicyclo [1.1. 0] butane chemistry. i. the synthesis and reactions of 3-methylbicyclo [1.1. 0] butanecarbonitriles. *J. Am. Chem. Soc.*, 88(3):487–495, 1966.

- [309] HM Frey and IDR Stevens. Thermal unimolecular isomerization of bicyclobutane. *Trans. Faraday Soc.*, 61:90–94, 1965.
- [310] Kenneth B Wiberg and Jerome M Lavanish. Formation and thermal decomposition of bicyclo [1.1. 0] butane-2-exo-d11. *J. Am. Chem. Soc.*, 88(22):5272–5275, 1966.
- [311] GL Closs and PE Pfeffer. The steric course of the thermal rearrangements of methylbicyclobutanes. *J. Am. Chem. Soc.*, 90(9):2452–2453, 1968.
- [312] David A Mazziotti. Energy barriers in the conversion of bicyclobutane to gauche-1, 3-butadiene from the anti-hermitian contracted schrodinger equation. *J. Phys. Chem. A*, 112(51):13684–13690, 2008.
- [313] Kiet A Nguyen and Mark S Gordon. Isomerization of bicyclo [1.1. 0] butane to butadiene. *J. Am. Chem. Soc.*, 117(13):3835–3847, 1995.
- [314] Jesse J Lutz and Piotr Piecuch. Extrapolating potential energy surfaces by scaling electron correlation: Isomerization of bicyclobutane to butadiene. *J. Chem. Phys.*, 128(15):154116, 2008.
- [315] Jan-Niklas Boyn and David A Mazziotti. Elucidating the molecular orbital dependence of the total electronic energy in multireference problems. *J. Chem. Phys.*, 156(19):194104, 2022.
- [316] Jérôme F Gonthier, Maxwell D Radin, Corneliu Buda, Eric J Doskocil, Clena M Abuan, and Jhonathan Romero. Measurements as a roadblock

- to near-term practical quantum advantage in chemistry: resource analysis. *Phys. Rev. Res.*, 4(3):033154, 2022.
- [317] Wesley D Allen and Henry F Schaefer. Ab initio Studies of the Low-Lying Electronic States of Ketene. *J. Chem. Phys.*, 84(4):2212–2225, February 1986.
- [318] Wesley D Allen and Henry F Schaefer. An examination of the $2\ 1a_1$ states of formaldehyde and ketene including analytic configuration interaction energy first derivatives for singlet excited electronic states of the same symmetry as the ground state. *J. Chem. Phys.*, 87(12):7076–7095, December 1987.
- [319] Robert M Parrish, Joseph T Iosue, Asier Ozaeta, and Peter L McMahon. A jacobi diagonalization and anderson acceleration algorithm for variational quantum algorithm parameter optimization. *arXiv preprint arXiv:1904.03206*, 2019.
- [320] Ken M Nakanishi, Keisuke Fujii, and Synge Todo. Sequential minimal optimization for quantum-classical hybrid algorithms. *Phys. Rev. Research*, 2(4):043158, 2020.
- [321] Phillip Kaye, Raymond Laflamme, and Michell Mosca. An introduction to quantum computing, 2007.
- [322] Michael E Beverland, Prakash Murali, Matthias Troyer, Krysta M Svore, Torsten Hoeffler, Vadym Kliuchnikov, Guang Hao Low, Mathias Soeken, Aarthi Sundaram, and Alexander Vaschillo. Assessing requirements to

- scale to practical quantum advantage. *arXiv preprint arXiv:2211.07629*, 2022.
- [323] Seunghoon Lee, Joonho Lee, Huanchen Zhai, Yu Tong, Alexander M Dalzell, Ashutosh Kumar, Phillip Helms, Johnnie Gray, Zhi-Hao Cui, Wenyuan Liu, et al. Evaluating the evidence for exponential quantum advantage in ground-state quantum chemistry. *Nat. Commun.*, 14(1):1952, 2023.
- [324] Jingwei Wen, Dingshun Lv, Man-Hong Yung, and Gui-Lu Long. Variational quantum packaged deflation for arbitrary excited states. *Quantum Eng.*, 3(4):e80, 2021.
- [325] Renke Huang, Chenyang Li, and Francesco A Evangelista. Leveraging small-scale quantum computers with unitarily downfolded hamiltonians. *PRX Quantum*, 4(2):020313, 2023.
- [326] Chenyang Li and Francesco A Evangelista. Driven similarity renormalization group for excited states: A state-averaged perturbation theory. *J. Chem. Phys.*, 148(12):124106, March 2018.
- [327] Jean Paul Malrieu, Jean Louis Heully, and Andréi Zaitsevskii. Multiconfigurational second-order perturbative methods: Overview and comparison of basic properties. *Theor. Chim. Acta*, 90(2-3):167–187, January 1995.
- [328] Michal Ben-Nun, Jason Quenneville, and Todd J Martínez. Ab initio multiple spawning: Photochemistry from first principles quantum molecular dynamics. *J. Phys. Chem. A*, 104(22):5161–5175, 2000.

- [329] M Barbatti, J Paier, and H Lischka. Photochemistry of ethylene: A multireference configuration interaction investigation of the excited-state energy surfaces. *J. Chem. Phys.*, 121(23):11614–11624, 2004.
- [330] Benjamin G Levine and Todd J Martínez. Isomerization through conical intersections. *Annu. Rev. Phys. Chem.*, 58:613–634, 2007.
- [331] Jimmy K Yu, Christoph Bannwarth, Edward G Hohenstein, and Todd J Martínez. Ab initio nonadiabatic molecular dynamics with hole–hole tamm–dancoff approximated density functional theory. *J. Chem. Theory Comput.*, 16(9):5499–5511, 2020.
- [332] Zhen Lu and Spiridoula Matsika. High-multiplicity natural orbitals in multireference configuration interaction for excited states. *J. Chem. Theory Comput.*, 8(2):509–517, 2012.
- [333] Ignacio Fdez. Galvan, Mickael G Delcey, Thomas Bondo Pedersen, Francesco Aquilante, and Roland Lindh. Analytical state-average complete-active-space self-consistent field nonadiabatic coupling vectors: Implementation with density-fitted two-electron integrals and application to conical intersections. *J. Chem. Theory Comput.*, 12(8):3636–3653, 2016.
- [334] Noriyuki Minezawa and Mark S Gordon. Optimizing conical intersections by spin-flip density functional theory: application to ethylene. *J. Phys. Chem. A*, 113(46):12749–12753, 2009.

- [335] B G Levine, C Ko, J Quenneville, and Todd J Martínez. Conical intersections and double excitations in time-dependent density functional theory. *Mol. Phys.*, 104(5-7):1039–1051, 2006.
- [336] John F Stanton. Coupled-cluster theory, pseudo-Jahn–Teller effects and conical intersections. *J. Chem. Phys.*, 115(22):10382–10393, 2001.
- [337] Andreas Köhn and Attila Tajti. Can coupled-cluster theory treat conical intersections? *J. Chem. Phys.*, 127(4):044105, July 2007.
- [338] Eirik F Kjøenstad, Rolf H Myhre, Todd J Martínez, and Henrik Koch. Crossing conditions in coupled cluster theory. *J. Chem. Phys.*, 147(16):164105, October 2017.
- [339] Shigeki Gocho, Hajime Nakamura, Shu Kanno, Qi Gao, Takao Kobayashi, Taichi Inagaki, and Miho Hatanaka. Excited state calculations using variational quantum eigensolver with spin-restricted ansätze and automatically-adjusted constraints. *npj Comput. Mater.*, 9:13, 2023.
- [340] Bryan T Gard, Linghua Zhu, George S Barron, Nicholas J Mayhall, Sophia E Economou, and Edwin Barnes. Efficient Symmetry-Preserving State Preparation Circuits for the Variational Quantum Eigensolver Algorithm. *npj Quantum Inf.*, 6(1):10, January 2020.
- [341] Kanav Setia, Richard Chen, Julia E Rice, Antonio Mezzacapo, Marco Pistoia, and James D Whitfield. Reducing Qubit Requirements for Quantum Simulations Using Molecular Point Group Symmetries. *J. Chem. Theory Comput.*, 16(10):6091–6097, August 2020.

- [342] Ryan V. Mishmash, Tanvi P. Gujarati, Mario Motta, Huanchen Zhai, Garnet Kin-Lic Chan, and Antonio Mezzacapo. Hierarchical clifford transformations to reduce entanglement in quantum chemistry wave functions. *J. Chem. Theory Comput.*, 19(11):3194–3208, 2023. PMID: 37227024.
- [343] Rick A Kendall, Thom H Dunning, and Robert J Harrison. Electron affinities of the first-row atoms revisited. Systematic basis sets and wave functions. *J. Chem. Phys.*, 96(9):6796–6806, 1992.
- [344] Florian Weigend. A fully direct RI-HF algorithm: Implementation, optimised auxiliary basis sets, demonstration of accuracy and efficiency. *Phys. Chem. Chem. Phys.*, 4(18):4285–4291, 2002.
- [345] Jae Woo Park. Analytical gradient theory for spin-free state-averaged second-order driven similarity renormalization group perturbation theory (sa-dsrg-mrpt2) and its applications for conical intersection optimizations. *J. Chem. Theory Comput.*, 18(4):2233–2245, 2022. PMID: 35229599.
- [346] Michael J Bearpark, Michael A Robb, and H Bernhard Schlegel. A direct method for the location of the lowest energy point on a potential surface crossing. *Chem. Phys. Lett.*, 223(3):269–274, 1994.
- [347] Sergey Bravyi, Sarah Sheldon, Abhinav Kandala, David C. McKay, and Jay M. Gambetta. Mitigating measurement errors in multiqubit experiments. *Phys. Rev. A*, 103:042605, Apr 2021.

- [348] Ying Li and Simon C Benjamin. Efficient Variational Quantum Simulator Incorporating Active Error Minimization. *Phys. Rev. X*, 7(2):361–14, June 2017.
- [349] Shuaining Zhang, Yao Lu, Kuan Zhang, Wentao Chen, Ying Li, Jing-Ning Zhang, and Kihwan Kim. Error-mitigated quantum gates exceeding physical fidelities in a trapped-ion system. *Nat. Commun.*, 11(1):587, 2020.